UQAR

Université du Québec
à Rimouski

Télédétection de la matière en suspension dans l'estuaire de Saint-Laurent

Thèse présentée

dans le cadre du programme de doctorat en océanographie

en vue de l'obtention du grade de PhD

PAR

© Gholamreza Mohammadpour

Novembre 2016

UQAR

Université du Québec
à Rimouski

Remote sensing of suspended particulate matter concentration
in the St. Lawrence Estuary

Thesis presented

In the doctorate program of oceanography

To obtain the degree of PhD

by

November 2016

Composition du jury :

Huixiang Xie, président du jury, UQAR

Jean-Pierre Gagné, directeur de recherche, UQAR

Martin A. Montes-Hugo, codirecteur de recherche, UQAR

Pierre Larouche, co-directeur de recherche, Institut Maurice Lamontagne

Susanne Craig, examinateur externe, Université de Dalhousie

Dépôt initial le 7 Novembre 2016   Dépôt final 1 Mars 2017

UNIVERSITÉ DU QUÉBEC À RIMOUSKI

Service de la bibliothèque
Avertissement

To my lovely family;

Sheila, Veyana, and Sayna

x

ACKNOWLEDGEMENT/REMERCIEMENTS

RÉSUMÉ

Les zones côtières et estuariennes jouent un rôle clé dans les processus biogéochimiques comme les échanges de gaz à effet de serre à l'interface air-mer, la photosynthèse et la régénération des nutriments. Tous ces processus sont liés à la dynamique des matières particules en suspension (MPS). L'estuaire du Saint-Laurent (ESL) est un des plus grands estuaires du monde. On y retrouve un important mélange de propriétés chimiques et optiques résultant de la combinaison des eaux douces en provenance du fleuve St-Laurent (FSL) et des eaux marines du golfe du Saint-Laurent (GSL). L'objectif principal de cette thèse est d'évaluer, développer et valider différents modèles de télédétection optique pour estimer la concentration de MPS dans les eaux de l'ESL.

Cette thèse présente en plus deux objectifs secondaires. Premièrement, caractériser, pour la zone étudiée, les distributions de tailles de la MPS, puis déterminer les propriétés optiques massiques spécifiques de la matière en suspension. Avec ces données certains proxys sont proposés pour étudier les attributs de deuxième ordre de la MPS. Deuxièmement, une revue des effets thermiques induits par la présence des MPS dans les eaux océaniques et littorales est réalisée. Cette synthèse incorpore une analyse des changements potentiels que pourraient subir certaines variables climatiques dues aux variations de chaleur associé à la distribution et à la nature des particules.

Le premier chapitre résume les concepts relatifs à l'optique marine et la télédétection de la couleur des océans dans les eaux estuariennes et côtières. Le deuxième chapitre présente une relation biogéo-optique pour cartographier les distributions C_{MPS} dans l'estuaire supérieur du Saint-Laurent basé sur des mesures satellitaires de couleur de l'océan à moyenne résolution spatiale. Enfin, l'influence de la composition chimique des particules sur la

télédétection des C_{MPS} est investiguée et une série de nouveaux paramètres sont présentés pour estimer le contenu organique des MPS dans l'ESL.

Le troisième chapitre traite de la caractérisation des propriétés optiques de la MPS ayant différentes compositions chimiques et tailles dans les eaux de l'ESL. Dans ce chapitre, l'effet de la composition et des tailles sur les propriétés optiques inhérentes des particules et leurs effets sur les signaux optiques détectés par des capteurs optiques sont étudiés.

Le quatrième chapitre propose une revue du rôle des particules dans la modulation de la variabilité spatiale de la température de l'eau, des flux de chaleur à l'interface air-mer et des variables météorologiques locales. La contribution de la MPS et celle de la matière organique dissoute chromophorique (MODC) dans le budget de chaleur dans les eaux côtières et océaniques sont examinées. De plus, le rôle du flux de chaleur induit par les particules dans l'altération des processus de formation de nuage et de précipitations et la dynamique des banquises est analysé.

En conclusion, pour l'ESL, les résultats obtenus dans cette thèse montrent que la concentration et la composition chimique des MPS peuvent être estimées à partir de méthode de télédétection optique avec une exactitude acceptable (c.-à-d.. une erreur d'environ 30 %). L'approche proposée devrait être valide dans d'autres environnements littoraux ayant des propriétés biogéooptiques comparables à celles mesurées dans la région d'étude. Il a été démontré que des changements dans la composition chimique des particules peuvent constituer une importante source de variabilité dans l'évaluation des C_{MPS} estimée par télédétection dans la région d'étude. Finalement, la discussion du chapitre 3 a révélé une importance comparable de l'effet des particules en suspension et des matières dissoutes sur la température de l'eau et la variabilité des flux de chaleur dans les eaux côtières.

Mots clés : matières particulaires en suspension, distribution de tailles des particules, composition des particules, matière organique dissoute colorée, propriétés optiques inhérentes, télédétection, flux de chaleur, température de l'eau surface, variabilité du climat

ABSTRACT

Estuarine and coastal zones play a key role in biogeochemical processes such as air-water exchange of greenhouse gases, photosynthesis and regeneration of nutrients. All these processes are linked to dynamics of suspended particulate matter (SPM). The St. Lawrence Estuary (SLE) is one of the largest estuaries in the world where a major mixing of chemical and optical properties occurs due to the exchange of water parcels derived from the St Lawrence River (SLR) and the Gulf of St. Lawrence (GSL). The primary objective of this thesis is to evaluate, develop and validate different optical remote sensing models for estimating concentration of SPM in SLE waters.

In addition, this thesis has two secondary objectives: Firstly, mass-normalized optical properties of different chemical and size distribution fractions are characterized over the study area, and optical remote sensing proxies are proposed for studying second-order attributes of SPM. Secondly, a review of particle-mediated thermal effects in oceanic and littoral waters is achieved. Also, this synthesis incorporates an analysis of potential changes on climate variables due to variations on water heat content. associated to different particle distributions and nature.

The first chapter summarizes the actual concepts on marine optics and remote sensing of ocean color in estuarine and coastal waters. In the second chapter, a biogeo-optical relationship is suggested to map C_{SPM} distributions in the upper SLE and based on satellite ocean color measurements having a moderate spatial resolution. Lastly, the influence of particle chemical composition on remote sensing of C_{SPM} was investigated, and a series of new parameterizations are shown for estimating organic content of SPM in SLE waters.

The third chapter is about the characterization of optical properties of different chemical and size fractions of SPM in SLE waters. In this chapter, the effect of particle

composition and size distribution on the inherent optical properties of particles and their effects on optical signals arriving to the remote sensing sensor are investigated.

The fourth chapter reviews the role of particles in in modulating the spatial variability of water temperature, air-water heat fluxes and local weather variables. Here, the contribution of SPM and chromophoric dissolved organic matter (CDOM) to heat budget components in coastal and oceanic waters was examined. Also, the role of the particle – mediated heat flux in altering the behavior of cloud formation and precipitation, and the dynamics of sea ice was analyzed.

In summary for the SLE, the results obtained during this thesis showed that concentration and chemical composition of SPM can be estimated based on optical remote sensing methods and with an acceptable accuracy (i.e., around 30% error). The proposed approach is expected to be valid in other littoral environments with comparable biogeo-optical properties to those typical measured over the study area. It was demonstrated that changes on particle chemical composition may be an important source of variability on remote sensing estimates of C_{SPM} in our study area. Lastly, the discussion of chapter 3 revealed the comparable importance of particulate and dissolved matter affecting water temperature and heat flux variability in land-influenced waters.

Keywords: Suspended particulate matter, particle size distribution, particle composition, CDOM, inherent optical properties, remote sensing, air-water heat flux, water surface temperature, climate variability

TABLE OF CONTENTS

LIST OF TABLES

CHAPTER 4

LIST OF FIGURES

xxviii

CHAPTER 3

CHAPTER 4

LIST OF ABREVIATIONS AND ACRONYMS

AATSR	Advanced along track scanning radiometer
AO	Atlantic oscillation
AOGCM	Atmosphere-ocean general circulation model
AOPs	Apparent optical properties
ATOVS	Advanced TIROS operational vertical sounder
AVHRR	Advanced very high-resolution radiometers
BOI comp	Bio-optical index for particle composions
BOI size	Bio-optical index for particle size fractions
CDOM	Chromophoric dissolved organic matter
CDR	Climate date records
Chl	Chlorophyll-a concentration
CTD	Conductivity, temperature, and depth
DOM	Dissolved organic matter
e	Emissivity of the sea surface
EUMETSAT	European organization for the exploitation of meteorological satellites
Fr	Fresnel reflectivity

GAC	Global area coverage
GBN	Global buoy network
GHRSST	Group for high resolution sea surface temperature
GOES	Geostationary operational environmental satellite
GTS	Global telecommunication system
HIRS	High resolution radiation sounder
HyspIRI	Hyperspectral infrared imager
IASI	Infrared atmospheric sounding interferometer
ISAR	Infrared sea surface temperature autonomous radiometer
LDV	Laser Doppler velocimetry
LE	Lower estuary
LIDAR	Light detection and ranging
M-**AERI**	Marine-atmosphere emitted radiance interferometer
MEI	Multivariate ENSO index
MERIS	Medium resolution imaging spectrometer
MHS	Microwave humidity sounder
MIRS	Microwave integrated retrieval system
NAO	North Atlantic oscillation
NAP	Non-algal particulates
NCEP	National center for environmental predictions

NESDIS	National environmental satellite, data, and information service
NIR	Near-infrared
NOAA	National oceanic and atmospheric administration
PIM	Particulate inorganic matter
PIV	particle image velocimetry
POM	Particulate organic matter
PSD	Particle size distribution
PSU	Practical salinity units
RHR	Radiant heat rate
RMSE	Root mean square error
SAR	Synthetic aperture radar
SF	Saguenay Fjord
SISTeR	Scanning infrared sea surface temperature radiometer
SLE	Saint Lawrence Estuary
SLR	Saint Lawrence river
SPM	Suspended particulate matter
SSEC	Space science and engineering center
SSM/I	Special sensor microwave imager
SST	Sea surface temperature
TIR	Thermal infrared

TIROS	Television infrared observation satellite
TOA	Top of the atmosphere
UE	Upper Estuary
UV	Ultra violet
VOS	Voluntary observing ships
WMO	World meteorological organization

LIST OF SYMBOLS

λ	Wavelength	nm
κ	Heat capacity	W m^{-2} kg^{-1} K^{-1}
ρ_t	Fresnel reflection coefficient	
$\nabla^2 T$	Laplacian of temperature	°C^2 m^{-2}
A_h	Horizontal viscosity	m^2 s^{-1}
$q_{z=-h}$	Heat flux at the depth h	W m^{-2} s^{-1}
W_e	Environment velocity	m s^{-1}
C_E	Coefficient of latent flux	K W m^{-2} kg^{-1} K^{-1}
C_H	Coefficient of sensible flux	K W m^{-2} kg^{-1} K^{-1}
$C_{p,a}$	Constant pressure specific heat of air	K W m^{-2} kg^{-1} K^{-1}
$E_d(z, \lambda)$	Spectral downwelling at the depth z	W m^{-2} nm^{-1}
$E_n(z, \lambda)$	Net irradiance profiles at the depth z	W m^{-2} nm^{-1}
$E_u(z, \lambda)$	Upwelling irradiances at the depth z	W m^{-2} nm^{-1}
I_{BLUE}	Irradiance in blue band	W m^{-2}
I_{RED}	Irradiance in red band	W m^{-2}

$L(\theta,\phi',z)$	Incident spectral radiance in zenith and azimuth directions	μW m^{-2} sr^{-1} nm^{-1}
$L(\theta,\phi,z)$	spectral radiance in zenith and azimuth directions (θ,ϕ)	μW m^{-2} sr^{-1} nm^{-1}
L_V	Evaporative latent heat	W m^{-2} s^{-1}
$\widetilde{\beta}$	Scattering phase function	sr^{-1}
$\omega(\tau)$	Single-scattering reflectance	sr^{-1}
Ω'	Solid angle of the incident light beam	$^{\circ}$
μ	Medium refractive index	
Q_E	Latent heat flux	W m^{-2} s^{-1}
Q_H	Sensible heat flux	W m^{-2} s^{-1}
Q_R	Radiative heat flux	W m^{-2} s^{-1}
R_d	Complementary downwelling sky radiance	Wsr^{-1}m^{-2}
R_u	Upwelling sea radiance	Wsr^{-1}m^{-2}
τ	Optical depth	m
$T_r(z)$	Solar transmission function	-
$a(\lambda)$	Total absorption coefficient	m^{-1}
$a_w(\lambda)$	Water absorption coefficient at a specific wavelength	m^{-1}

$a_{\mathrm{p}}(\lambda)$	Particulate absorption coefficient	m^{-1}
$a_{CDOM}(\lambda)$	Absorption coefficient of chromophoric dissolved organic matter at a specific wavelength	m^{-1}
$a_{NAP}(\lambda)$	Absorption coefficient non-algal particles at a specific wavelength	m^{-1}
$a_{ph}(\lambda)$	Phytoplankton absorption coefficient at a specific wavelength	m^{-1}
$a_{\mathrm{p}}{}^{*}(\lambda)$	Mass-specific absorption coefficient for particulate matter	$m^2\,g^{-1}$
c_p	Specific heat of seawater	$W\,m^{-2}\,kg^{-1}\,°C^{-1}$
$k_b(\lambda)$	Attenuation coefficients of particulates with blue/green colors	m^{-1}
$k_r(\lambda)$	Attenuation coefficients of particulates with red/yellow colors	m^{-1}
u_*	Friction velocity	$m\,s^{-1}$
$\alpha_a(\lambda)$	Sea-surface albedo at a specific wavelength	-
ρ_a	Air density	$Kg\,m^{-3}$
ΔT	Air-sea difference of temperature	$°C$
$\nabla \mathbf{T}$	Gradient of temperature	$°C\,m^{-1}$

$b(\lambda)$	Total scattering coefficient	m^{-1}
$b_p(\lambda)$	Scattering coefficient for particulate matter	m^{-1}
$b_b(\lambda)$	Total backscattering coefficient	m^{-1}
$b_b{}^{eff}(\lambda)$	Backscattering efficiency	
$b_{bp}(\lambda)$	Particulate backscattering coefficient	m^{-1}
$b_{bw}(\lambda)$	Water backscattering coefficient	m^{-1}
$b^{eff}(\lambda)$	Scattering efficiency	Dimensionless
$b_b{}^{eff}(\lambda)$	Backscattering efficiency	Dimensionless
$b_p{}^{*}(\lambda)$	Mass-specific particulate scattering coefficient	m^2 g^{-1}
BOI ^{size}	Biogeo-optical proxy for size distribution of SPM	dimensionless
BOI ^{comp}	Biogeo-optical proxy for chemical composition of SPM	dimensionless
$c(\lambda)$	Total beam attenuation coefficient	m^{-1}
Chl	Chlorophyll-a concentration	mg m^{-3}
C$_{PIM}$	Concentration of particulate inorganic matter	g m^{-3}
C$_{POM}$	Concentration of particulate organic matter	g m^{-3}
C$_{SPM}$	Concentration of suspended particulate matter	g m^{-3}

$C_{SPM}{}^{MERIS}$	MERIS-derived concentration of suspended particulate matter	g m^{-3}
$E_d(\lambda)$	Spectral downwelling irradiance at a specific wavelength	W m^{-2} nm^{-1}
$F_{SPM}{}^{i}$	Contribution of size fraction i to the total mass of SPM	dimensionless
$F_{SPM}{}^{PIM}$	Inorganic fraction of suspended particulate matter	%
h	Mixed-layer depth	m
$L_g(\lambda)$	Reference radiance at a specific wavelength	µW m^{-2} sr^{-1} nm^{-1}
$L_{sky}(\lambda)$	Sky radiance at a specific wavelength	µW m^{-2} sr^{-1} nm^{-1}
$L_u(\lambda)$	Total water upwelling radiance at a specific wavelength	µW m^{-2} sr^{-1} nm^{-1}
$L_w(\lambda)$	Spectral water-leaving radiance at a specific wavelength	µW m^{-2} sr^{-1} nm^{-1}
m_{SPM}	Mass of suspended particulate matter	g m^{-3}
n_w	Water refractive index	
Q	Net heat flux through the sea surface	W m^{-2} s^{-1}
r	Average internal Fresnel reflection	
T_∞	Reference temperature	°C

T	Temperature	°C
$R(\lambda)$	reflectance at a specific wavelength	sr^{-1}
q	Heat transfer coefficient	$W\ m^{-2}\ K^{-1}$
$RHR(z)$	Radiant heat rate at specific depth	$°C\ s^{-1}$
$R_{rs}(\lambda)$	Remote sensing reflectance at a specific wavelength	sr^{-1}
SPM	Suspended particulate matter	$g\ m^{-3}$
PIM	Particulate organic matter	$g\ m^{-3}$
POM	Particulate inorganic matter	$g\ m^{-3}$
U	Wind speed above the air-sea interface	$m\ s^{-1}$
Z	Depth	m
α	Thermal expansion coefficient of seawater	$°C^{-1}$
γ	Differential Junge slope	Number of particulates per μm
$\sigma_a(\lambda)$	Mass-specific absorption cross section	$m^2\ g^{-1}$
$\sigma_b(\lambda)$	Mass-specific scattering cross section	$m^2\ g^{-1}$

xl

CHAPTER 1

1. GENERAL INTRODUCTION

1.1 BASIC OPTICAL REMOTE SENSING CONCEPTS

Remote sensing is the scientific discipline that studies the characteristics of an object having a direct contact. Thus, remote sensing is a broad term that includes optical, thermal, microwave and acoustic measurements. Optical remote sensing measurements are obtained within the spectral range of UV-visible (300-700 nm) and near-mid IR (700-3000 nm).

Optical remote sensing measurements derived from satellites allow us to have synoptic observations of the object under investigation. Likewise, these methods provide the analysis of long-term regional trends on biogeochemical variables such as primary production, the fate of pollutants, and sediment transport in littoral waters (Jacobi et al., 2015; Balch et al., 2002; Coulombier et al., 2012b). However, traditional methods for monitoring SPM are based on costly and time-consuming oceanographic surveys that have a limited coverage, spatially and temporally.

1.2 OPTICAL REMOTE SENSING SYSTEM COMPONENTS

An optical remote sensing system is constituted by four elements: 1. the light source, 2. the target or object to be detected, 3. the receiver or sensor, and 4. the optical medium between the receiver and the target. Passive optical remote sensing systems have the sun as the light source and can detect reflected energy coming from the target. Unlike passive optical systems, active optical systems have a laser as a light source. These systems are currently known as LiDARs or light detection and range.

1.3 LIGHT PROPAGATION IN AIR AND WATER

The Penetrated beam in a water body can be absorbed or scattered. The photon is absorbed if it is permanently removed from the light beam. However, scattering redirects the angle of the light beam pathway. Unlike scattering which barely depends on the wavelength of the light beam, absorption highly depends on wavelength variation. The spectral beam attenuation coefficient $c(\lambda)$ of a medium describes the fraction of incident beam intensity attenuated per meter of the medium.

In studying biogeochemical processes at littoral surface waters, the goal is to measure the water-leaving electromagnetic signals reflected from water constituents towards the remote optical sensor. An optical remote optical sensor must deal with various interfering factors that influence the photon's path length. These radiance contributions causing interference include the effect of atmosphere and aerosols, bottom reflection, reflection by air bubbles, and adjacency effects (**Figure 1**).

$$L_w + L_{bub} = L_u - L_s - L_b - L_{adj} \tag{1}$$

where L_w is water-leaving radiance, L_u is the total upwelling radiance, L_r is the surface reflected radiance, L_a is the atmospheric radiance including Rayleigh scattering of gases and aerosols, L_b is the bottom reflected radiance, L_{adj} is the adjacency reflected radiance, and L_{bub} is the bubble-reflected radiance. Surface reflected radiance (L_r) is the portion of the incoming solar radiation that is reflected by the water surface (Schaepman-Strub et al. 2006). The radiance by atmosphere (L_a) includes two contributions; Rayleigh scattering of gases and aerosols (Gordon, 1997; Wang, 2010). The radiance by adjacent objects (L_{adj}) (e.g., ice, land) may cause light field distortions when they are very reflective or absorbing compared with the target to be detected (Lyapustin and Kaufman 2001). High wind speeds and breaking waves continuously produce bubble layers near the sea surface. The radiance due to bubble layers (L_{bub}) mainly affects L_w due to an increase in light scattering (Ma et al. 2015). L_w is composed by elastic (i.e., scattering) and inelastic (i.e., fluorescence) contributions (Mobley, 1994). Reflection by the bottom (L_b) in optically shallow waters can increase or decrease the water-leaving radiance depending bottom depth, inherent optical properties of water, and bottom reflectivity (Kostadinov et al. 2009).
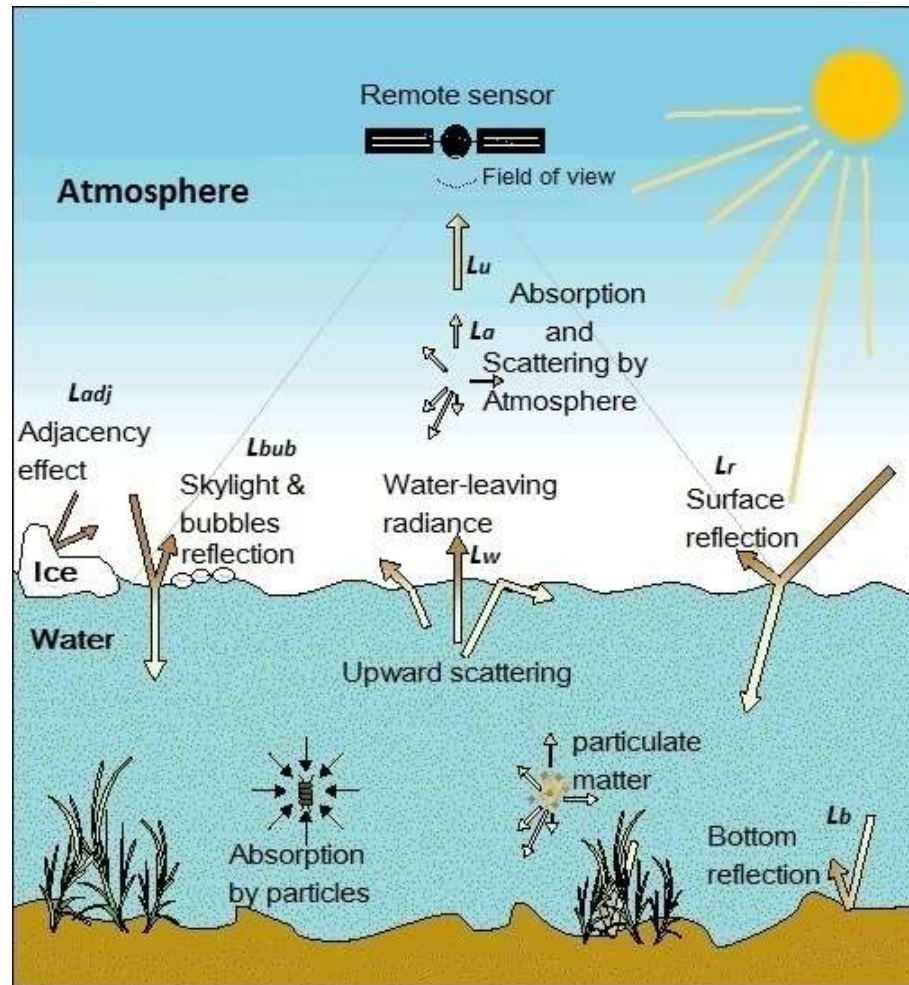
Figure 1. Factors influencing upwelling sunlight leaving the air-water interface (adapted from www.dmu.dk)

1.4 INHERENT AND APPARENT OPTICAL PROPERTIES (IOPS AND AOPS)

In optical remote sensing, two major concepts are used the most often: inherent optical properties (IOPs) of particulates that are independent of illumination conditions, and apparent

optical properties (AOPs) that closely depend on IOPs and the ambient illumination conditions (Mobley 1994). The variability in IOPs have a major influence on L_w by causing scattering and absorption of photons. Indeed, light attenuation occurs due to either absorption, or scattering of light beam from its direct path by water molecules, dissolved matter, and particulates in the medium (Mobley 1994):

$$c(\lambda) = a(\lambda) + b(\lambda) \tag{2}$$

where $a(\lambda)$ and $b(\lambda)$ are the spectral beam absorption and scattering coefficients in m^{-1} units, respectively. In a water column, the sum of absorption coefficient of all single constituents form the bulk IOP:

$$a(\lambda) = a_w(\lambda) + a_{ph}(\lambda) + a_{NAP}(\lambda) + a_{CDOM}(\lambda) \tag{3}$$

where $a_w(\lambda)$ is the absorption coefficient of water molecules. $a_{ph}(\lambda)$ is the absorption coefficient of phytoplankton, which is determined by the composition and concentration of pigments. $a_{NAP}(\lambda)$ is the absorption coefficients of non-algal particles (NAP). NAP is a composite of detritus, suspended organic matter, zooplankton, and bacteria. $a_{CDOM}(\lambda)$ is the absorption coefficient of chromophoric dissolved organic matter (CDOM). Operationally, CDOM is defined the material that passes through a filter of nominal pore size 0.2 µm (Bricaud et al. 1981). **Figure 2** shows the schematic absorption spectra of water components within visible and near IR wavelengths. $a_w(\lambda)$ is the least variable among other absorption values at given wavelengths (Pope and Fry 1997).
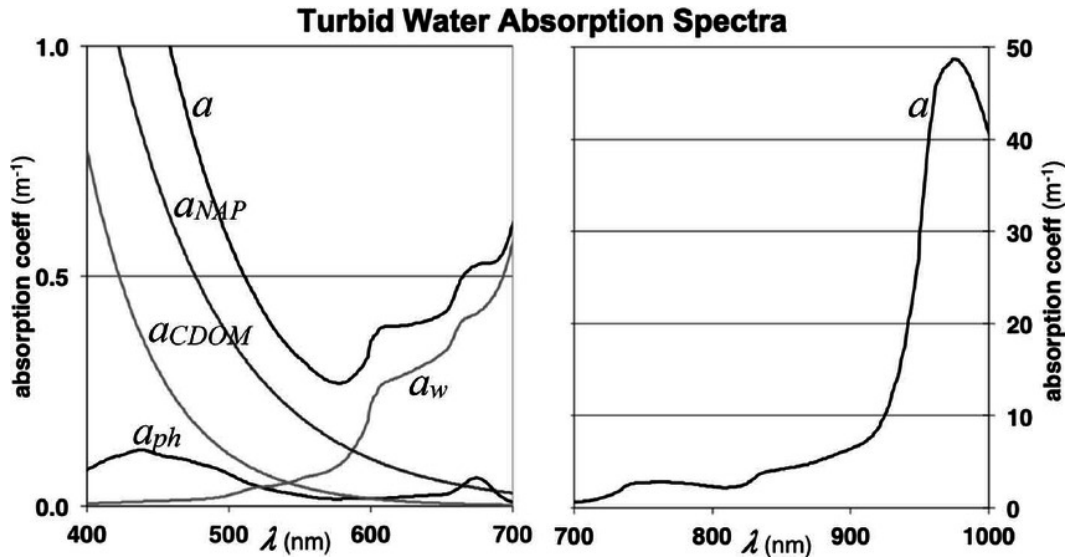
Figure 2. Light absorption components in coastal waters (Turpie 2013)

Similarly, bulk scattering and backscattering (the fraction of light scattered at angled > 90˚ relative to incident beam direction) coefficients can be written as:

$$b\,(\lambda) = b_w\,(\lambda) + b_p\,(\lambda) \tag{4}$$

$$b_b\,(\lambda) = b_{bw}\,(\lambda) + b_{bp}\,(\lambda) \tag{5}$$

where $b_w(\lambda)$, $b_p(\lambda)$, $b_{bw}\,(\lambda)$, and $b_{bp}\,(\lambda)$ are the scattering and backscattering coefficients for water and particulates, respectively. Scattering properties of particulates are directly related to computations of remote sensing reflectance. Particle scattering highly depends on size, geometry, and refractive index of all components of the particulate (Loisel et al., 2006). For instance, phytoplankton has a smaller scattering coefficient compared to other particulates in coastal waters due to the high water content (Aas, 1996), except cocolihophores that are associated with high values of scattering coefficient due to their calcium carbonate content (Balch et al., 2002).

Apparent optical properties of particulates depend on inherent optical properties and the light geometry. This concept is illustrated using the definition of R_{rs} in the relationship between IOPs and AOPs (Mobley 1994):

$$R_{rs}(\lambda) = \frac{L_w(\lambda)}{E_d(\lambda)} \tag{6}$$

where R_{rs} is a remote sensing reflectance and an AOP, L_w is water-leaving radiance, and E_d is down-welling irradiance. The forward simulation of radiance distribution due to SPM includes water-leaving radiance at a specific wavelength, $L_w(\lambda)$, and downwelling irradiance signal due to SPM just above the water surface at a specific wavelength, $E_d(\lambda,0^+)$. These variables are essential to computing the remote sensing reflectance $R_{rs}(\lambda)$ of SPM. The interrelationship between IOPs and $R_{rs}(\lambda)$ is shown as (Mobley 1994):

$$R_{rs}(\lambda) = \frac{L_w(\lambda)}{E_d(\lambda)} = \frac{f}{Q}\left(\frac{b_b(\lambda)}{a(\lambda)+b_b(\lambda)}\right) \tag{8}$$

where R_{rs} is remote sensing reflectance, $\frac{f}{Q}$ is the proportionality factor that depends on both IOPs and AOPs of particulates, $a(\lambda)$ is particles absorption coefficient, and $b_b(\lambda)$ is particle backscattering coefficient.

Variations in optical properties of water depend on the type of water body. Natural waters are classified into two water types: case 1 and case 2 waters. Case 1 corresponds to waters where chlorophyll is the major responsible for variation in optical properties within the water column. In case 1 waters, we undertake that there is a strong covariation between optical properties at any specified wavelength and the pigment concentrations. However, in Case 2 waters, components other than chlorophyll, such as yellow substances or chromophoric dissolved organic matter (CDOM) and suspended matter contribute to this covariation (Mobley 1994). Unlike case 1 waters that single-variable biogeo-optical models could be used for deriving the water optical properties, case 2 waters require more complex algorithms

due to the spectral overlap of water constituents that causes a strong dependency between different components (Zarco-Tejada et al. 2000).

1.5 OPTICAL REMOTE SENSING MODELS OF SPM

Radiative transfer models are used for developing biogeo-optical models based on IOPs of SPM and simulated radiance field. A radiative transfer model allows to track the fate of a photon in the water column, whether it is absorbed, scattered, or produced (e.g. bioluminescence). Briefly, the RTE expression is (Zaneveld et al. 2005):

$$L(\theta,\phi,z)\left[1 + \mu \frac{d}{d\tau}\right] = \omega(\tau)\int_{\Xi'} L(\theta',\phi',z)\widetilde{\beta}(\theta'\phi' \rightarrow \theta\phi)d\Omega'$$

(7)

where $L(\theta,\phi',z)$ is the incident spectral radiance in (zenith at a specific direction, azimuth) direction (θ,ϕ), $L(\theta,\phi,z)$ is the radiance created by scattering in direction (θ,ϕ) in the medium, τ is the optical depth, μ is the medium refraction index, $\widetilde{\beta}$ is the scattering phase function, $\omega(\tau)$ is the single-scattering reflectance and Ω' is the solid angle of the incident light beam. Currently there is no known general analytical solution to this equation, except when $\theta=0$ (Zaneveld et al. 2005), which incorporates a derivative and an angular integral of the solution being sought (i.e. the directional radiance field L). To estimate the AOPs from IOPs (the forward approach), one needs to numerically solve the RTE as a function of the boundary (illumination) conditions. Inherent optical properties of particles can be computed based on apparent optical properties by using inversion models.

There are two types of remote sensing reflectance models for estimating suspended and dissolved matter based on linear relationships between SPM concentration and reflectance at certain wavelengths: single-wavelength, and, multiple-wavelength models. Remote sensing

reflectance at a single wavelength has been used as a proxy to estimate the concentration of particle assemblages in numerous studies (Gordon and Castaño 1987, Nechad et al. 2003, Zhang et al. 2006). Despite wide usage, single-wavelength models are sensitive to changes in particle characteristics and associated effects on scattering and absorption (Doxaran et al. 2003). By contrast, algorithms with band ratios are less sensitive to this natural variability. Indeed, band ratios minimize second-order effects and variability due to illumination conditions (Doxaran et al. 2003, Ruddick et al. 2008). These algorithms are widely used in studying the dynamics of suspended and dissolved matter in coastal waters (Gilerson et al. 2010, Montes-Hugo et al. 2012, Mohammadpour et al. 2015).

Estimating the characteristics of particle assemblages by biogeo-optical models is associated with uncertainties due to the optical variability of particles in littoral waters. Likewise, high absorption of light within UV-green wavelengths due to CDOM may cause bias on C_{SPM} estimates due to highly absorptive characteristic within UV-blue wavelengths (Huang et al. 2012). Finally, the optical properties of particulates per unit mass at a region may change through time (Lucotte et al., 1986; Xi et al., 2013). Indeed, biogeo-optical models need to be validated within reasonably short periods due to high dynamism of littoral waters (Wei et al. 2004, Yu et al. 2016).

1.6 OPTICAL REMOTE SENSING MODELS FOR STUDYING SECOND-ORDER ATTRIBUTES OF SPM

Passive optical remote sensing techniques can be used for studying the second-order attributes of SPM (i.e., chemical composition and size distribution of SPM) in coastal waters (Neukermans et al. 2016, Woźniak et al. 2016, Organelli et al. 2016). These algorithms are constructed on particle backscattering $b_{bp}(\lambda)$ and absorption $a(\lambda)$ coefficients at specific

wavelengths. Likewise, particulate absorption coefficient $a_p(\lambda)$ has been utilized for studying the variation in organic fraction of SPM in littoral waters (Neukermans et al. 2012, Woźniak 2014). The magnitude of $b_{bp}(\lambda)$ has been used in developing algorithms for estimating particle chemical composition (Stramski et al. 2008, Martinez-Vicente et al. 2013). Likewise, the spectral slope of $b_{bp}(\lambda)$ has been anticipated to be as an indicator of particle size distribution (Loisel et al. 2006, Kostadinov et al. 2009). In summary, understanding the variation of the optical properties of the second-order attributes of SPM, plays a key role in improving biogeo-optical models in coastal waters.

1.7 MASS-SPECIFIC OPTICAL PROPERTIES OF SPM

The mass-specific absorption, σ_a, and scattering, σ_b, coefficients, known as optical cross sections of particles per unit mass, are influenced mainly by their natural characteristics such as particle composition, refractive index, density, and size distribution, due to their dependency on characteristic variations per unit mass (Neukermans et al. 2012). Optical cross-section of particulates play a key role in developing optical remote sensing models. Likewise, they are highly useful in detecting and discriminating biogeo-optical properties of particulates. Particulate mass-specific absorption and scattering coefficients are given by:

$$a_{SPM}^* = \frac{a_{SPM}}{C_{SPM}} \tag{9}$$

$$b_{SPM}^* = \frac{b_{SPM}}{C_{SPM}} \tag{10}$$

where C_{SPM} is the concentration of SPM, and a_{SPM} and b_{SPM} are the absorption and scattering coefficients of SPM, respectively. Unlike a^*_{SPM}, optical cross sections are not empirical. Instead, they must be computed based on models such as those based on Mie theory. The variation of optical cross sections of particulates depends on particle density and refractive

index. The partial regression coefficients from this multiple linear regression are the mass-specific scattering cross sections for the particulate inorganic and organic matter (PIM, POM), indicated as σ_{IOPs}^{PIM} and σ_{IOPs}^{PIM}, and are given by (Stavn and Richter 2008):

$$\sigma_{PIM}(\lambda) = \frac{\sigma_m(\lambda)}{\rho_m v_m} \tag{11}$$

$$\sigma_{PIM}(\lambda) = \frac{\sigma_o(\lambda)}{\rho_{do} f_{do} v_o} \tag{12}$$

where $\sigma_m(\lambda)$ and $\sigma_o(\lambda)$ are, the particle scattering cross sections for mineral and organic fractions of particulates, respectively, ρ is the particle density, v is the volume of a single (mineral or organic) particle, and f_{do} is the volume fraction of dry organic matter in the organic particle. Optical cross sections of particles in terms of particle size, shape, and density, play key role in the simulation of water turbidity in littoral waters through the parameterization of turbulent kinetic energy within the water column (Bowers 2003, Peng and Effler, 2012; Rottgers et al., 2014).

1.8 BIOGEO-OPTICAL WATER COMPONENTS AND HEAT TRANSFER ACROSS THE AIR-WATER INTERFACE

The attenuated solar energy in coastal waters is partially transformed to heat depending on environmental and biogeochemical conditions of the water body such as zenith angle and water turbidity. Main components affecting light absorption and temperature variation in oceanic clear waters is phytoplankton (Morel 1988). The heat transfer related to absorption is as follows (Modest 2003):

$$q \propto T^4 - T_\infty^4 \tag{13}$$

where q is the heat transfer coefficient, T_∞ is a reference temperature, and T is temperature. Any relatively warm object emits electromagnetic waves to different directions of the surrounding space by the Planck's law of black body radiation. The total exchange of heat Q_T at the air-water interface can be partitioned as (Komori et al. 1993):

$$Q_T = Q_H + Q_E + Q_R \tag{14}$$

where Q_H is the sensible heat flux, Q_E is the latent heat flux, and Q_R is the radiative heat flux in Wm^{-2} (**Figure 3**). These partitions are explained in more details in chapter 4. The relationship between radiative heat transfer and temperature fluctuation at the air-water interface is Modeled (Qiu and Kelly 1993, Isobe et al. 2014). More specifically, Manizza et al. (2005) parameterized the thermal effect of phytoplankton assemblages in terms of biological heating by:

$$q(z) = 0.58I_0 + I_{RED}e^{-k_r z} + I_{BLUE}e^{-k_b z} \tag{15}$$

Where $q(z)$ is downward radiative flux at the depth z, I_0 is surface irradiance, I_{RED} and I_{BLUE} are 21% of I_0 (reanalysis product available in NCEP-NCAR), and k_r and k_b are the attenuation coefficients at red and blue wavelengths, respectively, derived by (Morel 1988):

$$k_r = 0.225 + 0.037\ Chl^{0.629} \tag{16}$$

$$k_b = 0.0232 + 0.074\ Chl^{0.674} \tag{17}$$

Equations (15-17) approve the feedback of suspended and dissolved matter to solar radiation within UV-IR wavelengths through increasing the water surface temperature at the top layer of water column (Siegel et al. 1995, Isobe et al. 2014).
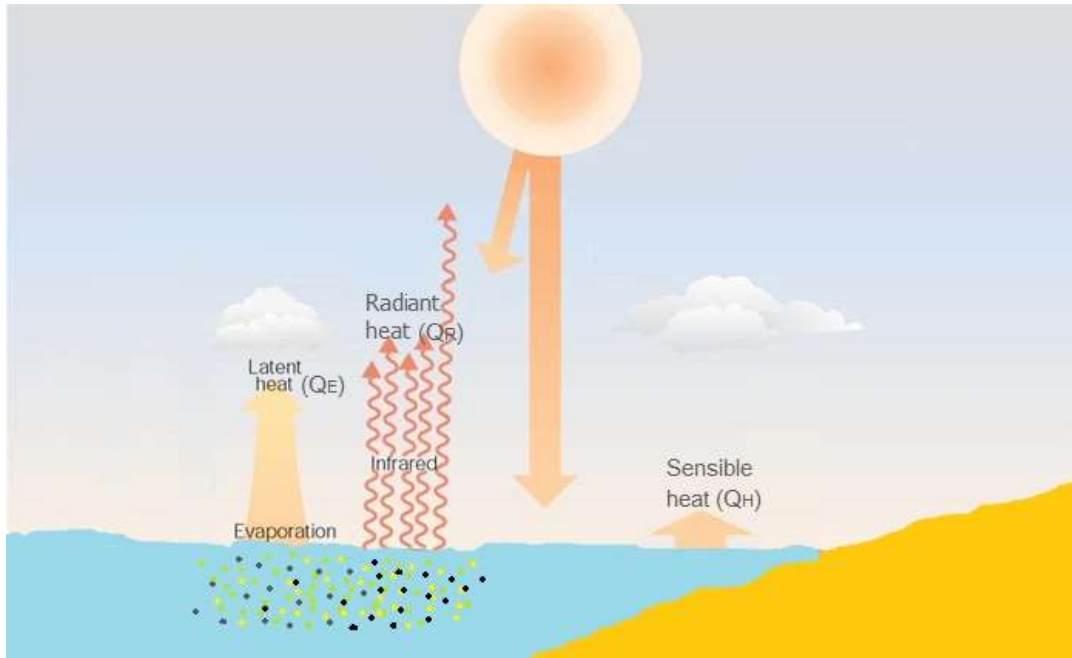
Figure 3. Heat budget components in coastal waters (adapted from www.luther.edu)

Particle-mediated heat radiation performs environmental feedbacks in coastal and estuarine waters. Indeed, biological heating contributes in modifying sea-ice cover, vertical mixing, and surface heat flux in high latitude waters (Manizza et al. 2005). The increase of the temperature at the water surface thickens the mixed layer in the atmosphere and increases the vertical velocity of air (Mechem et al. 2012). This process can slightly change the direction of weather fronts and impact the cloudiness over the target region (Senatore et al. 2014). In summary, particle mediated heat exchange at the air-water interface can play a key role in manipulating biogeochemical and environmental processes in coastal waters.

1.9 THE ST. LAWRENCE ESTUARY (SLE)

The SLE is a unique environment in terms of the dynamics of dissolved and suspended particulates, primary production, tidal currents, and resuspension processes that control the advection and turbulent diffusion of SPM (El-Sabh and Silverberg 1992). The estuary covers an area of 12,850 km^2, which begins at the upper limit of the salt-water intrusion near Quebec City, and extends 400 Km downstream to Pointe-des-Monts. The SLE is a transitional environment where the waters of the Atlantic and those of the Great Lakes converge (Forrester 1970). At the Quebec City, the drainage region of the St. Lawrence River hosts ~375 km^3 yr^{-1} of fresh water (El-Sabh and Silverberg 1990a). The SLE has been traditionally divided into two subregions such as the upper estuary, which covers the area between Ile d'Orleans and the mouth of the Saguenay fjord, and the lower estuary, which is extended from the Saguenay fjord until Pointe-des-Monts. The average depth of the upper estuary varies around 60 m with the lowest depth along the south shore of the estuary. while the lower estuary can be as deep as 250 – 400 m due to the Laurentian channel (El-Sabh and Silverberg 1992).

Considering complex physical and biogeochemical processes, the SLE is a suitable environment to develop remote sensing tools to study the biogeochemical processes and dynamics in this region, and expand those parameterizations to other estuarine and coastal waters in the world. Various studies on the SLE have revealed significant characteristics of estuarine waters and their influence on ocean color. These studies include the performance of bio-optical models on SPM estimates and the effect of particle composition on their performance (Larouche and Boyer-Villemaire 2010, Montes-Hugo et al. 2012, Montes-Hugo and Mohammadpour 2012, Mohammadpour et al. 2015), particle chemical composition (Gobeil et al. 1981, Tremblay and Gagné 2007, 2009), particle size distribution (Chanut and Poulet 1979, Poulet et al. 1986), particle dynamics (d'Anglejan and Smith 1973, Gagné et al.

2009, Coulombier et al. 2012a), physical processes (Bourgault et al. 2001, 2005, 2014), and the influences of teleconnections (Assani et al. 2010).

1.9.1 PHYSICAL PROCESSES

In the upper estuary, tidal currents are responsible for more than 90% of variations in currents (Saucier and Chassé 2000). Strong salinity gradient at the water surface characterizes this region due to the fresh water discharge by the SLR near Quebec City, which alters the salinity within the range of 0 – 20 psu from Quebec City to the mouth of the Saguenay fjord. This process intensifies the stratification conditions, and hence, weakens vertical circulations (Nieke et al. 1997). In the lower estuary, salinity varies between 20 and 30 psu due to tidal oscillations in the vertical shear of the geostrophic current. This resonant oscillation causes the density gradients to influence the upwelling zone near the mouth of the Saguenay fjord (Forrester 1970, Therriault and Levasseur 1985).

1.9.2 TIDAL CURRENTS, WAVES, AND DYNAMICS OF SPM

The SLE have salt marshes that serve to dissipate energy of tidal currents and waves. In the SLE, factors controlling the concentration of dissolved and suspended matter include the river discharge and their concentrations of geochemical traces, tide amplitude, estuarine geometry, mixing processes, and biological production. In the upper estuary, wind-driven waves and density gradient in the frontal regions cause sediment resuspension within shallow regions and the zone separating discharged fresh water of the St. Lawrence River from ocean salt water (Coulombier et al. 2012b). Likewise, the maximum turbidity zone in the upper

estuary supplies large sediments through tidal currents that induce cyclic seasonal erosion and a sedimentation rate as high as several centimeters per year (Troude and Sérodes 1990). Meybeck et al. (2003) showed the average daily yields of SPM in the SLE varied within 10 – 50 $kgkm^{-2}day^{-1}$. Likewise, the sedimentation rate from free-drifting sediment traps in the SLE moved from ~4.5 mm. $year^{-1}$ in spring to ~1 mm. $year^{-1}$ in fall (Tremblay and Gagné 2009). However, the conditions in the lower estuary are partially different from the upper estuary. The lower estuary, has more marine characteristics with respect to the upper estuary. This region is more exposed to waves and tidal currents, and tidal flats contain more fine sand. The lower estuary contains lower concentrations of suspended matter with respect to the upper estuary, which explains the role of currents and waves in particle dynamics and transport in this region (Coulombier et al. 2012a). Indeed, shear instabilities at the surface create barocliny and vertical fluxes of mass that are responsible for vertical distribution of nutrients and suspended particles (Bourgault et al. 2001). Likewise, in the lower estuary, the predominant northwesterly winds blow parallel to the southern shoreline and create the Gaspé current that displaces water mass and water constituents from the upper estuary and Saguenay fjord towards the Gulf of St. Lawrence (Koutitonsky and Bugden 1989).

1.10 OBJECTIVES

The objectives of this thesis are:

- To evaluate the performance of different optical remote sensing models for estimating SPM in SLE waters

- To determine mass-specific optical coefficients for different chemical and size fractions of SPM in SLE waters

- To review literature regarding how particulate and dissolved matter influence the surface water temperature and local climate

1.11 HYPOTHESES

To achieve our goals in this research, the following assumptions are considered:

- **First hypothesis:** Optical remote sensing can be used to obtain reliable C_{SPM} estimates in surface waters of the SLE.

- **Second hypothesis:** Second-order attributes of SPM can be estimated in SLE waters based on optical remote sensing models

1.12 GENERAL METHODOLOGY

The general methodological approach includes three tools. Firstly, field surveys for developing and validating the in-water biogeo-optical relationships. Secondly, simulations, and lastly, implementations of satellite-based models of SPM based on in-water algorithms. The first tool comprised oceanographic surveys during June 2012 and June 2013, during which, biogeochemical measurements were performed based on sampling and filtrating surface seawater (< 2m of depth) at the target stations. We performed above-water remote sensing measurements during the 2012 survey, to determine apparent optical properties of surface water. The data obtained were used for developing optical proxies to estimate the SPM concentration in the SLE. Likewise, we measured particle attenuation and absorption coefficients and particle size distribution at each target station during June 2013. Those

measurements allowed us to characterize optical cross sections of particles based on particle mass, chemical composition, and size distribution in the sampling region during this period.

The third and final tool we used was a radiative transfer model (Hydrolight 2.0, *Sequoia* Inc.) constrained by in situ measured IOPs, in order to simulate remote sensing reflectance (R_{rs}) values of MERIS spectral band ratios $R_{rs}(708)/R_{rs}(665)$ and $R_{rs}(753)/[R_{rs}(665)-R_{rs}(708)]$. In general, the combination of these measurements and methods allowed us to achieve the specified objectives, although they individually have their advantages and disadvantages.

1.13 STRUCTURE OF THE THESIS

The thesis is divided in five chapters. The first chapter covers the general introduction, explaining the essential perceptions about optical remote sensing and optical properties of water constituents in coastal regions. In the second chapter, we will explain the fundamental concepts of particle optics and the effects of particle concentration on bio-optical proxies. Moreover, we will discuss the influence of particles chemical composition on the satellite-derived SPM concentration. The third chapter explains how chemical composition and size distribution of particles affect the particle optical cross sections in our study area. Likewise, it considers the effect of particle size distribution and chemical composition on the optical proxies enlisted to estimate SPM concentration. The fourth chapter reviews the role of particles in radiant heat transfer and their influence on the variation of SST. The effect of teleconnections on particle concentration and attributes within estuarine and complex case II waters – with an interest in the SLE – have also been described. Finally, the fifth chapter covers the general conclusions and perspectives of the thesis.

CHAPTER 2

EFFETS DE LA COMPOSITION DES PARTICULES SUR LES MATIERES EN SUSPENSION DÉRIVÉE DE MERIS : UNE ETUDE SUR L'ESTUARE DE SAINT- LAURENT

Ce premier article, intitulé « *Particle composition effects on MERIS-derived SPM: a case study in the Saint Lawrence Estuary»*, fut corédigé par moi-même ainsi que par les professeurs Martin A. Montes-Hugo, Robert Stavn, Jean-Pierre Gagné, et Pierre Larouche. Il fut accepté pour publication dans sa version finale en 2015 par les éditeurs de la revue *Canadian Journal of Remote sensing*. En tant que premier auteur, ma contribution à ce travail fut l'essentiel de la recherche sur l'état de l'art, le développement de la méthode, et l'exécution des tests de performance. Le professeur Martin A. Montes-Hugo, second auteur, a fourni l'idée originale. Il a aidé à la recherche sur l'état de l'art, au développement de la méthode ainsi qu'à la révision et la rédaction de l'article. Les professeurs Robert Stavn, Jean-Pierre Gagné, et Pierre Larouche ont aidé à la recherche sur l'état de l'art ainsi qu'à la révision de l'article. Une version abrégée de cet article a été présentée à la conférence *International Geoscience and Remote Sensing Symposium, à Québec* (*Québec, Canada*) à l'été 2014.

Mohammadpour G., Montes-Hugo M.A., Stavn R., Gagne J.P., Larouche L. Particle composition effects on MERIS-derived SPM: a case study in the Saint Lawrence Estuary. Canadian Journal of Remote Sensing. Vol. 41, issue 6, 2015, doi: 10.1080/07038992.2015.1110012

Résumé

Un modèle optique empirique pour estimer la concentration de particules en suspension (C_{SPM}) a été développé dans la partie supérieure de l'estuaire du Saint-Laurent, basé sur la réflectance (R_{rs}) mesurée par télédétection correspondant aux canaux spectraux 7 et 9 (centrés sur des longueurs d'onde de 665 et 708 nm, respectivement) du capteur MERIS (Medium Résolution Imaging Spectromètre). La sensibilité de C_{SPM} au changement du contenu en minéraux des particules en suspension a été examinée en utilisant des valeurs simulées de Rrs. Pour les mesures de juin 2012, les valeurs observées de $R_{rs}(708)/R_{rs}(665)$ en fonction de C_{SPM} peuvent être modélisées par une relation de type puissance ($y = 235.7\ x^{8.321}$, $r^2 = 0.7$, $N = 10$). De plus, des simulations numériques et une analyse de régression de type II révèlent que le paramètre exposant de ce modèle biogéo-optique diminue lorsque les particules en suspension deviennent plus riches en matière organique.

PARTICLE COMPOSITION EFFECTS ON MERIS-DERIVED SPM: A CASE STUDY IN THE SAINT LAWRENCE ESTUARY

Mohammadpour Gholamreza[1], Martin A. Montes-Hugo[1*], Robert Stavn[2,3], Jean-Pierre Gagné[1], Pierre Larouche[4]

[1]Institut des Sciences de la Mer de Rimouski, Université du Québec à Rimouski, 310 Allée des Ursulines, Office P-216, G5L 3A1, Rimouski, Québec, Canada

[2]Visiting scientist, Naval Research Lab, Stennis Space Center, MS, USA

[3]Department of Biology, University of North Carolina/Greensboro, USA

[4]Institut Maurice-Lamontagne, Pêches et Océans Canada, Québec, Canada

[*]Author to whom correspondence should be addressed; Tel.: +1-418-723-1986 (ext. 1961), Fax: +1-418-724-1842, E-Mail: martinalejandro_montes@uqar.ca

Abstract. An empirical optical model for estimating the concentration of suspended particulate matter (C_{SPM}) was developed in the upper part of the Saint Lawrence Estuary based on remote sensing reflectance (R_{rs}) measurements corresponding to MERIS (MEdium Resolution Imaging Spectrometer) spectral channels 7 and 9 (i.e., centered wavelengths 665 and 708 nm, respectively). Sensitivity of C_{SPM} estimates to changes on mineral content of suspended particulates was investigated based on simulated R_{rs} values. For June 2012 measurements, C_{SPM} varied with $R_{rs}(708)/R_{rs}(665)$ values following a power-type relationship ($y = 235.7\,x^{8.321}$, $r^2 = 0.7$, $N = 10$). Also, numerical experiments and analysis of regression type II showed that exponent parameter of this biogeo-optical model decreased as suspended particulates become more enriched in organic matter.

2.1 INTRODUCTION

The study of the distribution of suspended particulate matter (SPM) in littoral environments has several applications in civil engineering and ecology including the characterization of coastal erosion patterns (Fettweis et al., 2012), the monitoring of harmful algae blooms (Miller et al., 2006), and the managing of fisheries (Gernez et al., 2014). The characterization of SPM dynamics based on discrete ship-based measurements is costly in estuarine and coastal areas due to the large temporal and spatial variability of water constituents. Overcoming these limitations is possible by performing a synoptic mapping of SPM based on optical measurements derived from satellite sensors (Miller and McKee, 2004). Although several remote sensing algorithms based on visible and near-infrared (NIR) wavelengths have been proposed for characterizing the concentration of SPM (C_{SPM}) in littoral surface waters (Doxaran et al., 2002; D'Sa et al., 2007; Nechad et al., 2009; Montes-Hugo and Mohammadpour, 2012), their use cannot be generalized across different environments due to variations in regression model coefficients associated with changes in water optical composition including variability of particle attributes (e.g., mineral content).

Here we investigate how parameters of an empirical biogeo-optical relationship for estimating C_{SPM} and based on MERIS (MEdium Resolution Imaging Spectrometer) radiometric bands 7 and 9 (i.e., centered wavelengths 665 and 708 nm, respectively) are influenced by changes in particle chemical composition. The experiments were conducted with samples obtained in the upper part of the Saint Lawrence Estuary (SLE) and during June of 2012. The main working hypothesis states that non-linear variation of remote sensing reflectance ratio $R_{rs}(708)/R_{rs}(665)$ as a function of C_{SPM} is strongly related to particle composition changes as reflected by mineral enrichment of suspended particulate matter.

This deviation from linearity is linked to the combination of two SPM chemical components (i.e., mineral vs organic matter) with different indices of refraction.

The results of this contribution have three important applications. First, they will help to generalize biogeo-optical models of C_{SPM} across different littoral environments. Second, they will provide key information about the bias of C_{SPM} estimates due to changes in particle composition. Lastly, they will be useful for estimating the fraction of inorganic material in suspended solids if the relationship between C_{SPM} and R_{rs} is known *a priori*.

2.2 METHODS

2.2.1 STUDY AREA

The lower estuary waters are brackish (salinity = 0-25 psu), relatively shallow (i.e., bottom depth < 50 m), and characterized by high spatial and sub-daily variations of C_{SPM} values (1 to 400 g m^{-3}) (Yeats, 1988). Minerals dominate the chemical composition of suspended particulates by contributing up to 95% of SPM mass (Sundby, 1974; Yeats, 1988). The size spectrum of suspended particulates is strongly influenced by the presence of small particles (~5 μm in diameter) (Poulet et al., 1986). The concentration of CDOM or chromophoric dissolved organic matter, as reflected by its absorption coefficient (a_{CDOM}), is very high (up to 2 m^{-1} at 412 nm) with respect to other SLE sub-regions (Nieke et al., 1997).

2.2.2 DATASETS

Field surveys were performed during June 14 of 2012 and encompassed 10 locations situated NE of the Orleans Island (M1 to M10, Figure 1). Discrete water samples for chlorophyll a concentration (chl), a_{CDOM}, C_{SPM}, and concentration of particulate inorganic

matter (C_{PIM}) were obtained at 2 m depth by using a Niskin bottle (12 L). Also at each location, spectral radiance measurements for remote sensing reflectance calculations were made with a hand-held radiometer (see Above-water radiometric measurements).
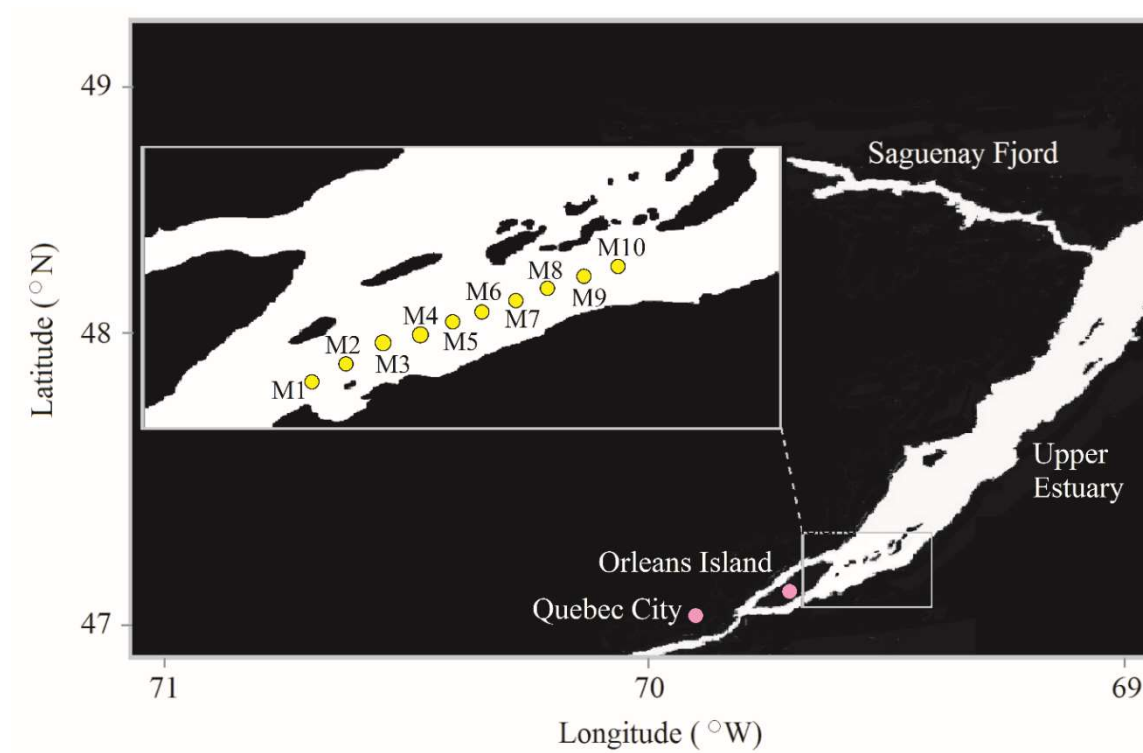
Figure 1. Study area; sampling locations during June 2012 (M1 to M10, inset A)

2.2.3 BIOGEOCHEMICAL ANALYSIS

The concentration of SPM in g m^{-3} was measured gravimetrically after filtering a volume of seawater through pre-weighed GF/F filters (47 mm, pore size = 0.7 μm, Whatman) (Aminot and Chaussepied, 1983). The precision of C_{SPM} determinations was 15%. The inorganic fraction of SPM was obtained after removing the organic components of the original sample by combustion at 450°C for 6 h. The analysis of Chl includes the following steps: 1) filtration of 0.5 L samples using GF/F membranes (25 mm, pore size = 0.7 μm Whatman), 2) storage of samples in liquid nitrogen and during 72 h, 3) 24-h extraction of pigments in cold (i.e., 4-5°C) 90% acetone and dark conditions, and 4) fluorescence measurements of extracted samples and standards (Mueller et al., 2003). The Fluorometer used in this study (TD-10AU, Turner Designs) allowed Chl determinations with a precision of 4%. Water samples for a_{CDOM} determinations were obtained with clean amber glass bottles and immediately filtered through 0.2 μm membranes (nucleopore, Whatman). Filtrates were kept in dark conditions at 4°C till processing at ISMER. Spectral a_{CDOM} measurements were performed with a dual beam UV-visible spectrophotometer (Perkin-Elmer Lambda-35) and using Nanopure water as a baseline (Mueller et al., 2003).

2.2.4 ABOVE-WATER RADIOMETRIC MEASUREMENTS

The radiometric data were collected under clear skies and calm wind conditions (i.e., wind speed < 4 ms^{-1}, wave height < 0.3 m) using a portable spectrometer (ASD FieldSpecPro RS, spectral range = 350-1000 nm, spectral resolution 10 nm). Spectral radiance measurements of sky and water components were obtained at 1 m from the air-water interface. To compute R_{rs}, three types of radiance measurements were made: the total water upwelling radiance, L_u, the sky radiance, L_{sky}, and the reference radiance, L_g:

$$R_{rs}(\lambda) = \rho_g(\lambda) \, (L_u(\lambda) - F_r(\lambda) \, L_{sky}(\lambda))/(\pi \, L_g(\lambda)) \tag{1}$$

$$E_d(\lambda) = \pi \, L_g(\lambda)/\rho_g(\lambda) \tag{2}$$

where F_r is the Fresnel reflectivity, L_u - $F_r \, L_{sky}$ is equivalent to the water leaving radiance (L_w), and E_d is the downwelling irradiance. Upward (i.e., L_u and L_g) and downward (i.e., L_{sky}) radiance components were measured at 40° with respect to the vertical, and 135° with respect to the solar azimuth (Mobley, 1994). The final magnitude of L_u, L_{sky} and L_g was computed by averaging three samples having an integration time of 0.65, 0.14, and 0.03 s, respectively. F_r is equal to 0.02 and $F_r \, L_{sky}$ represents the E_d fraction due to diffuse photons going to the ASD sensor after being retro-reflected against the air-water interface. L_g is measured using a Spectralon plaque with a known spectral reflectivity (i.e., ρ_g = 0.995 and 0.998 at a wavelength λ of 665 and 708 nm, respectively) and assuming a Lambertian reflectance distribution function.

2.2.5 CORRECTIONS DUE TO SENSOR DIFFERENCES

To obtain synthetic MERIS-derived R_{rs} values, *in situ* R_{rs} measurements were weighted by the response function of the spaceborne imager (Froidefond et al., 2004):

$$R_{rs}(j) = \frac{\sum_{i=\lambda min}^{i=\lambda max} L_w(\lambda) S_{i,j}(\lambda)}{\sum_{i=\lambda min}^{i=\lambda max} E_d(\lambda) S_{i,j}(\lambda)} \tag{3}$$

where i is the wavelength and j stands for MERIS radiometric channels 7 and 9, $S_{i,j}(\lambda)$ is the spectral sensitivity of MERIS (Vermote et al., 2006).

2.2.6 SIMULATED PARTICLE COMPOSITION EFFECTS

The impact of variable mineral content of SPM on $R_{rs}(708)/R_{rs}(665)$ variations and subsequent changes on regression coefficients of C_{SPM}- $R_{rs}(708)/R_{rs}(665)$ relationship was modeled based on synthetic R_{rs} derived from the quasi-analytical algorithm (Lee et al., 2009):

$$R_{rs}(\lambda) = 0.52/(1/r_{rs})-1.7) \tag{4}$$

$$r_{rs}(\lambda) = ((0.249\ u(\lambda) + 0.0895)^2 - 0.008)/0.499 \tag{5}$$

$$u(\lambda) = b_b(\lambda)/(a(\lambda) + b_b(\lambda)) \tag{6}$$

The total backscattering coefficient (b_b) was computed as the sum of water and particulate contributions:

$$b_b(\lambda) = 0.5\ b_w(\lambda) + b^{PIM}(\lambda)\ b_{eff}{}^{PIM} + b^{POM}(\lambda)\ b_{eff}{}^{POM} \tag{7}$$

$$b^{POM} = \sigma_b{}^{POM}\ C_{POM} \tag{8}$$

where b_{bw} is the backscattering coefficient of pure seawater and equivalent to one half of the scattering coefficient of pure seawater (Morel, 1974). This approximation holds since forward and backward scattering contributions by a water molecule are comparable. b^{PIM} and b^{POM} are the scattering coefficients for particulate inorganic and organic matter, respectively, $b_{eff}{}^{PIM}$ and $b_{eff}{}^{POM}$ are the backscattering efficiencies (i.e., backscattering coefficient over scattering coefficient ratio) for mineral (0.02) and organic (0.012) particulate compounds, respectively, C_{POM} is the concentration of particulate organic matter in g m^{-3}. Notice that magnitude of $b_{eff}{}^{POM}$ corresponds to an intermediate value between typical backscattering ratios of phytoplankton (0.007) and non-algal particulates (0.016) (Bukata et al., 1981).

The calculation of the total absorption coefficient (a) included four components:

$$a(\lambda) = a_w(\lambda) + a_{CDOM}(\lambda) + a^{PIM}(\lambda) + a^{POM}(\lambda) \tag{9}$$

where a_w is the pure seawater absorption coefficient (Pope and fry, 1997), a^{PIM} and a^{POM} are the absorption coefficients for inorganic and organic particulate matter, respectively. Based on ship measurements (Montes-Hugo and Mohammadpour, 2012), mean $a_{CDOM}(665)$ and

$a_{CDOM}(708)$ values of 0.066 and 0.045 m^{-1}, respectively, were chosen over the whole SLE. The value of a^{PIM} was calculated as the product between C_{PIM} and the mass-specific absorption coefficient of PIM ($\sigma_a^{PIM}(\lambda)$). The magnitude of σ_a^{PIM} was 0.01975 and 0.01778 $m^2\ g^{-1}$ at 665 and 708 nm, respectively (Ahn, 1990). The values of $a^{POM}(\lambda)$ were derived as:

$$a^{POM}(\lambda) = \sigma_a^{SPM}(\lambda)\ C_{SPM} - a^{PIM}(\lambda) \tag{10}$$

The mass-specific absorption cross section for the absorption coefficient of SPM (σ_a^{SPM}) has been set to the arithmetic average of C_{SPM}-normalized particulate absorption coefficients measured during May 2000 and April 2001 cruises. σ_a^{SPM} was 0.0242 and 0.0034 $m^2\ g^{-1}$ at 665 and 708 nm, respectively. To avoid negative $a^{POM}(708)$ estimates, a constant value of 0.0002 m^{-1} was used (Röttgers et al., 2014). Theoretical experiments were performed using ten C_{SPM} concentrations (0.1, 0.5, 1, 3, 5, 10, 20, 100, 300, 500 g m^{-3}) consistent with a realistic range of values reported in the SLE by previous studies (Sundby, 1974; Yeats, 1988). Also, simulations were initialized with five C_{PIM}/C_{SPM} ratios (1,0.8,0.5,0.2 and 0) encompassing extreme and intermediate cases.

2.2.7 STATISTICAL ANALYSIS

The relationship between C_{SPM} and MERIS-adjusted $R_{rs}(708)/R_{rs}(665)$ measurements was analyzed based on a power regression type II function (i.e., dependent and independent variables are randomly chosen):

$$C_{SPM}^{MERIS} = A\ [R_{rs}(708)/R_{rs}(665)]^B \tag{11}$$

where A and B are regression coefficients as derived from the Levenberg-Marquardt algorithm (Levenberg,1944).

2.3 RESULTS

2.3.1 BIOGEO-OPTICAL RELATIONSHIPS

Examples of remote sensing reflectance spectra measured in the upper estuary and during June 2012 are shown in **Figure 2**. Despite the increase of the spectral slope of R_{rs} within the red-NIR as C_{SPM} increases, the quotient between $R_{rs}(708)$ and $R_{rs}(665)$ values are larger at higher water turbidities. The graph clearly illustrates the augmentation of the spectral slope within the red-NIR as C_{SPM} increases. This is the foundation of the parameterization proposed in equation 10. The resulting empirical model of C_{SPM} as a function of $R_{rs}(708)/R_{rs}(665)$ is depicted in **Figure 3**. This parameterization explained more than two- thirds of the regression variability, and was valid for a C_{SPM} range of 4.9-18.5 g m^{-3} (**Figure 3a**, **Table 1**). Likewise, it was found that $R_{rs}(708)/R_{rs}(665)$ changes were strongly related (i.e., more than 50% of regression variability) to variations on the mineral content of SPM (**Figure 3b**). As expected, the spatial distribution of C_{SPM} during the spring surveys was far from being homogeneous. Indeed, C_{SPM} varied more than 3-fold (i.e., 4.9 to 18.5 g m^{-3}) in less than 2 km (**Figure 3a**). This was also true for C_{PIM}/C_{SPM} values (e.g., 0.57 at M10 and 0.79 at M3, **Figure 1,3b**).
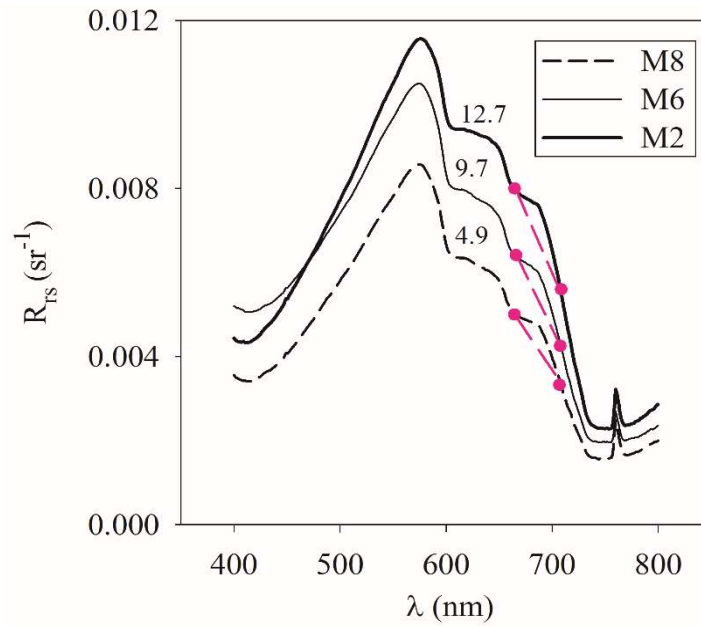
Figure 2. Spectral remote sensing reflectance spectra in the SLE. Number next to each Rrs curve indicates the concentration of SPM measured in situ, wavelengths used in equation (11) (pink solid circles), spectral Rrs slopes (pink broken line).

Table 1. Biogeo-optical relationships of C_{SPM} as a function of $R_{rs}(708)/R_{rs}(665)$. Regression parameters are derived from the equation: $y = A\,x^B$. Within parentheses two standard errors. The number of observations in each case (N) was 10.

	A	B	r^2
C_{SPM}	235.7 (171.1)	8.321 (4.016)	0.687
C_{PIM}/C_{SPM}	1.535 (0.720)	2.069 (1.240)	0.592
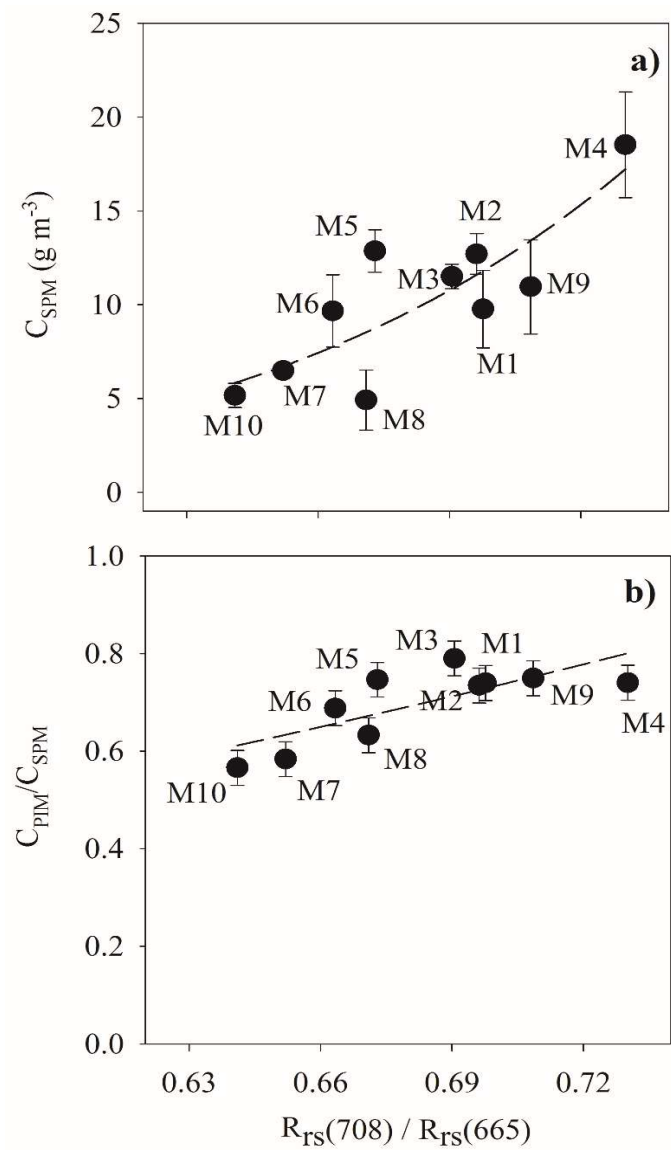
Figure 3. Biogeo-optical relationships for estimating C_{SPM}. a) C_{SPM} versus $R_{rs}(708)/R_{rs}(665)$, b) C_{PIM}/C_{SPM} versus $R_{rs}(708)/R_{rs}(665)$. Labels of data points identify each sampling location, power-type regression model (dash line).

2.3.2 SENSITIVITY OF C$_{SPM}$ ESTIMATES TO PARTICLE COMPOSITION

As highlighted in the previous section, the magnitude of $R_{rs}(708)/R_{rs}(665)$ was substantially influenced not only by the first-order properties (i.e., concentration) but also by second-order properties (i.e., chemical composition) of suspended particulates. The inorganic enrichment of SPM and its impact on SPM optical properties is illustrated in Figure 4. As stated in introduction, our power-type model predicted a flattening of the curve as mineral particles become replaced by organic compounds (**Figure 4a**). In fact, minimum and maximum values of *B* (3.04 and 14.47, respectively) corresponded with the smallest and largest C$_{PIM}$/C$_{SPM}$ (0 and 1, respectively) values studied here (**Table 2**). Notice that these results encompassed a broader interval of C$_{SPM}$ values with respect to those measured in the SLE during June 2012. However, the impact of increasing C$_{PIM}$/C$_{SPM}$ on $R_{rs}(708)/R_{rs}(665)$ was also present at C$_{SPM}$ values smaller than 20 g m^{-3} (**Figure 4b**). Indeed, modeled values suggest that optically-derived C$_{SPM}$ estimates may change in 100% (e.g., from 10 to 20 g m^{-3}) if C$_{PIM}$/C$_{SPM}$ varied from 0.5 to 1.
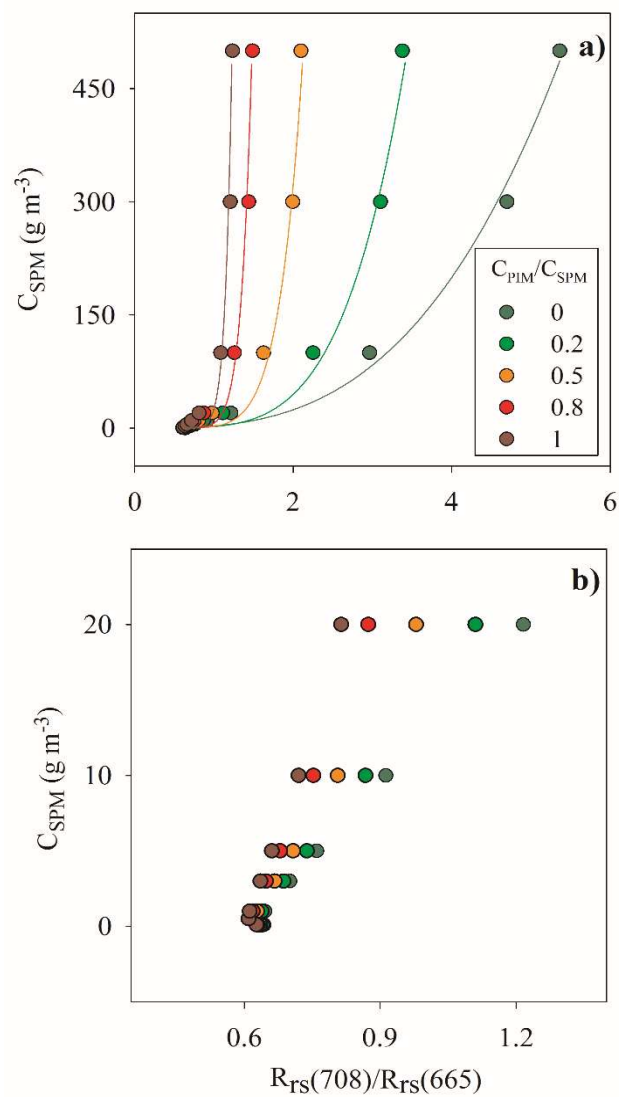
Figure 4. Simulated particle composition effects on C_{SPM} estimates. a) Variation of C_{SPM} as a function of $R_{rs}(708)/R_{rs}(665)$ for particle assemblages having different chemical composition, power-type regression models (solid lines), b) idem to a) but for the C_{SPM} range measured during June 2012.

Table 2. Simulated influence of mineral content of particulates on $R_{rs}(708)/R_{rs}(665)$ variability. Definition of regression parameters, uncertainties, and N as the list of abbreviations and acronyms.

C_{PIM}/C_{SPM}	A	B	r^2
0	2.963 (2.300)	3.036 (0.476)	0.994
0.2	1.923 (1.980)	4.540 (0.842)	0.992
0.5	2.003 (1.950)	7.398 (1.457)	0.991
0.8	5.252 (5.163)	11.360 (2.523)	0.990
1	20.020 (13.892)	14.990 (3.426)	0.989

2.4 DISCUSSION

2.4.1 REMOTE SENSING OF C_{SPM} AND C_{PIM}/C_{SPM}

A power-type remote sensing model based on visible-NIR wavelengths was used in this study for investigating the impact of particle chemical composition on MERIS-derived C_{SPM} estimates. The proposed C_{SPM} model is not sensitive to CDOM variations and sunlight geometry, thus it is ideal for investigating biogeo-optical changes due to different particle assemblages. A remarkable result in this study was the positive correspondence between $R_{rs}(708)/R_{rs}(665)$ ratios and C_{PIM}/C_{SPM} values. This strong linkage was not anticipated since variations due to second-order attributes of particulates are reduced when models are constructed based on R_{rs} band ratios (Doxaran et al., 2003). However, Wozniak et al. (2010) found that optical cross sections of particulate absorption and scattering coefficients (i.e., concentration-normalized IOPs) are very changing within the spectral interval 665-708 nm. Thus, to quantify the spectral response of R_{rs} to particle composition modifications in the upper estuary, a power-type model was suggested based on data reported in the literature and field measurements obtained in SLE waters. These simulations showed that C_{PIM}/C_{SPM} can be estimated from the exponent B based on the following function: $y = y_0 + y_1 \ln(x)$ ($y_0 = -0.745 \pm 0.086$, 2 standard errors, $y_1 = 0.646 \pm 0.042$, $r^2 = 0.996$, $N = 10$). By applying this expression to regression parameters in **Table 1**, the resulting C_{PIM}/C_{SPM} value (0.624) was within the interval of values (0.57-0.75) measured during June 2012 in the upper estuary.

2.4.2 THE ORIGIN OF BIOGEO-OPTICAL COVARIATIONS

Any inherent optical property j can be computed as the product σ_j^i $[C]^i$, where $[C]^i$ is the concentration of the component i, thus the use of R_{rs} band ratios make models to be independent of $[C]^i$ terms. However, the influence of spectral variations driven by mass-specific optical cross sections is preserved. These linkages are shown below for the band ratio applied in this study:

$$R_{rs}(708)/R_{rs}(665) = k \ (b_b(708)/ \ b_b(665) \ [(a(665)+ b_b(665)][a(708)+ b_b(708)]^{-1} \qquad (12)$$

$$b_b(\lambda) = 0.5 \ b_w(\lambda) + \sigma_{b_{bp}}^{SPM} C_{SPM}, \text{ and } a(\lambda) = a_w(\lambda) + \sigma_{a_p}^{SPM} C_{SPM} \qquad (13)$$

where b_{bp} and a_p are the particulate backscattering and absorption coefficients, respectively.

As a first order approximation, k is equal to 1 since the weak spectral variability of f/Q factors within the NIR range and associated to changes on solar illumination, sea-surface geometry, and inherent optical properties of the water (Morel and Gentili, 1996).

Dependencies between mass-specific optical cross sections and particle characteristics have been already investigated in littoral environments but based on single wavelengths. In coastal waters of UK, it was shown a positive covariation between the mass-specific scattering coefficient of minerals as derived from *in situ* optical measurements at $\lambda = 665$-670 nm and the inverse of the apparent density of particulates (Bowers et al., 2009). In coastal and offshore waters of Europe, the magnitude of the mass-specific particulate backscattering coefficient measured at $\lambda = 650$ nm was directly related to the proportion of organic carbon of SPM (Neukermans et al., 2012).

Three more questions are keys to understand relationships found in **Figure 3**: Is scattering or absorption of particulates the main optical process modulating $R_{rs}(708)/R_{rs}(665)$

variations? Which second-order particle attributes are responsible of these changes? Why the biogeo-optical functionalities become less linear as C_{SPM} or C_{PIM}/C_{SPM} increases? Regarding the first question, the spectral influence of particulate absorption and scattering (b_p) coefficients on $[a_p(665) \; b_p(708)] \; [a_p(708) \; b_p(665)]^{-1}$ ratios was examined based on in-water optical measurements obtained in the SLE during June 2013 (Appendix, **Figure A1**). This sensitivity analysis suggested that variability of $[a_p(665) \; b_p(708)] \; [a_p(708) \; b_p(665)]^{-1}$ was mainly driven by particulate absorption changes (**Figure A2a**). Although potential changes on $R_{rs}(708)/R_{rs}(665)$ due to spectral particulate backscattering variability were not analyzed, it can be said that variations on $b_{bp}(708)/b_{bp}(665)$ were probably secondary as b_{bp} strongly correlates ($r^2 = 0.96\text{-}0.98$) with b_p (Cizmeli, 2008), and spectral b_p variations were not connected to $[a_p(665) \; b_p(708)] \; [a_p(708) \; b_p(665)]^{-1}$ changes (**Figure A2b**).

With respect to the second question, it is possible that dependencies observed between $R_{rs}(708)/R_{rs}(665)$ and C_{PIM}/C_{SPM} values were also partially influenced by additional properties of particulates such as particle size. Although size distributions of SPM were not measured during June 2012, additional data obtained over the SLE during June 2013 showed an inverse covariation between C_{PIM}/C_{SPM} and the average diameter of particulates as derived from the Sauter parameter (ϕ_m) (**Figure A3**). Thus, the additive effect of particle size on $R_{rs}(708)/R_{rs}(665)$ variations and subsequent changes of B is likely present and may not be ignored in our study area.

By focusing in question 3, the regression analysis suggested a non-linear behavior of $R_{rs}(708)/R_{rs}(665)$-C_{SPM} and $R_{rs}(708)/R_{rs}(665)$-C_{PIM}/C_{SPM} relationships. These deviations were likely attributed to spectral variations on optical cross sections associated to chemical and physical changes on non-algal particulates (NAP) as the SPM load increases. In coastal waters of California, particle assemblages dominated by organic and inorganic particulate components were characterized by relatively high (~ 6.7 in average) and low (~ 2) $a_p(665)^*/a_p(708)^*$ values, respectively (Wozniak et al., 2010). Likewise, for the same samples, the mean value of $b_p(708)^*/b_p(665)^*$ was found to be higher for organic-rich SPM

samples. This implies that rate of change of $[a_\mathrm{p}(665)\, b_\mathrm{p}(708)]\, [a_\mathrm{p}(708)\, b_\mathrm{p}(665)]^{-1}$ values will decrease as C_SPM and $C_\mathrm{PIM}/C_\mathrm{SPM}$ increase due to the replacement of organic-dominated NAP by inorganic-dominated NAP. These spatial biogeo-optical modifications have been already reported in other coastal environments with comparable turbidities to those measured in the SLE (Doxaran et al., 2012). Lastly, the influence of PIM and POM analytical errors on aforementioned $a_\mathrm{p}{}^*$ and $b_\mathrm{p}{}^*$ spectral dependencies are expected to be secondary because changes in $a_\mathrm{p}{}^*(665)/a_\mathrm{p}{}^*(708)$ and $b_\mathrm{p}{}^*(708)/b_\mathrm{p}{}^*(665)$ due to underestimation (overestimation) of C_PIM (C_POM) are likely small (i.e.,~10%).

2.5 CONCLUSIONS

In this contribution, we demonstrated the influence of different SPM compositions on MERIS-derived C_SPM in very turbid environment of the SLE. Although MERIS mission finished in April 2012, ocean color spaceborne imagers having similar bands are expected to be launched in 2015 (e.g., Sentinel-3). Thus, the results obtained in this study are not restricted to MERIS observations and may also be useful in future satellite ocean color imagers. An important lesson derived here was the potential use of B as an optical proxy for discriminating waters with different particle chemical composition. This approach does not require of specific algorithms of C_PIM since $C_\mathrm{PIM}/C_\mathrm{SPM}$ fractions can be estimated from the exponent parameter of the C_SPM-$R_\mathrm{rs}(708)/R_\mathrm{rs}(665)$ function. Likewise, the suggested inversion may be generalized to other environments having comparable water optical properties. Indeed, the atmospheric correction can be achieved, even in these highly turbid waters. This may be problematic given the fact that the black pixel assumption of negligible L_w in the NIR may not hold in these waters.

2.6 ACKNOWLEDGEMENTS

2.8 APPENDIX

2.8.1 SHIPBOARD OPTICAL MEASUREMENTS

Spectral measurements of a and c coefficients were performed onboard using an absorption-beam attenuation meter (ac-s, WetLabs). Discrete samples were obtained at 2 m depth and using Niskin bottles attached to an oceanographic rosette. Sampling locations during June 2013 are depicted in Figure A1. The ac-s has a spectral range of 400-730 nm, a path length of 10 cm, a spectral resolution of 4 nm, and an accuracy of ± 0.001 m^{-1}. In order to minimize the presence of bubbles, a pump (ISMATEC MCP-Z) was used to gently circulate the samples thru the ac-s tubes. Remaining signal spikes related to bubbles were removed by visual inspection. A posteriori, a and c values were corrected by water temperature and salinity variations (Pegau et al., 1997), and residual scattering effects were removed from resulting absorption coefficients following Zanaveld's approach (Zanaveld et al., 1994). The magnitude of a_{CDOM} was also measured using the ac-s by filling each tube with seawater previously pre-filtered through a 0.2 μm polycarbonate membrane (Isopore, track-etched polycarbonate, 47 mm in diameter, Millipore). The magnitude of a_p was derived by subtracting a_w and a_{CDOM} from a. Likewise, b_p values at each wavelength were computed by subtracting a from c, and removing water contribution from the total scattering coefficient (b).

2.8.2 ANALYSIS OF PARTICLE SIZE

The particle size spectra of discrete water samples were measured using a red laser (wavelength = 670 nm) diffractometer (LISST-100X, type B, Sequoia Scientifics) equipped

with a chamber and a magnetic stir bar. The LISST-100X instrument can measure 32 size classes of particulates with a diameter between 1.25 to 250 μm, however only the interval 3-170 μm was analyzed due to instrument artifacts (e.g., stray light) in the first bins (i.e., < 3 μm) and bias related to particle sinking in the last bin (i.e., 170-250 μm) (Reynolds et al., 2010). Measurements were made during a period of 3 minutes at 1 Hz, and resulting raw data were quality controlled by using the Hampel filter algorithm (Pearson, 2005). The Sauter parameter or mean diameter of particulates weighted area by the cross-sectional area concentration of particles (φm) (Sauter, 1928) was calculated for each sampling location based on LISST measurements made within the size interval 3-170 μm (Neukermans et al., 2012).
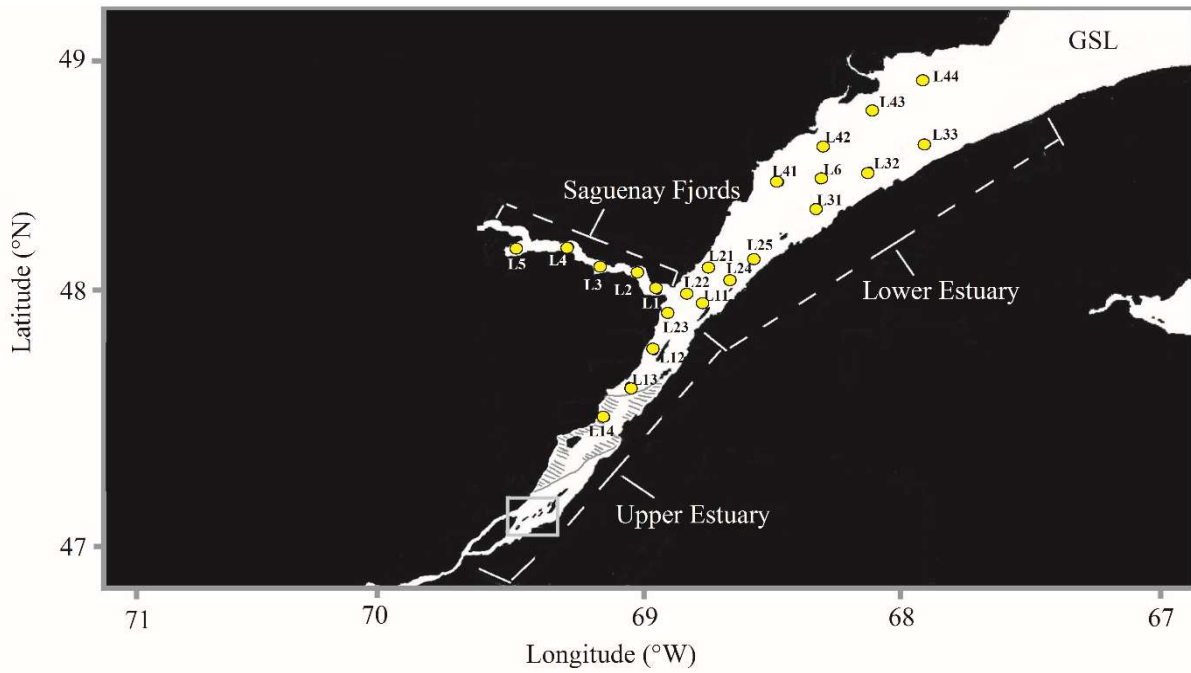
Figure A1. Sampling locations for June 2013 surveys. SLE sub-regions, Lower estuary (LE, L6 to L44), Saguenay Fjords (SF, L1 to L5), and upper estuary (UE, L12 to L14), GSL: Gulf of Saint Lawrence, Maximum turbidity zone mean boundaries (hatched area). Study area during June 2012 is highlighted with a rectangle.
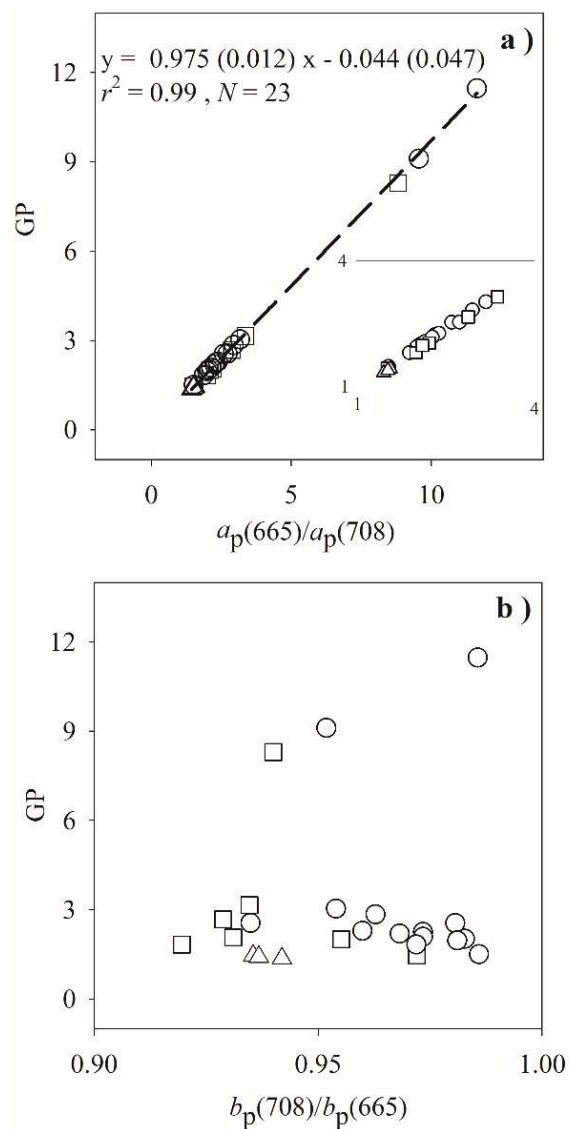
Figure A2. Response of NIR-visible optical proxy of $R_{rs}(708)/R_{rs}(665)$ to optical properties of SPM. GP = $a_p(665)$ $b_p(708)$ $(a_p(708)$ $b_p(665))^{-1}$.a) particulate absorption ratio. Datapoints in the lower range (inset), b) particulate scattering ratio. SLE sub-regions for June 2013 surveys, UE (triangles), SF (rectangles) and LE (circles), are shown in Figure A1. Linear regression equation (upper left corner), modeled GP (dash line), between parentheses are two standard errors.
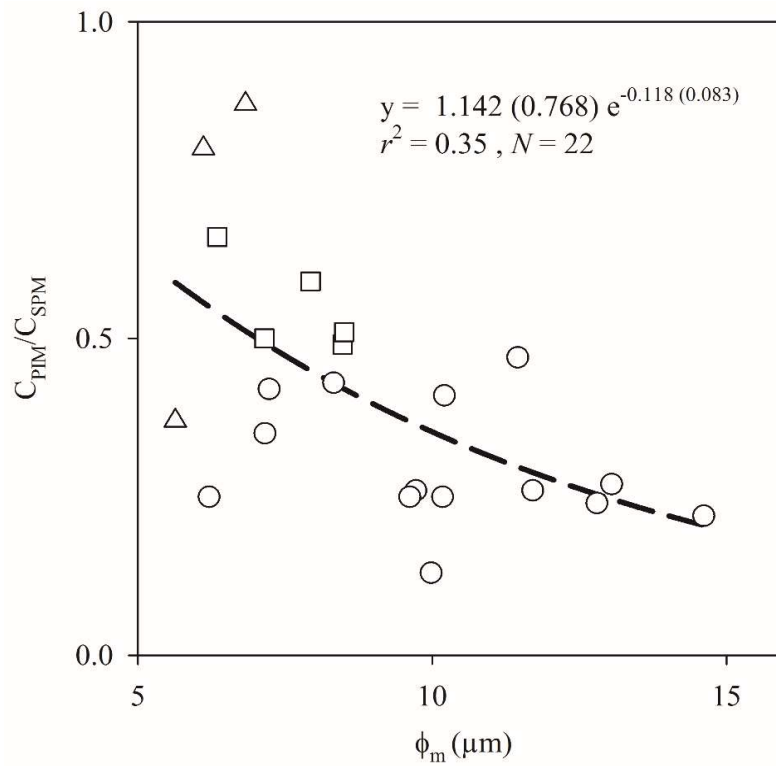
Figure A3. Exponential-type regression equation (upper right corner), modeled CPIM/CSPM (dash line), between parentheses are two standard errors.

CHAPTER 3

PROPRIETES OPTIQUES LIÉES À LA TAILLE ET AUX FRACTIONS CHIMIQUES DES MATIÈRES EN SUSPENSION DANS LES EAUX LITTORALESDU QUÉBEC

Ce deuxième article, intitulé « *Optical properties of size and chemical fractions of suspended particulate matter in littoral waters of Quebec*», fut corédigé par moi-même ainsi que par les professeurs Martin A. Montes-Hugo, Jean-Pierre Gagné et Pierre Larouche. L'article sera soumis au journal *Optic Express*. En tant que premier auteur, ma contribution à ce travail fut d'effectuer les recherches bibliographiques et de mettre à jour l'état des connaissances sur le sujet étudié, d'effectuer le développement de la méthode et l'exécution des tests de performance. Le professeur Martin A. Montes-Hugo, dernier auteur, a fourni l'idée originale. Il a aidé à la recherche sur l'état des connaissances, au développement de la méthode ainsi qu'à la révision et la rédaction de l'article. Les professeurs Jean-Pierre Gagné et Pierre Larouche ont aidé à la recherche sur l'état de l'art ainsi qu'à la révision de l'article.

Résumé

Les coefficients d'absorption massiques spécifique ($a_{SPM}*$) et de diffusion ($b_{SPM}*$) des matières particulaires en suspension ont été mesurés pour la matière en suspension de différentes tailles (0.2-0.4 µm, 0.4-0.7 µm, de 0.7 à 10 µm, et> 10 µm) et de compositions chimiques variables (dominance organique ou minérale) dans les eaux de surface du système du Saint-Laurent au cours du printemps 2013. En général, pour le spectre visible et proche de l'infrarouge, l'$a_{SPM}*$ et les sections de diffusion efficaces estimés pour les particules de matière inorganique étaient plus élevées par rapport à celles mesurées dans d'autres environnements littoraux. L'analyse des corrélations entre différents paramètres suggère que la composition des particules a un plus grand impact sur $a_{SPM}*$ que sur $b_{SPM}*$ comparé aux effets de la distribution de la taille des particules.

Optical properties of size and chemical fractions of suspended particulate matter in littoral waters of Quebec

Mohammadpour Gholamreza[1], Jean-Pierre Gagné[1], Pierre Larouche[2], Martin A. Montes-Hugo[1*]

[1]Institut des Sciences de la Mer de Rimouski, 310 Alleé des Ursulines, Office P-216, Rimouski, Québec, Canada, G5L 3A1

[2]Institut Maurice-Lamontagne, Pêches et Océans Canada, Mont-Joli, Québec, Canada, G5H 3Z4

*corresponding author: martinalejandro_montes@uqar.ca

Abstract

Mass-specific absorption (a_{SPM}^*) and scattering (b_{SPM}^*) coefficients of suspended particulate matter (SPM) were measured for different size (0.2-0.4 μm, 0.4-0.7 μm, 0.7-10 μm, and >10 μm) and chemical (organic- vs mineral-rich) fractions in surface waters (i.e., 0-5 m depth) of the Saint Lawrence Estuary and Saguenay Fjords (SLE-SF) during spring of 2013. For the spectral range 400-700 nm, scattering cross sections for particulate inorganic matter were commonly larger with respect to those measured in other littoral environments. This phenomenon was attributed the lower water turbidity of the SLE-SF with respect to other river-influenced regions (e.g., Gironde River). Also, a_{SPM}^* values in our study area were relatively not only high in locations typically rich in particulate iron but also characterized by relatively high concentrations of chromophoric dissolved organic matter. Lastly, correlation analysis suggests that particle composition (size distribution) has a larger impact on a_{SPM}^* (b_{SPM}^*). This is consistent with published remote sensing models and

highlights the importance of including scattering processes for estimating 'bulk' changes on size spectra of suspended particulates.

3.1 INTRODUCTION

The distribution of suspended particulate matter (SPM) in coastal and estuarine environments has a major influence on several ecological processes (e.g., phytoplankton blooms) and human related activities (e.g., contaminant dispersion). The concentration of SPM (C_{SPM}) is an important variable to estimate primary productivity and thermodynamic processes due to its influence on underwater light attenuation (Zhai et al. 2011; Morel and Antoine, 1994; Löptien and Meier, 2011). Likewise, size distribution and chemical composition of SPM are critical parameters for better understanding trophic relationships in a food web, the fate of pollutants, and the transport of sediments (Tremblay et al., 2005; Dunton et al. 2012, Dong et al. 2016, Yang et al. 2017).

Due to its variability, spatial variations of SPM in littoral environments are commonly investigated based on synoptic measurements derived from spaceborne ocean color sensors. This approach has proven to be successful for estimating C_{SPM} based on visible (i.e., wavelength, λ = 400-700 nm) and infrared (λ = 700-3,000 nm) spectral bands (Doxaran et al., 2002; Miller and McKnee, 2004; Montes-Hugo and Mohammadpour, 2012). Despite this progress, there is still a lack of understanding regarding how SPM microphysical characteristics (e.g., particle chemical composition and size distribution) relate to mass-specific inherent optical properties (IOPs) of particulates. This knowledge is essential for deriving more accurate algorithms used for estimating C_{SPM} and developing new mechanistic models for retrieving second-order attributes of SPM (i.e., chemical composition, size distribution).

The remote sensing of particle size and composition in coastal and oceanic waters has been attempted based on four main methodologies: (1) analysis of spectral changes of IOPs

(Loisel et al., 2006), (2) empirical relationships between mass-specific IOPs and biogeo-physical characteristics of SPM (e.g. mean diameter of particulates) (Bowers et al., 2009), (3) optical inversions of different volume scattering functions (Zhang et al. 2013; Zhang et al., 2014), and (4) changes on water leaving polarized reflectance (Loisel et al., 2008).

The Saint Lawrence Estuary (SLE) and the Saguenay Fjords (SF) constitute a large sub-Arctic system characterized by relatively high concentrations of chromophoric dissolved organic matter (CDOM) (Nieke et al., 1997). The accurate monitoring of C_{SPM} and SPM characteristics in these waters is crucial for understanding regional climate effects on coastal erosion and occurrence of harmful algae blooms (Bernatchez and Dubois, 2004; Fauchot et al. 2008).

Despite this need, there is a lack of information regarding how optical properties are linked to particle second-order attributes and what is the spatial variability of mass-specific IOPs of SPM. For this reason, our contribution has two main objectives: (1) to characterize the mass-normalized IOPs for size and chemical fractions of SPM in different locations of the SLE-SF during spring conditions, and (2) to establish relationships between mass-specific optical properties of SPM, 'bulk' particle characteristics related to size distribution and mineral content, and optical remote sensing proxies within the visible and near-infrared spectral range (i.e., $\lambda = 700\text{-}1{,}000$ nm).

This study is organized in three sections. In the first section, mass-normalized spectral absorption and scattering coefficients for size and chemical SPM fractions are calculated for different optical environments of the SLE-SF waters in terms of CDOM contribution to light attenuation and particle characteristics. In the second section, the response of mass-normalized absorption and scattering coefficients of SPM fractions to variations in particle size distribution and mineral-content are investigated. Lastly in the third section, covariations between remote sensing proxies and microphysical properties of SPM are examined.

3.2 DATA AND METHODS

3.2.1 STUDY AREA

The SLE can be divided in two main regions having contrasting biological productivity and bathymetry: the upper (UE) and the lower (LE) estuary (Levasseur et al., 1984) (**Figure S1**). Non-algal particulates (NAP) and CDOM dominate the underwater light attenuation of UE waters (Nieke et al., 1997). This is in part related to the inflow of CDOM-rich and NAP-rich waters coming from the St. Lawrence River (Tremblay, and Gagné, 2007). Unlike NAP and CDOM, contribution of phytoplankton to IOPs increases downstream and along the LE (Montes-Hugo and Mohammadpour, 2012). Historical studies performed during summer of 1975 suggest that size distribution of SPM differs between the UE, LE and SF regions (Poulet et al., 1986). Based on surface samples, Poulet et al. (1986) found a dominance of relatively 'small-sized' (i.e., mode diameter < 10 μm) and 'large-sized' (i.e., > 30 μm) particulates over the UE and the mouth of the SLE, respectively.

Conversely, the remaining locations of the LE were characterized by particulates having an intermediate size (i.e., 8-40 μm). In surface waters of SF, SPM is mainly composed by very small particles (i.e., 2-3 μm) during spring months (Chanut and Poulet, 1979). However, this pattern is reversed during autumn. Several investigations suggest that suspended particulates in SLE-SF regions are principally composed by inorganic matter (D'Anglejan, and Smith, 1973; Larouche and Boyer-Villemaire, 2010). This mineral contribution varies between 60 and 95% of dry weight depending on location and period of the year (Yeats, 1988; Larouche and Boyer-Villemaire, 2010).

3.2.2 FIELD SURVEYS

Discrete water samples for biogeochemical and optical measurements were obtained in 23 sampling locations distributed over the SLE (n =18) and SF (n = 5) regions (Fig. S1). Samples were collected by using an oceanographic rosette onboard the vessel NGCC Frederick G. Creed and during June 3-9 of 2013. In all cases, the sampling was done near the surface (i.e., 2 m depth) by using Niskin bottles (volume = 12 L). Three main types of variables were analyzed during the survey: mass of different size fractions of SPM, IOPs for different SPM size fractions, and particle size distribution spectra.

3.2.3 BIOGEOCHEMICAL ANALYSIS

The concentration of SPM and particulate inorganic matter (C_{PIM}) in g m^{-3} was measured gravimetrically with a precision of 15% and 25%, respectively (Mohammadpour et al., 2015). Size fractionation of SPM was done after sequentially filtering the original samples through pre-weighted membranes having a diameter of 47 mm and a pore size of 10 µm (Whatman, polycarbonate), 0.7 µm (GF/F, Whatman, glass fiber), 0.4 µm (Whatman, polycarbonate), and 0.2 µm (Nucleopore, polycarbonate). The contribution of size fraction i to the total mass of SPM (F_{SPM}^i, i = 0.2-0.4 µm, 0.4-0.7 µm, 0.7-10 µm, and >10 µm) was computed by normalizing their weight by the total weight of unfractioned samples that were retained on 0.2 µm membranes. The contribution of particulate inorganic (PIM) and organic (POM) to mass is F_{SPM}^j where j superscript symbolizes PIM or POM ($F_{SPM}^{PIM} = C_{PIM}/C_{SPM}$, $F_{SPM}^{POM} = C_{POM}/C_{SPM}$).

3.2.4 OPTICAL MEASUREMENTS

Discrete water samples for CDOM absorption coefficient (a_{CDOM}) determinations were done in the lab following protocols suggested by Muller and Horn (1990). Total absorption (a) and beam attenuation (c) coefficient measurements for four size fractions (0.2 – 0.4 μm, 0.4 – 0.7 μm, 0.7 – 10 μm, and > 10 μm) were performed onboard using an absorption-beam attenuation meter (ac-s, WetLabs) after each filtration of water samples. Spectral values of b were computed by subtracting a from c at each wavelength, using the baseline correction at 715 nm (Röttgers et al. 2013). The particle size spectra of discrete water samples and within the size range 3-170 μm were measured before filtering and by using a red laser (wavelength = 670 nm) diffractometer (LISST-100X, type B, Sequoia Scientifics) (Agrawal et al. 1991).

3.2.5 OPTICAL PROXIES OF PARTICLE CHARACTERISTICS

Optical composite parameters directly related to remote sensing reflectance (R_{rs}) (Table acronyms) were constructed based on IOPs since no in situ Rrs measurements were available in the oceanographic surveys conducted during 2013. Values of a and b at different wavelengths can be linked to the reflectance or irradiance ratio measured just below the water surface ($R(0^-)$) (Morel and Prieur, 1977):

$$R(0^-) = f \ b \ b_b^{eff} / a \tag{1}$$

$$R_{rs} = R(0^-) \ \kappa/Q_n(\theta_0) \tag{2}$$

where f is a coefficient that varies with atmospheric (e.g., solar zenith angle) and water (e.g., single scattering albedo) parameters (Morel and Gentilli, 1996), b_b^{eff} is the backscattering efficiency for water plus particulates (i.e., b_b/b where b_b is the backscattering coefficient). The magnitude of κ depends on refraction and internal reflection of photons at the air-water interface. For a nadir-looking sensor, the $Q_n(\theta_0)$ is defined as the ratio between upwelling irradiance and upwelling radiance just beneath the sea surface and as a function of the solar

zenith angle (θ_0). From equations (1) and (2), three biogeo-optical indices (BOI) were proposed for estimating changes in 'bulk' chemical composition (superscript comp) and size distribution (superscript size1 and size2) of SPM:

$$BOI^{comp} = a_{SPM}(\lambda_6)/a_{SPM}(\lambda_4) \tag{3}$$

$$BOI^{size1} = F((b(\lambda_1)\,a(\lambda_2))\,(a(\lambda_1)\,b(\lambda_2))^{-1}) \tag{4}$$

$$BOI^{size2} = F((b(\lambda_5)\,a(\lambda_3))\,(a(\lambda_5)\,b(\lambda_3))^{-1}) \tag{5}$$

where a_{SPM} is the absorption coefficient of SPM, F is the polynomial function $g + g^2$, where $g = b(\lambda)\,(b(\lambda)+ a(\lambda))^{-1}$, and λ_1, λ_2, λ_3, λ_4, λ_5 and λ_6 correspond to centered wavelengths 443, 488, 555, 570, 670 and 675 nm, respectively. Values of the particulate absorption coefficient (a_{SPM}) were derived by subtracting the contributions of CDOM and sea water to a. The absorption coefficient (a_w) and scattering (b_w) coefficient of seawater were computed at in situ salinity and temperature by using empirical parameterizations suggested by Pope and Fry (1997) and Zhang et al. (2009), respectively.

The equation (3) was suggested based on empirical relationships between $a_{SPM}(\lambda_6)/a_{SPM}(\lambda_4)$ and POC/C_{SPM} ratios, where POC is the particulate organic carbon concentration (Wozniak et al., 2010). BOI indices for particle size distribution were based on published R_{rs} band ratios used for estimating the spectral slope of particulate backscattering (Carder et al., 2004; D'Sa et al., 2007). In general, BOI^{comp} values are expected to increase as SPM becomes richer in POC. Likewise, BOI^{size1} and BOI^{size2} are anticipated to decrease as particulates become larger or water contribution to backscattering increases at relatively low water turbidities.

3.2.6 OPTICAL CROSS SECTIONS AND MASS-NORMALIZED IOPS

Spectral values of mass-specific absorption (σ_d^j) and scattering (σ_b^j) cross sections for mineral and organic fractions of SPM were estimated from multiple regression analysis (Sokal et al., 1995). The superscript j indicates inorganic (PIM) u organic (POM) particulate

matter. For the case of size fractions of SPM, a mass-normalized variable was calculated for particulate absorption and scattering coefficients:

$$a_i{}^*(\lambda) = a_x(\lambda)(m_x)^{-1} \tag{6}$$

$$b_i{}^*(\lambda) = b_x(\lambda)(m_x)^{-1} \tag{7}$$

where m is the mass in g m^{-3} for each size class i.

3.2.7 STATISTICAL ANALYSIS

The influence of particle size and chemical composition variations on a_{SPM}, b_{SPM}, σ_a, σ_b, a^*, and b^* was investigated using the non-parametric Spearman rank correlation coefficient (ρ_S) (Spearman, 1904). This metrics was also applied to examine the sensitivity of $a_x{}^*$ and $b_x{}^*$ values to variations of the differential Junge slope (γ) or the slope of log-transformed number of particulates per unit of volume as a function of their size range (Junge, 1963). Values of γ were computed based on linear regression models where dependent and independent variables are randomly selected (i.e., type II parameterization). Although particle size distribution in natural waters may not follow a Junge-type slope, its use here was justified since our main interest was to have a first-order assessment of size effects of particulates on IOPs. The sensitivity of BOI$^{\text{comp}}$, BOI$^{\text{size1}}$, and BOI$^{\text{size2}}$ to variations of different chemical and SPM size fractions was quantified based on the magnitude of ρ_S. Lastly, potential functionalities between mass-normalized IOPs for different study regions were examined based on linear regression analysis model type II.

3.3 RESULTS

3.3.1 SPATIAL VARIABILITY OF SPM FRACTIONS

In terms of particle size distribution, contrasting areas in the SLE-SF were identified. In UE, particulates having a diameter larger than 10 µm had on average contribution of 11% to the total SPM (**Table 1**). This proportion was lower in the LE (up to 9%) and SF (up to 6%) sub regions. The largest mass contribution of smallest-sized particulates (i.e., diameter < 0.4 µm) was calculated in the lower estuary. Lastly, the intermediate size class 0.7-10 microns was the fraction having the maximum contribution to SPM in the SF (76.5% in average).

Table 1. Summary of biogeochemical variables during June 2013. Acronyms UE, SF, LE, F_{SPM} and F_{SPM}^{PIM} are defined in the Table of acronyms. N is the number of sampling per sub-regions.

Sub-region	Fraction	Range	N
UE	F_{SPM}^{PIM}	0.37 – 0.87	3
	$F_{SPM}^{0.2-0.4\ \mu m}$	0.04-0.08	3
	$F_{SPM}^{0.4-0.7\ \mu m}$	0.01-0.04	3
	$F_{SPM}^{0.7-10\ \mu m}$	0.77-0.89	3
	$F_{SPM}^{>10\ \mu m}$	0.05-0.17	3
SF	F_{SPM}^{PIM}	0.49 – 0.66	5
	$F_{SPM}^{0.2-0.4\ \mu m}$	0.05-0.11	5
	$F_{SPM}^{0.4-0.7\ \mu m}$	0.01-0.14	5
	$F_{SPM}^{0.7-10\ \mu m}$	0.66-0.87	5
	$F_{SPM}^{>10\ \mu m}$	0.01-0.11	5
LE	F_{SPM}^{PIM}	0.53 – 0.87	15
	$F_{SPM}^{0.2-0.4\ \mu m}$	0.02-0.27	15
	$F_{SPM}^{0.4-0.7\ \mu m}$	0.01-0.10	15
	$F_{SPM}^{0.7-10\ \mu m}$	0.48-0.93	15
	$F_{SPM}^{>10\ \mu m}$	0.03-0.15	15

In general, the Junge slope calculations suggested the presence of relatively larger particulates in the LE with respect to UE and SF sub-regions. Indeed, the arithmetic average and range of γ for LE, UE and SF locations were 1.67 and 0.9-2.4, 2.4 and 2.3-2.4, and 2.4 and 2.1-2.6, respectively. The uncertainty of γ calculations varied between 8 and 90% based on the coefficients of determination, with smaller errors in the LE. Unlike particle size distribution modification, chemical composition of SPM was less variable (20 to 87 %). In average for each sub-region under investigation, the mass of suspended particulates was always determined by inorganic matter by inorganic matter (F_{SPM}^{PIM} = 0.58, 0.62 and 0.70 for SF, UE and LE, respectively, **Table 1**). The largest variability of mineral content of SPM was the characteristic of waters with relatively shallow depths and a greater of freshwater discharge by the St Lawrence River (e.g., sampling locations 12 and 13 in the UE).

3.3.2 RELATIONSHIPS BETWEEN SPM FRACTIONS AND IOPs

In general, size spectra and mineral content of SPM were important second-order attributes affecting the scattering coefficient of suspended particulates. In general, b_{SPM} response to changes on SPM size fractions and chemical composition (ρ_s up to 0.71 and 0.59, t up to 21.17 and 15.35, Student-t test, respectively) was greater with respect to that associated to a_{SPM} (ρ_s up to 0.53 and 0.21, t up to 13.13 and 4.51, Student-t test, respectively) (**Table 2**).

The larger influence of particle size distribution on b_{SPM} compared to a_{SPM} values was supported by correlations between γ and IOPs (ρ_s up to 0.50, t up to 12.12, Student-t test; ρ_s up to 0.33, t up to 7.34, Student-t test) (**Table S1**).

Unlike particle size, the impact of SPM chemical composition on a_{SPM} was principally manifested at relatively short wavelengths (i.e., λ = 440-556 nm, ρ_s up to 0.21, t up to 4.51, Student-t test, **Table 2**). Indeed, the highest correlations between SPM size fractions and a_{SPM}

values were computed in the red-NIR spectral regions (e.g., ρ_s up to 0.41, t up to 9.44, Student-t test).

3.3.3 MASS-SPECIFIC OPTICAL PROPERTIES OF SPM

The variation of mass-normalized scattering and absorption coefficients of SPM for different size and chemical fractions are shown in **Figure 1**. In general, sub-regional averages of mass-normalized IOPs for different particle size ranges were higher with respect to optical cross sections of chemical fractions (up to 2 and 3 orders of magnitude for a and b, respectively). For a wavelength of 556 nm and over the whole study area, the range of values for $a_{0.2\text{-}0.4\ \mu m}^{*}$, $a_{>10\ \mu m}^{*}$, σ_a^{PIM} and σ_a^{POM} was 0.11-2.14, 0.18-1.20, 0.01-1.06 and 0.01-1.03 m^2 g^{-1}, respectively (**Figure 1a**). Likewise, for the same wavelength, the range of $b_{0.2\text{-}0.4\ \mu m}^{*}$, $b_{>10\ \mu m}^{*}$, σ_a^{PIM} and σ_a^{POM} was 1.82-2.39, 1.05-1.49, 0.03-1.06 and 0.03-0.36 m^2 g^{-1}, respectively (**Figure 1b**).

Table 2. Spearman Rank correlations between particulate IOPs and SPM mass fractions. The statistical confidence level at 95 and 99% is symbolized with * and **, respectively.

	λ	a_{SPM}	b_{SPM}
F_{SPM}^{PIM}	440	0.21 **	0.59**
	556	0.12 *	0.58**
	665	0.02	0.56 **
	708	0.17 *	0.55 **
$F_{SPM}^{0.2-0.4\ \mu m}$	440	-0.01	0.66 **
	556	0.03	0.71 **
	665	-0.03	0.70 **
	708	-0.13 *	0.66 **
$F_{SPM}^{0.4-0.7\ \mu m}$	440	-0.06	0.28 **
	556	-0.05	0.35 **
	665	-0.09	0.31 **
	708	-0.20 **	0.27 **
$F_{SPM}^{0.7-10\ \mu m}$	440	-0.12 *	-0.65 **
	556	-0.14 *	-0.67 **
	665	-0.17 *	-0.63**
	708	-0.03	-0.57 **
$F_{SPM}^{>10\ \mu m}$	440	0.36 **	0.47 **
	556	0.35 *	0.39 **
	665	0.53 **	0.33 **
	708	0.41 **	0.28 **
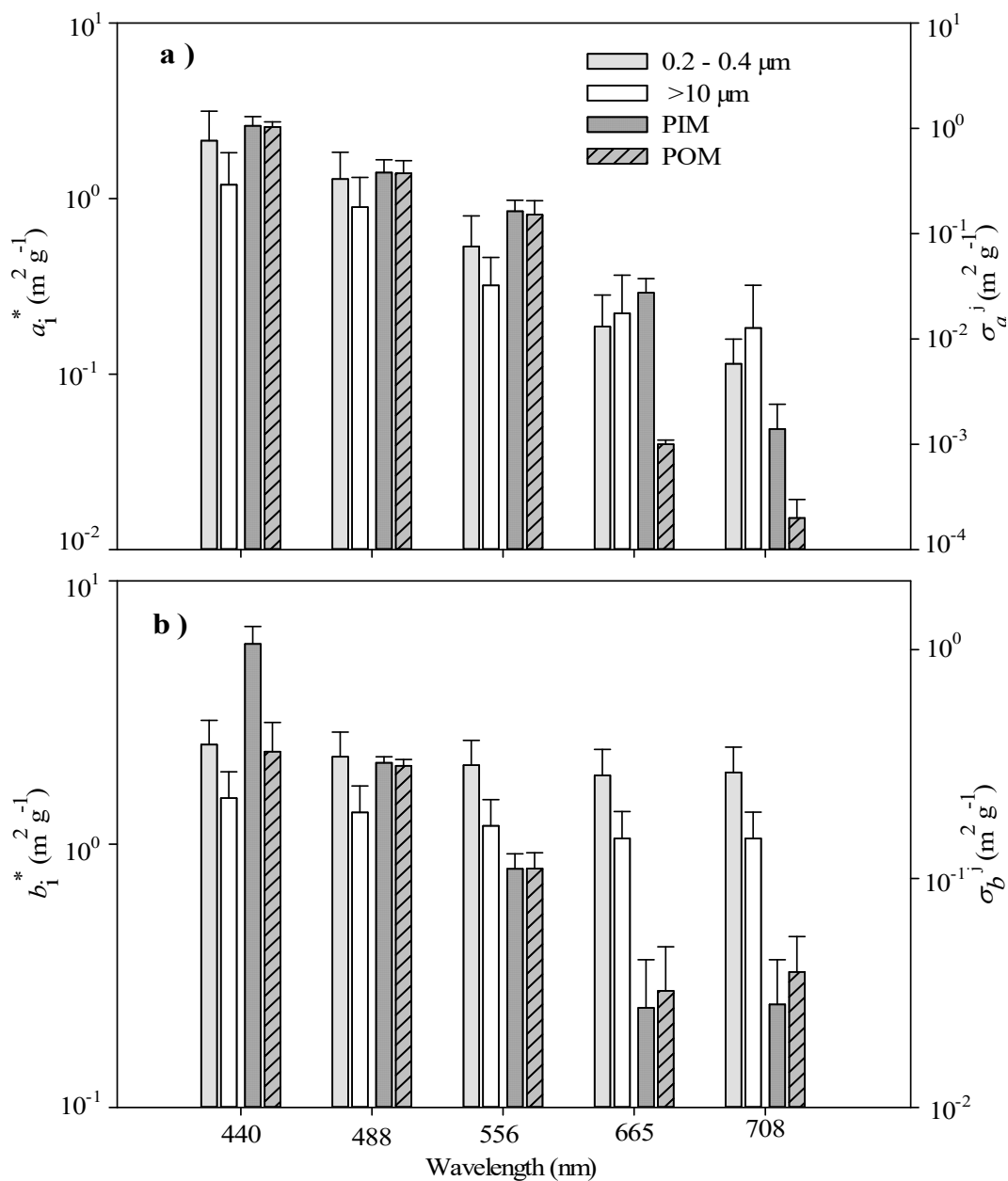
Figure 1. Spectral variations of mass-normalized optical coefficients for SPM size and chemical fractions. a) particulate absorption, b) particulate scattering. Each bar corresponds to the arithmetic average over the whole study area; uncertainty bars symbolize 2 standard errors. Subscript x and superscript j symbolize size and chemical fractions, respectively.

For the spectral range 440-556 nm, mass-normalized absorption coefficients of SPM tended to be higher for particulates within the lower size range (i.e., 0.2-0.4 μm) (**Figure 1a**, left-axis). Also, this trend appeared to be reversed at longer wavelengths. Unlike mass-normalized absorption coefficients of size fractions, mass-specific cross sections of chemical fractions showed only differences within the red and near-IR wavelengths (**Figure 1a**, right-axis). For the whole study area, the arithmetic average of mass-normalized scattering coefficients for the size fraction 0.2-0.4 μm were larger with respect to those derived for the size fraction >10 μm (**Figure 1b**, left-axis). At a wavelength of 440 nm, the mass-specific scattering cross sections for PIM were only substantially higher (1.060 ± 0.206 m^2 g^{-1}) than those corresponding to POM (0.359 ± 0.123 m^2 g^{-1}) (**Figure 1b**, right-axis).

In general, the magnitude of the mass-normalized absorption coefficient at 440 nm and computed for different size and chemical fractions was higher in UE-SF with respect to LE locations (**Figure 2a**). Notice that absorption or scattering cross sections for chemical SPM fractions are not shown in UE locations since there number of samples to perform a multiple regression analysis was insufficient. The maximum a_{SPM}^*(440) values (up to 4.6 m^2 g^{-1}) were associated with the largest size fraction of SPM and samples obtained in Saguenay Fjord waters. Unlike size fractions, no substantial sub-regional differences were detected for σ_a^{PIM}(440) and σ_a^{POM}(440) values ($P > 0.05$, t up to 0.42, Student-t test). In general, γ and F$_{SPM}^{PIM}$ correlations with mass-normalized IOPs suggest that particle chemical composition has a larger influence on a_i(440)* (ρ_s up to 0.50, t up to 12.12, Student-t test) with respect to particle size (ρ_s up to 0.31, t up to 6.85, Student-t test) (**Table 3**).

Unlike a_j(440)*, mass-specific scattering coefficients computed at 550 nm and for different size and chemical fractions of SPM presented smaller variations among spatial domains (**Figure 2b**). Only for the intermediate size fraction 0.7-10 μm, the regional average of b_i(550)* in UE-SF (0.432-0.501 m^2 g^{-1}) was larger with respect to that computed in LE waters (0.136 ± 0.027 m^2 g^{-1}). Unlike a_i(440)*, b_i(550)* variability was less influenced by changes on particle composition (ρ_s up to 0.42, t up to 9.72, Student-t test) (**Table 3**). Conversely, the impact of changing particle dimensions, as inferred from γ correlations, was

greater for $b_i(550)^*$ (ρ_s up to 0.37, t up to 8.36 Student-t test) with respect to $a_i(440)^*$ (ρ_s up to 0.33, t up to 7.34 Student-t test) values.

Table 3. Particle size and chemical composition effects on mass-normalized IOPs. Spearman correlations for a_i^* and b_i^* are computed at a wavelength of 440 and 550 nm, respectively. Acronyms γ and F_{SPM}^{PIM} are defined in the table of acronyms. The statistical confidence level at 95 and 99% is symbolized with * and **, respectively.

	γ	F_{SPM}^{PIM}
$a_{0.2-0.4\ \mu m}^*$	0.32 **	0.31 **
$a_{0.4-0.7\ \mu m}^*$	0.28 **	0.50 **
$a_{0.7-10\ \mu m}^*$	0.26 **	0.49 **
$a_{>10\ \mu m}^*$	0.31 **	0.44 **
$b_{0.2-0.4\ \mu m}^*$	0.15 *	-0.17 *
$b_{0.4-0.7\ \mu m}^*$	0.05	-0.06
$b_{0.7-10\ \mu m}^*$	0.23 **	0.42 **
$b_{>10\ \mu m}^*$	0.37 **	0.26 **
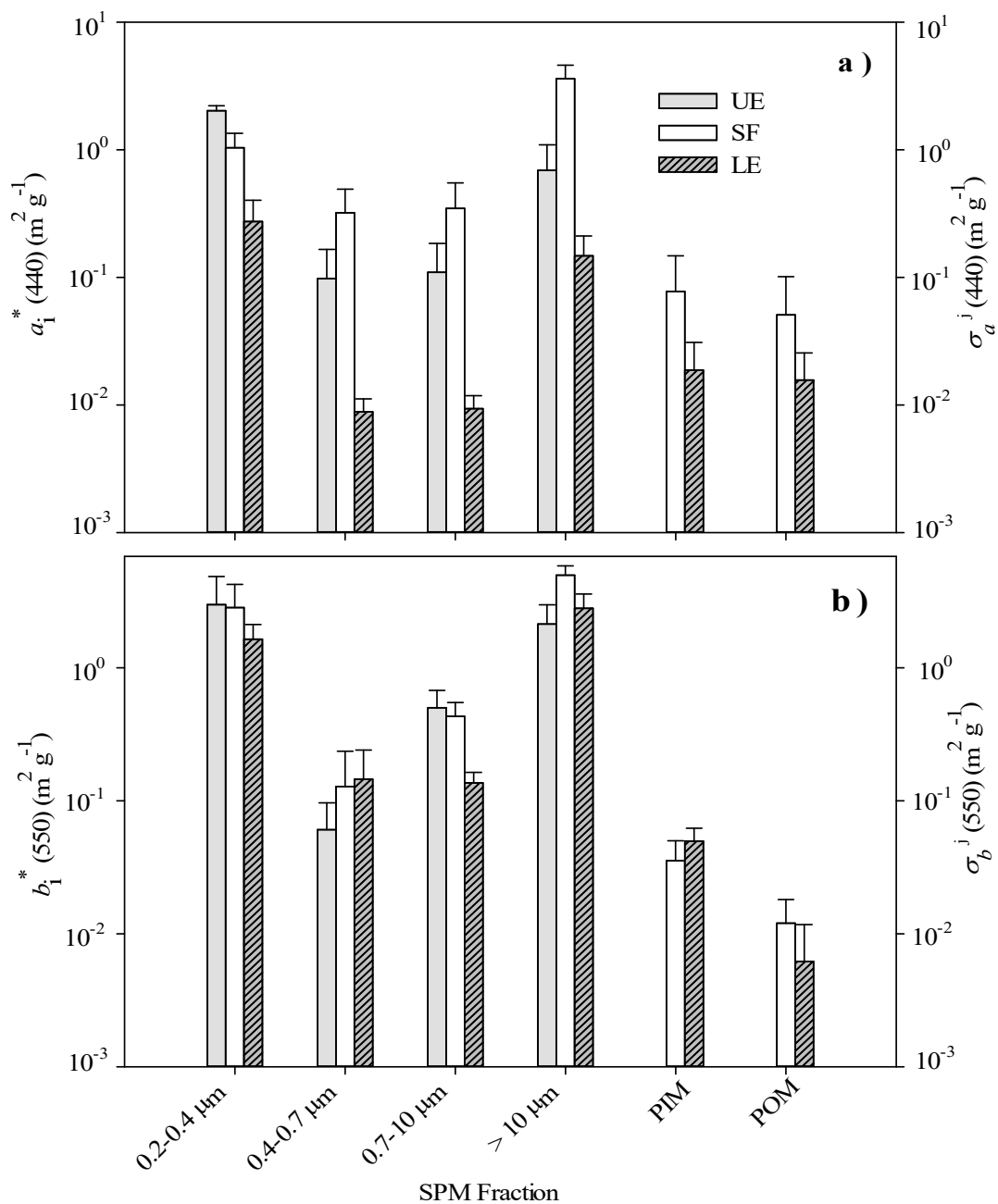
Figure 2. Sub-regional variations of mass-normalized optical coefficients of SPM. a) particulate scattering at $\lambda = 440$ nm, b) particulate absorption at $\lambda = 550$ nm. Each bar and uncertainty corresponds to the arithmetic average ± 2 standard errors of each sub-region (UE, SF and LE are defined in Table of acronyms. Subscript i and superscript j as in Figure 1.

3.3.4 OPTICAL REMOTE SENSING PROXIES

Correlations between individual samples of size-based fractions of SPM and ratios of IOPs related to remote sensing proxies for estimating particle size and chemical composition are presented in **Table 4**. In general, it was found that BOI^{size1} was a more selective biogeo-optical indicator for retrieving second-order properties of SPM than BOI^{size2} and BOI^{comp}. Indeed, BOI^{size2} was also dependent on particle chemical composition variations as inferred from F_{SPM}^{PIM} (ρ_S = -0.16, P <0.05, t = -3.40, Student-*t* test). Likewise, BOI^{comp} changes were also connected to variations of $F_{SPM}^{0.2\text{-}0.4\ \mu m}$ (ρ_S = 0.34, t = 7.59, Student-*t* test) and $F_{SPM}^{>10\ \mu m}$ (ρ_S = -0.26, t = 5.65, Student-*t* test) fractions. Despite these dependencies, BOI^{comp} had the strongest correlations with F_{SPM}^{PIM} values (ρ_S = 0.38, P < 0.05, t = 8.63, Student-*t* test).

Optical proxies for estimating particle size had a different performance depending on the size fraction. Indeed, Carder et al. (2004) and D'Sa et al. (2007) indices were preferentially associated to changes of relatively small-sized (i.e., $F_{SPM}^{0.2\text{-}0.4\ \mu m}$, ρ_S up to -0.29, t up to -6.36, Student-*t* test) and intermediate-sized ($F_{SPM}^{0.4\text{-}0.7\ \mu m}$, ρ_S up to 0.35, t up to 7.85, Student-*t* test) particulates, respectively (**Table 4**).

Unlike BOI^{comp}, BOI^{size1} and BOI^{size2} indices had a greater correlation with mass-specific IOPs and this dependency was stronger for larger particulates and mass-normalized absorption coefficients (ρ_S up to 0.74, t up 23.10 Student-*t* test). Notice that no correlations between $\sigma_a^{j,\ SPM}$, $\sigma_b^{j,\ SPM}$, BOI^{size1}, BOI^{size2} and BOI^{comp} are shown because only 3 optical cross sections of SPM chemical fractions were computed over the whole study area .

Table 4. Particle size and chemical composition effects on optical remote sensing proxies. Spearman rank correlations having a statistical confidence level at 95 and 99% are symbolized with * and **, respectively. N the number of observations is 23.

	BOI ^{size1}	BOI ^{size2}	BOI ^{comp}
F_{SPM}^{PIM}	-0.02	-0.16 *	0.38 **
$F_{SPM}^{0.2-0.4 \ \mu m}$	-0.29 **	0.03	0.34 **
$F_{SPM}^{0.4-0.7 \ \mu m}$	-0.28**	0.35**	-0.20**
$F_{SPM}^{0.7-10 \ \mu m}$	0.27**	-0.12*	-0.21*
$F_{SPM}^{>10 \ \mu m}$	-0.01	-0.10	0.26*

3.4 DISCUSSION

3.4.1 SPATIAL PATTERNS OF SPM MICROPHYSICAL CHARACTERISTICS

A striking finding in this study was the important weight contribution of relatively large particulates (i.e., >10 µm) in UE waters with respect to the other sub-regions. This phenomenon was likely attributed to the active resuspension of sediments associated with a continuous vertical mixing produced by tidal currents and winds (Yeats, 1988). Conversely, this effect was secondary in relatively deep waters of SF and LE where large and heavy particulates are rapidly removed from the water column and deposited along submarine canyons (Gagné et al., 2009).

Although chemical composition of SPM size fractions was not analyzed in this study, additional correlations between total F_{SPM}^{PIM} and SPM size fractions values suggest that smallest particulates were richer in inorganic matter ($\rho_s = 0.27$, t up to 5.89, Student-*t* test, Table S3). Also, the opposite was true for the largest particulates ($\rho_s = -0.27$, t up to -5.89, Student-*t* test). This finding confirms previous studies showing that relatively small (~2 µm) particulates in the SLE are mainly composed by minerals (Yeats, 1988; Gagné et al., 2009).

In this contribution, a large proportion of particulates with a diameter above 50 µm and lower γ values were typically found in LE locations. This regional variation in SPM size distribution was attributed to the major influence of large-sized particulates derived from phytoplankton as γ was strongly correlated with chlorophyll a concentration ($\rho_s = -0.45$, t up to -10.58, Student-*t* test, **Table S4**). These results also support historical observations made during July and August and showing a greater proportion of relatively large particulates (i.e., > 5 and < 50 µm) over the LE locations (Chanut and Poulet, 1979).

3.4.2 SPATIAL VARIABILITY OF MASS-SPECIFIC COEFFICIENTS OF SPM

In this study, a_{SPM}* measurements in the visible and near-IR range were in the upper range or higher than those reported in the literature for temperate coastal waters (e.g., Mobile Bay, River of La Plata, Elbe Estuary, Gironde Estuary) (Stavn and Richter, 2008; Doxaran et al., 2009; Dogliotti et al., 2015) (**Table 5**). In general, lowest a_{SPM}* values commonly corresponded with samples obtained in very turbid environments (i.e., > 100 g m^{-3}, Gironde River, La Plata River) (Dogliotti et al., 2015; Doxaran et al., 2009). Also, highest a_{SPM}* values in the SLE were not associated to UE locations where water turbidity was maximum. Lastly, σ_a^{POM} and σ_a^{PIM} estimates in this study were generally lower and higher respectively compared with those reported in littoral waters having a concentration of SPM up to 6 and 50 g m^{-3}, respectively (Bowers and Binding, 2006; Snyder et al., 2008).

Table 5. Mass-normalized absorption and scattering coefficients of SPM, PIM and POM in the SLE and different littoral environments. Acronyms λ, a_{SPM}^*, b_{SPM}^*, σ_a^{POM}, σ_a^{PIM}, σ_b^{POM}, σ_b^{PIM} and C_{SPM} are defined in Table 1.

Location	λ	a_{SPM}^*	b_{SPM}^*	σ_a^{POM}	σ_a^{PIM}	σ_b^{POM}	σ_b^{PIM}	C_{SPM}	Reference
	440	0.01 – 2.68	0.01 – 2.71	0.15	0.11	0.84	2.27	7.38 – 30.6	This study
UE	488	0.01 – 0.99	0.01 – 2.70	0.06	0.05	0.76	2.04		
	556	0.01 – 0.32	0.01 – 2.55	0.01	0.01	0.71	1.82		
	665	0.01 – 0.15	0.01 – 1.75	0.01	0.05	0.45	1.67		
	708	0.01 – 0.12	0.01 – 0.79	0.01	0.02	0.11	1.31		
SF	440	0.01 – 2.61	0.03 – 2.39	1.71	0.86	1.78	0.94	2.28 – 3.68	
	488	0.01 – 1.76	0.05 – 1.76	1.84	0.43	1.14	0.88		
	556	0.01 – 1.55	0.05 – 1.68	0.85	0.17	0.45	0.56		
	665	0.01 – 0.70	0.01 – 0.68	0.12	0.11	0.23	0.12		
	708	0.01 – 0.44	0.01 – 0.49	0.01	0.01	0.12	0.04		

LE	440	0.01 – 1.95	0.01 – 2.17	0.07	0.02	2.64	2.04	2.72 – 25.7
	488	0.01 – 1.24	0.01 – 2.06	0.03	0.01	2.13	1.88	
	556	0.01 – 1.18	0.01 – 1.38	0.01	0.01	1.88	1.36	
	665	0.01 – 1.04	0.01 – 1.03	0.02	0.01	1.42	0.89	
	708	0.01 – 0.88	0.01 – 0.88	0.02	0.01	0.98	0.67	
Elber River,	650	0.001 – 0.020					0.5-10	(Rottgers et al., 2014)
German Bight,	750	0.001 – 0.019						
Baltic Sea, New Caledonia lagoon	850	0.001 – 0.014						

Location	nm						Reference
Monterey Bay, US	532		0.46 – 2.54	1.23–3.39	0.08 – 0.77	0.11 – 2.37	(Zhang, 2014)
Mobile Bay, US	532		0.40 – 1.78	0.35–3.85	0.27 – 0.79	0.26 – 7.36	
Hudson Bay, Canada	675	0.001 – 0.12				0.2 – 2.5	(Xi et al., 2013)
Mississippi River, US	450	0.02 – 0.11				7-25	(Bowers and Binding, 2006)
	550	0.017 – 0.06					
	650	0.012 – 0.035					
	700	0.01 – 0.025					

Mobile Bay,	440	0.44 – 1.95			0.01-1.91	0.36 – 0.80	0.23-25.32	(Stavn and Richter, 2008)
Southwest Pass, US	488	0.41 – 1.89			0.01-1.82	0.36-0.73		
	550	0.40 – 1.80			0.01-1.65	0.33-0.70		
	676	0.36 – 1.63			0.04-1.48	0.34-0.63		
	715	0.34 – 1.61			0.02-1.39	0.33-0.58		
Coast of New Jersey,	440		0.23 –0.59	0.08–0.17	0.7 – 5.1	0.3 – 1.3	0.44 – 6.6	(Snyder et al., 2008)
Monterey Bay,	488		0.18 – 0.39	0.07–0.13	0.65 – 4.8	0.4 – 1.6		
Great Bay	556		0.13 – 0.21	0.05–0.08	0.4 – 4.3	0.5 – 1.8		

Location	λ							Reference
	665		0.09 – 0.11	0.05–0.06	0.35 – 3.8	0.4 – 1.7		
	708		0.02 – 0.03	0.01–0.02	0.4-3.9	0.3-1.7		
Irish sea, UK	665	0.08 – 0.45		0.01 – 0.02		0.47 – 0.49	1.9 – 26.5	(Binding et al., 2005)
Irish sea, UK	443	0.17 – 0.19		0.05 – 0.06		0.25 – 0.27	1.6 – 50	(Bowers and Binding, 2006)
	490	0.20 – 0.22		0.03 – 0.04		0.33 – 0.37		
	555	0.20 – 0.24		0.03 – 0.03		0.37 – 0.39		
	665	0.14 – 0.15		0.02 – 0.03		0.27 – 0.29		

Location	Wavelength	Range 1	Range 2	Range 3	Reference
English channel, UK	550	0.62 – 1.04		0.01 – 72.8	(Babin et al., 2003)
Coast off Europe and French Guyana	676	0.63 – 2.07	0.12 – 1.83	1.2 – 82.4	(Neukermans et al., 2012)
Guyana coast, Scheldt River, Gironde River, Rio de la Plata Estuary	440	0.02 – 0.12	0.37 – 0.89	30 – 120	(Dogliotti et al., 2015)

Elbe Estuary, Germany	555	0.05 – 0.07	0.35 – 0.47	73.5 – 294.2	(Doxaran et al., 2009)
	715	0.01 – 0.03	0.32 – 0.44		
Gironde Estuary, France	555	0.02 – 0.06	0.28 – 0.50	21.9 – 344.1	
	715	0.01 – 0.02	0.27 – 0.45		

One mechanism explaining the general decrease of $a_{SPM}*$ in very turbid waters is related to packaging effects (Zhang 2014). At higher turbidities, particulates become dominated by larger size distributions, thus as mean diameter of particles increases, the scattering efficiency of SPM decreases. In SF waters, the magnitude of $a_{>10\mu m}(440)*$ values were higher with respect to those computed in other SLE subregions. These differences could be related to the relatively high concentrations of particulate iron and humic substances in surface waters of the Saguenay Fjord (Yeats and Bewers, 1976; Tremblay and Gagné, 2009). Pigmentation of mineral particulate due to iron hydroxides have been suggested to be a major factor enhancing $a_{SPM}*$ (Babin and Stramski, 2004; Estapa et al., 2012). Likewise, the association between iron and humic substances have been shown to increase absorption coefficient of CDOM by several folds in the visible range of the spectrum (Xiao et al., 2013) and could contribute in the increase in the magnitude of $a_{SPM}*$ in the SF.

Unlike $a_{SPM}*$, the magnitude of $b_{SPM}*$ during our surveys was comparable, smaller or higher with respect to other studies depending on the wavelength and the type of environment. To exemplify, at the wavelength of 440 nm, the magnitude of our $b_{SPM}*$ measurements was comparable to that reported in coastal waters off Mississippi (Stavn and Richter, 2008). However, these values were higher compared to that reported in the Irish Sea waters (Bowers and Binding, 2006). The magnitude of σ_b^{POM} was relatively low with respect to values measured in environments having lower turbidities with respect to the SLE (e.g., Monterrey Bay, Mobile Bay and off New Jersey shore) (Snyder et al., 2008; Zhang, 2014). Lastly, our σ_b^{PIM} estimates were relatively high with respect to those characteristics of environments having a greater concentration of SPM (e.g., La Plata River, Irish Sea) (Bowers and Binding, 2006; Dogliotti et al., 2015). This trend with turbidity was supported in our study area as sub-regional averages of σ_b^{PIM} showed higher values downstream where C_{SPM} was up to 10-fold lower with respect to the upper estuary. In general, as waters become richer in suspended particulate matter, the mean diameter of particles increases. This change is

expected to lower the scattering efficiency of particulates as deduced from Mie theory calculations (Peng and Effler, 2012). Thus, lower b_{SPM}* values should be typically associated with waters dominated by relatively high C_{SPM} values.

3.4.3 PARTICLE SIZE AND COMPOSITION EFFECTS ON OPTICAL CROSS SECTIONS

Correlations of γ and F_{SPM}^{PIM} with mass-normalized IOPs for different SPM size fractions showed two contrasting optical responses. First, γ was positively correlated with $a_{SPM}(440)$* (ρ_s up to 0.33, t up to 7.34, Student-t test) and $b_{SPM}(550)$* (ρ_s up to 0.56, t up to 14.19, Student-t test) for particulates larger than 10 μm. This pattern was due probably to the greater changes in particle density as particulates get bigger and more hydrated (Boss et al., 2001; Neukermans et al., 2012, 2016; Reynolds et al., 2016). Wozniak and Dera (2007) found that mass-specific absorption decreases as particle size increases. Based on theoretical calculations, Babin et al. (2003) showed a positive relationship between $b_{SPM}(550)$* and the Junge slope of particle size distribution. Also in this study, $b_{SPM}(550)$* was found to be directly related to γ (**Table 3**).

F_{SPM}^{PIM} had a stronger correlation with $a_{SPM}(440)$* compared with $b_{SPM}(550)$* values, and these relationships were stronger when SPM was dominated by particulates with an intermediate size (i.e., 0.4-10 μm). Babin et al. (2004) obtained positive correlations between a_{SPM}* and iron content of minerals. Rottgers et al (2014) suggest that low a_{SPM}* values (averagely 0.001-0.01 m^2g^{-1}) in the near-IR are characteristic of organic detritus (i.e., non-algal particulate organic matter). In summary, particle size (chemical composition) appears to be more important than particle composition (particle size) for influencing spatial variability of b_{SPM}* (a_{SPM}*) in Saint Lawrence Estuary waters, which is similar to the findings of Reynolds et al. (2016) in terms of particle backscattering at 550 nm in the Arctic waters. These functionalities seem to be different to those established across coastal-oceanic

gradients by Babin et al. (2003) and where organic matter content of SPM was the main cause of increasing $b_{SPM}*$ values toward deeper and more clear oceanic waters.

3.4.4 OPTICAL PROXIES OF PARTICLE SIZE AND COMPOSITION

The response of three optical composite variables (BOI^{size1}, BOI^{size2} and BOI^{comp}) to size and composition changes on SPM were evaluated in this study. Correlations between indices and SPM fractions showed that unlike BOI^{comp}, BOI^{size1} was very selective for indicating changes on particle micro-physical properties. Indeed, BOI^{comp} was correlated to F_{SPM}^{PIM} and the mass contribution of relatively small (0.2-0.4 µm) and large (>10 µm) particulates. This lack of specificity may respond to the use of a spectral range where phytoplankton has a maximum light absorption peak (i.e., 675 nm). As phytoplankton cells becomes larger (e.g., above 20 µm), chlorophyll *a* increases (Montes-Hugo et al., 2008). As result, the magnitude of a_{SPM} at 675 nm is expected to increase affecting positively BOI^{comp}. Lastly, BOI^{size1} and BOI^{size2} response was mainly associated with variability of large-sized and small-sized SPM fractions, respectively. This selectivity is particularly interesting as both indexes may be combined for developing more robust metrics for estimating SPM size spectra distributions in littoral waters.

3.5 CONCLUSIONS

The measure of optical cross sections of SPM is essential for developing optical inversions and improve our understanding regarding the origin of optical signatures in remote sensing studies and map biogeo-chemical components in surface waters. In this contribution, we presented for the first time, mass-specific scattering and absorption coefficients of size

fractioned SPM in estuarine waters of the Saint Lawrence River and a major SLE tributary, the Saguenay Fjord.

Despite the intrinsic variability of weight-normalized IOPs due to variations of particle micro-physical attributes, the following trends were observed: 1. the mass-specific absorption coefficient of SPM was preferentially influenced by changes in particle chemical composition, 2. particle size had a larger impact on b_{SPM}^* than a_{SPM}^*, and 3. optical proxies of SPM size distribution BOI^{size1} was more specific than optical proxy related to particle chemical composition (i.e., BOI^{comp}). These relationships are anticipated to be useful in the context of predicting mass-specific IOPs based on satellite remote sensing measurements.

3.6 FUNDING

3.7 ACKNOWLEDGEMENTS

3.8 APPENDIX
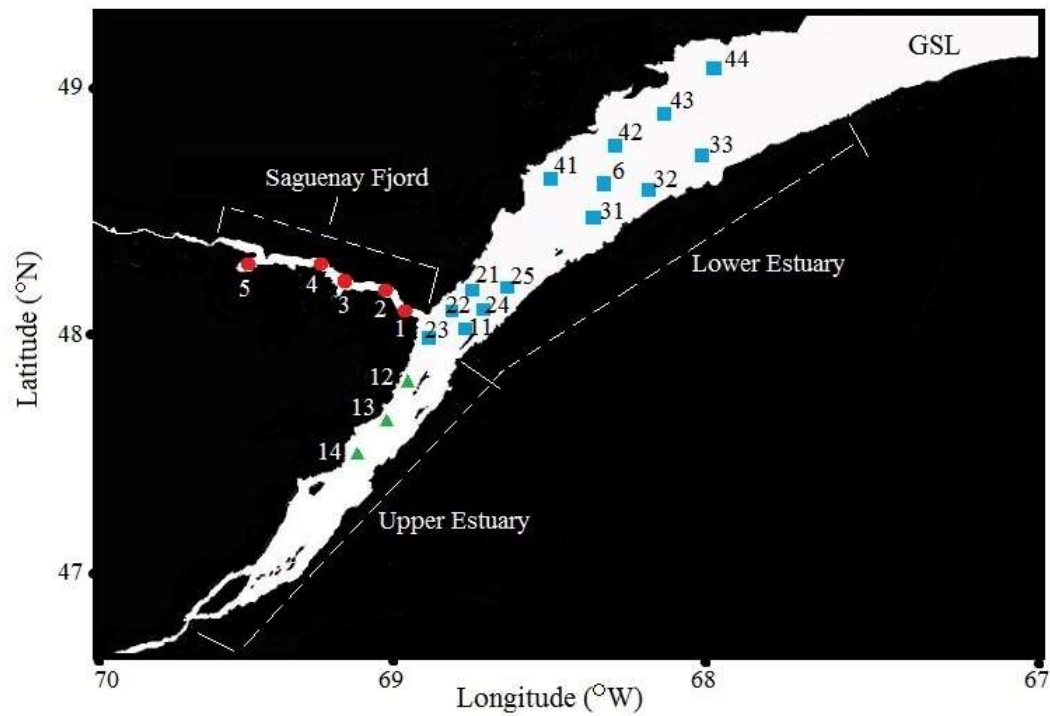
Figure S1. Study area. Sampling locations for the UE (green triangles), LE (blue rectangles), and SF (red circles) are indicated. GSL is the Gulf of St. Lawrence.

Table S1. Spearman rank correlation between particulate IOPs of different SPM size fractions, γ, and F_{PIM}. For each comparison, first, second, third and fourth value corresponds to the wavelength of 440, 556, 665 and 708 nm, respectively. The number of sampling locations is 23 in all cases. The statistical confidence level at 95 and 99% are symbolized with * and **, respectively.

	γ	$F_{SPM}{}^{PIM}$
$a_{SPM}{}^{0.2\text{-}0.4\ \mu m}$	-0.17*, 0.21**, 0.01,0.01	0.10*,0.29**,0.12*,0.12*
$a_{SPM}{}^{0.4\text{-}0.7\ \mu m}$	0.31**,0.07,0.33**,0.20*	0.62**,-0.17*,0.35**,0.36**
$a_{SPM}{}^{0.7\text{-}10\ \mu m}$	0.07,0.31**,0.07,0.11*	-0.17*,0.62**,-0.02,0.01
$a_{SPM}{}^{>10\ \mu m}$	0.21**,0.30**,-0.30**,0.08	0.29**,0.42**,0.15*,0.01
$b_{SPM}{}^{0.2\text{-}0.4\ \mu m}$	-0.29**,0.26**,-0.30**,-0.25**	-0.03,0.16*,0.15*,0.19*
$b_{SPM}{}^{0.4\text{-}0.7\ \mu m}$	-0.21**,0.18*,-0.21**,-0.16*	-0.15*,0.28**,-0.10,-0.06
$b_{SPM}{}^{0.7\text{-}10\ \mu m}$	0.50*,0.16*,0.50**,0.41**	0.28**,0.01,0.16*,0.17*
$b_{SPM}{}^{>10\ \mu m}$	0.34**,0.05,0.24**,0.19*	0.59**,-0.13*,0.52**,0.44**

Table S2. Relationships between optical remote sensing proxies and mass-normalized IOPs of SPM. For each Spearman Rank correlation coefficient, the statistical confidence level at 95 and 99% are symbolized with * and **, respectively. Mass-normalized absorption and scattering coefficients correspond to a λ of 440 and 550 nm, respectively.

	BOI [size 1]	BOI [size 2]	BOI [comp]
$a_{0.2\text{-}0.4\ \mu m}$ *	-0.03	0.16*	-0.14*
$a_{0.4\text{-}0.7\ \mu m}$ *	-0.47**	0.49**	0.06
$a_{0.7\text{-}10\ \mu m}$ *	-0.44**	0.45**	0.06
$a_{>10\ \mu m}$ *	-0.64**	0.74**	0.04
$b_{0.2\text{-}0.4\ \mu m}$ *	-0.29**	0.19*	-0.03
$b_{0.4\text{-}0.7\ \mu m}$ *	-0.19**	0.04	-0.02
$b_{0.7\text{-}10\ \mu m}$ *	-0.17*	0.02	-0.04
$b_{>10\ \mu m}$ *	-0.43**	0.35**	0.03

Table S3. Relationships between size and chemical fractions of SPM. Each relation and statistical confidence is described in table 2. N the number of stations is 23.

	F_{SPM}^{PIM}
$F_{SPM}^{0.2-0.4\ \mu m}$	0.27 **
$F_{SPM}^{0.4-0.7\ \mu m}$	0.15 *
$F_{SPM}^{0.7-10\ \mu m}$	0.08
$F_{SPM}^{>10\ \mu m}$	-0.27 **

Table S4. Relationship between chlorophyll a concentration and γ. Each relation and statistical confidence is described in Table S2.

	γ	N
UE	-0.08	3
SF	0.62 **	4
LE	-0.45 **	14

CHAPTER 4

EFFETS THERMIQUES DÛS À LA PRÉSENCE DE LA MATIÈRE PARTICULAIRE EN SUSPENSION DANS LES EAUX ESTUARIENNES ET LITTORALES

Ce troisième article, intitulé « *Thermal effect of suspended particulate matter (SPM) in estuarine and littoral waters*», fut corédigé par moi-même ainsi que par les professeurs Martin A. Montes-Hugo, Jean-Pierre Gagné, et Pierre Larouche. L'article sera soumis au Journal of Geophysical Research. En tant que premier auteur, ma contribution à ce travail fut de proposer et de développer l'idée originale, d'effectuer les recherches bibliographiques sur l'état de la question, de développer la méthode présentée dans cet article, et d'exécuter des tests de performance. Le professeur Martin A. Montes-Hugo, deuxième auteur, a aidé à la recherche sur l'état de l'art, au développement de la méthode ainsi qu'à la révision de l'article. Les professeurs Jean-Pierre Gagné et Pierre Larouche ont aidé à la recherche sur l'état de l'art ainsi qu'à la révision de l'article.

Résumé

La variabilité spatiale et temporelle de la matière particulaire en suspension dans les environnements littoraux joue un rôle majeur affectant la visibilité dans l'eau et l'échange de chaleur à travers l'interface air-mer. Les variations de turbidité de l'eau en raison de la présence de matières particulaires en suspension peuvent affecter indirectement des variables météorologiques locales (par exemple la température de l'air et l'humidité relative) à cause de modifications thermiques au sein de la couche de surface mélangée. Dans cette étude, nous expliquons les effets de ces modifications thermiques sur les modifications potentielles des conditions météorologiques locales. En outre, nous décrivons les mécanismes expliquant comment la lumière du soleil est atténuée par les composants optiques de l'eau et se convertit en chaleur rayonnante. Des études de terrain suggèrent que l'influence thermique des composés organiques dissous colorés et des matières particulaires en suspension peuvent être comparables. Comme les composés organiques dissous colorés, la production de chaleur induite par les particules peut avoir des influences considérables sur la variabilité climatique régionale. Ces changements peuvent affecter la distribution et ainsi la contribution des composants optiques responsables des effets thermiques sur les variations spatiale et temporelle de la fonte des glaces, des changements sur la nébulosité, et la répartition inégale de l'insolation.

THERMAL EFFECT OF SUSPENDED PARTICULATE MATTER (SPM) IN LITTORAL WATERS

Mohammadpour G. [1], Montes-Hugo M. [1], Gagne J.-P. [1], Larouche P. [2]

[1]Institut des Sciences de la Mer de Rimouski, Université du Québec à Rimouski, Québec, Canada

[2]Institut Maurice-Lamontagne, Pêches et Océans Canada, Québec, Canada

Abstract

The spatial and temporal variability of suspended particulate matter (SPM) in littoral environments has a major role affecting water visibility and heat exchange through the air-water interface. Water turbidity variations due to SPM may affect local weather variables (e.g., air temperature and relative humidity) due to thermal modifications within the upper mixed layer. In this study, we explain the effects of these thermal modifications to potential modifications of local weather conditions. Besides, we describe the mechanisms explaining how sunlight is attenuated by the water optical components and is converted into radiant heat. Field studies suggest that thermal influence of colored dissolved organic components (CDOM) and SPM can be comparable. Like CDOM, particle-mediated heat production can have substantial influence on regional climate variability. These changes may affect the distribution and thus, the contribution of optical components responsible for thermal effects on spatial and temporal variation in ice melting, changes on cloudiness patterns, and uneven distribution of solar insolation.

4.1. INTRODUCTION

The understanding of heat balance in littoral and oceanic waters has major implications for biogeochemical processes and development of circulation models. In that regard, the upper mixed layer plays an important function by absorbing solar radiation and modulating the air temperature just above the water surface (Donohoe et al., 2013). This redistribution of energy is modulated by changes in inherent optical properties (IOPs), local meteorological conditions (i.e., wind, cloudiness, precipitation), and hydrodynamics processes (e.g., advection, diffusion) (Adler et al., 2013; Boss et al., 2009; Guézennec et al., 1999; Verspecht and Pattiaratchi, 2010). Note that alterations in IOPs are mainly driven by concurrent variations in dissolved (e.g., CDOM) and particulate (e.g., phytoplankton and non-algal particulates) optical components. In general, in littoral environments influenced by fresh water discharge, changes in optical properties may be larger compared with marine environments (Zhang et al., 2010).

The solar energy reaching the ocean surface is about 50% of the solar energy at the top of the atmosphere, and is mainly composed of visible light (wavelength = 350 – 700 nm) (Arancibia-Bulnes et al. 2000). One percent of this energy is lost to scattering and absorption before entering the water column (Bricaud et al., 1998). The rate of light attenuation with depth is variable and depends on the concentration of optical components and their vertical distribution. On average for coastal waters, sunlight may penetrate up to 20 m within the first optical depth = xc, where x is actual depth and c is beam attenuation coefficient in m^{-1}, (Kirk, 1994).

The 1% light level (often inaccurately called the euphotic depth) is the depth at which photosynthetically available at noon falls to 1% of its value just below the sea surface. The rate at which light is attenuated is spectrally dependent. UV and green light (300 and 550 nm) may be still measured at depths up to 50 and 100 meters, respectively (Helbling et al.,

2003) in open oceans with minimal phytoplankton and CDOM concentrations. Conversely, near-infrared light (700-1000 nm) is rapidly attenuated within the first meter of the water column (Gitelson et al., 2008).

The sea surface temperature (SST) is a leading factor that governs weather patterns, thus it plays a key role in constraining atmospheric models. Although surface temperature measurements are obtained from multiple platforms (e.g., satellites, ships, buoys, coastal weather stations), this information is insufficient for very accurate weather model simulations due to their limited spatio-temporal resolution. This constraint may lead to large model uncertainties in terms of predicting local weather variables (e.g., wind speed, relative humidity). Small-scale variations in SST due to water constituents may be amplified at the regional scale by affecting air temperature, pressure, and circulation (Isobe et al., 2014). Likewise, these perturbations can be rapidly (i.e., on a scale of days) propagated by weather systems (e.g., synoptic-scale pressure depression systems) across the world (Isobe et al., 2014).

In general, climate variability affects coastal turbidity plumes through affecting the magnitude of transported SPM and CDOM towards coastal regions by increasing riverine output or coastal runoffs (Garcia et al. 2015), and cause local atmospheric pressure depressions, which lead to change in wind speed and velocity (Qiu and Kelly 1993). Wind-induced and tidal resuspension may have a major impact on the concentration and spatial distribution of SPM, and associated variations in light attenuation within the top layer of water column (Ruiz et al., 1994). Off the southwestern Australia, Verspecht and Pattiaratchi (2010) found that wind-induced waves were the dominant mechanism driving the vertical redistribution of particulate matter. They also found that daily see breezes were effective in holding particulate matter in suspension. The change in wind speed may also affect the release of water vapor and thermal energy at the water surface. These meteorological modifications may cause significant variations on vertical light penetration due to changes

on atmospheric transmission. At the same time, this effect is modulated by water turbidity and concentration of particulates inside of ice layers (Handorf et al., 2015; Hessen et al., 2010). Thus, rivers are major sources of SPM and CDOM towards downstream watersheds during ice melting periods.

In this chapter, the effect of different water optical components on heat budget terms are discussed with special emphasis on the influence of SPM on SST. Likewise, an important part of the review is devoted to understand relationships between weather patterns and particle-mediated thermal effects. The present chapter is organized in five sections. The first section encompasses the introduction and provides an overview about the heat balance between the atmosphere and the upper mixed layer of the ocean. In the second section, remote sensing variables related to heat budget parameterizations are discussed. In the third section, a simple thermodynamic model is described for the upper ocean. In the fourth section, the water heating due to SPM and CDOM, and its relationship with climate variables is analyzed for littoral waters. Lastly, in the fifth section, a list of potential long-term effects of particle-mediated heat variations in regional climate variables is summarized for different estuarine and coastal systems.

4.2 AIR-WATER HEAT FLUX COMPONENTS

The ocean and the atmosphere have a fundamental role in redistributing the incoming Sun's energy over the Earth's surface. This ocean-atmosphere coupling modulates the global exchange of heat and momentum, and the local dynamics of weather variables. Likewise, these energy pathways may suffer alterations due to distribution changes in SST associated with SPM and CDOM.

4.2.1 HEAT BALANCE TERMS

The exchange of heat across the atmosphere-ocean interface Q_T can be partitioned based on the following components (Komori et al., 2011):

$$Q_T = Q_H + Q_E + Q_R \tag{1}$$

where Q_H is the sensible heat flux, Q_E is the latent heat flux, and Q_R is the radiative heat flux in W m^{-2}. By assuming a temperature (ΔT) and specific humidity (Δq) difference across the air-sea boundary (i.e., the ratio of the water vapor content of the mixture to the total air content per unit of mass), Q_H, Q_E, and Q_R heat fluxes can be computed as follows:

$$Q_H = \rho_a C_{p,a} C_H U \Delta T \tag{2}$$

$$Q_E = \rho_a L_V C_E U \Delta q \tag{3}$$

$$Q_R = (\varepsilon \alpha T^4) A \tag{4}$$

where C_H and C_E are the coefficients of sensible and latent heat fluxes [W s^{-1} Kg^{-1} K^{-1}], respectively, ρ_a is the air density [kg m^{-3}], $C_{p,a}$ is the specific heat of air at a constant atmospheric pressure [W s^{-1} kg^{-1} K^{-1}], T is temperature [K], U is the wind speed above the air-sea interface [m s^{-1}], L_V is the evaporative latent heat coefficient [W s^{-1} kg^{-1}], ε is the thermal emissivity coefficient, α is the thermal diffusivity coefficient [m^2 s], and A is the area of exposure [m^2].

4.2.2 PHYSICAL FACTORS INFLUENCING HEAT BALANCE TERMS

Multiple energy pathways drive the exchange of heat between the atmosphere and the ocean surface. Longwave and shortwave radiation warms the ocean and provides energy to drive weather and climate. A fraction of this energy is stored in the ocean (~45%), and another fraction contributes to the atmosphere warming (~35%). Lastly, the the evaporation of water accounts for remaining energy fraction (~20%) (Kirk, 1988).

In the midlatitudes and as climatological averages (Sakai and Nozaki, 1995) (**Figure 1**), the atmosphere absorbs 67 W m^{-2} of shortwave radiation and 350 W m^{-2} of reflected and emitted longwave radiation from the surface. Indeed, the atmosphere emits 165 and 30 W m^{-2} of longwave and shortwave radiation, respectively. In addition, the absorbed energy by the earth, including land and ocean, is 168 W m^{-2} and 333 W m^{-2} for short and longwave radiations, respectively. Also, the Earth's surface emits 195 W m^{-2} of longwave radiation to space. The ocean's surface, in contrast, gains 168 W m^{-2} of shortwave solar radiation and 324 W m^{-2} of longwave back radiation from the atmosphere and clouds. However, the earth's surface emits 350 W m^{-2} of longwave radiation to the atmosphere. This balance results in a net surplus of energy from the earth to the atmosphere of 102 W m^{-2} (Q_H = 24 W m^{-2}, Q_E = 78 W m^{-2}). It must be noted that latent heat flux and net infrared (IR) radiation tend to balance insolation. Moreover, the magnitude of Q_E is always small with respect to Q_H and Q_R (~24%).
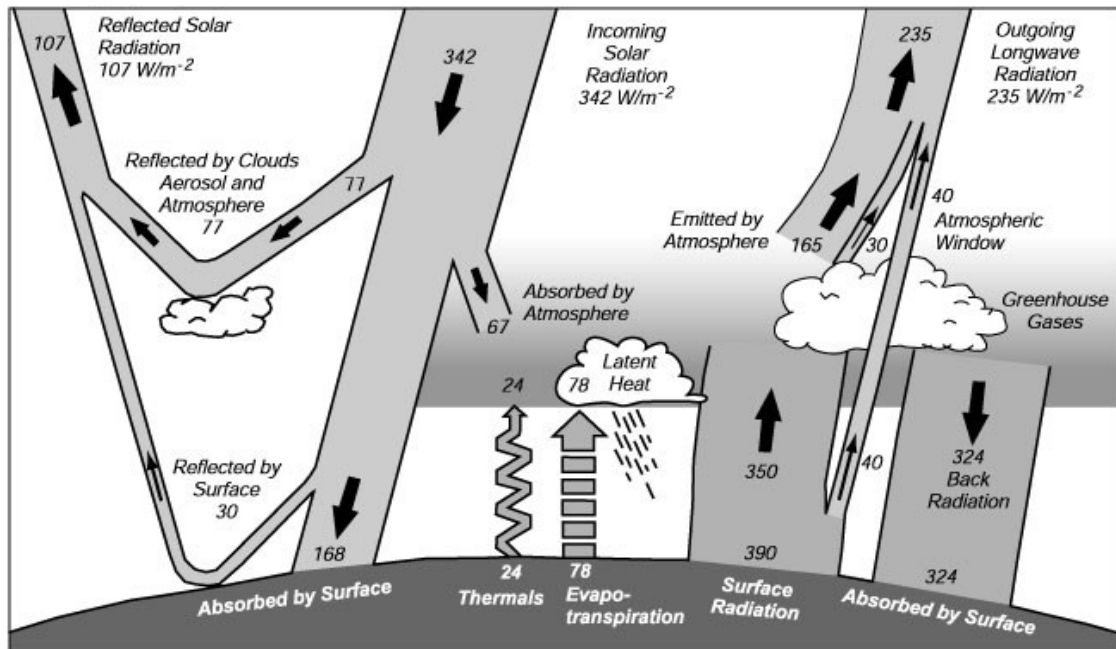
Figure 1. Net heat flux at the ocean-atmosphere interface (www.nasa.gov)

Wind modifies the magnitude and variability of Q_E by injecting air into the water and changing the amount of water vapor just above the air-water interface (Sakai and Nozaki, 1995). More specifically, the displacement of air above water changes the vapor saturation state of the air and the heat fluxes across the air-water interface (Kubota et al., 2003). In general, latent heat fluxes increase at higher wind speeds and are linked to large changes on ocean-atmosphere humidity gradients (Feng and Li, 2006; Yu et al., 2011).

To investigate the effect of water constituents on underwater solar radiation and calculate the terms in Equations (1-4), we need to estimate the amount of transmitted solar radiation within visible and IR wavelengths going to the water column. Following Kirk (1994), the solar transmission at the water depth z, $(T_r(z)$ is defined as:

$$T_r(z.\lambda) = \frac{E_n(z.\lambda)}{E_d(0^-.\lambda)} \tag{5}$$

$$E_n(z.\lambda) = E_d(z.\lambda) - E_u(z.\lambda) \tag{6}$$

where $E_n(z.\lambda)$, $E_d(z.\lambda)$, and $E_u(z.\lambda)$ are spectral net, downwelling, and upwelling irradiance (W m^{-2} nm^{-1}), respectively.

The fraction of solar radiation that leaves the water surface is given by:

$$\alpha(\lambda) = \alpha_a(\lambda) + \alpha_b(\lambda) \tag{7}$$

$$\alpha_a(\lambda) = 1 - \frac{E_n(0^-.\lambda)}{E_d(0^+.\lambda)} \tag{8}$$

where $\alpha(\lambda)$ is the water-surface reflectance. α, is often defined as a combination of water-leaving radiation, $\alpha_a(\lambda)$, and Fresnel reflection, $\alpha_b(\lambda)$ (Ohlmann et al., 2000). For a layer of thickness z, the radiant heat rate (RHR(z)) in ºC s^{-1} is defined as:

$$RHR(z) = \frac{E_n(0^-.\lambda) - E_n(z.\lambda)}{z\,\rho_w(z)\,c_p} \tag{9}$$

where $E_n(0^-.\lambda)$ denotes the total spectral net flux of solar radiation within UV – IR spectral range (350 – 800 nm) and just below the sea surface, $\rho_w(z)$ is the density of seawater [kg m^{-3}] at depth z [m], and c_p is the specific heat of water [W s^{-1} kg^{-1} K^{-1}]. For the same depth interval and spectral range, the RHR is expected to be higher at IR wavelengths, due to their rapid attenuation of this energy within the spectral range 700 – 1700 nm (Chang and Dickey, 2004).

The heating rate beyond this depth only depends on attenuation of UV and visible light. This light extinction depends on optical properties of water constituents, as CDOM highly absorbs light at UV – blue spectra (wavelengths shorter than 450 nm), and water absorbs at relatively long wavelengths (i.e., > than 650 nm). Additionally, algal and non-algal particles

have a major contribution to light absorption in UV-blue spectral range, and light scattering at wavelengths above 500 nm (Mobley, 1994; Zhai et al., 2011) (**Figure 2**).
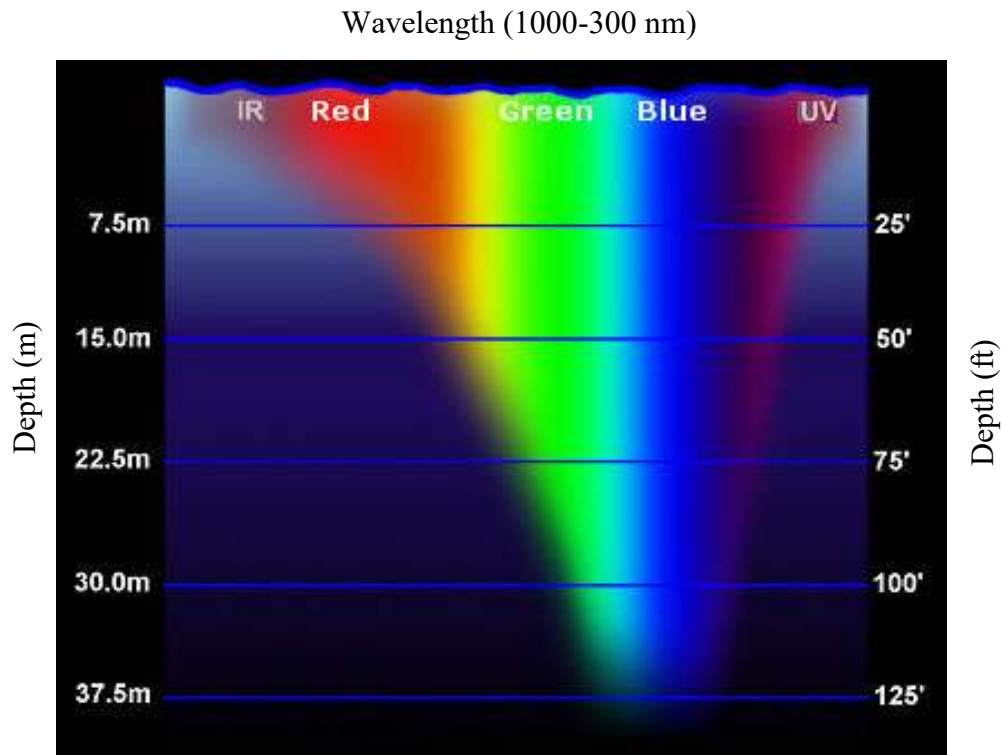
Figure 2. The penetration of light spectra in coastal waters (adapted from oceanexplorer.noaa.gov)

The presence of clouds can decrease the RHR by half and within the top 10 m of the water column (Siegel et al., 1999). Indeed, clouds decrease the magnitude of RHR through making the light more diffused and increasing the importance of upward E_u compared with E_d.

4.3 REMOTE SENSING OF HEAT BALANCE TERMS

The characterization of heat budgets over a large spatial extent is commonly performed using satellite-based observations. Conversely, planes and balloons are usually used to validate satellite-derived products related to heat budget components retrievals. Satellite-based heat budget measurements are commonly used in ocean circulation and climate models. The most important spaceborne variables for estimating heat balance terms shown in equations (1 – 9) are temperature, wind, and $E_d(\lambda)$. This section is mainly focused on describing heat budget parameters obtained from spaceborne and *in situ* sensors that allow synoptic mapping of heat budget variables over spatial domains and scales comparable to meso-scale (as high as 500 km) oceanographic features. Likewise, this spatial domain has a major relevance for climate variability studies (Reynolds et al., 2002).

4.3.1 SATELLITE MEASUREMENTS

In 1975, the first geostationary imager, GOES (Geostationary Operational Environmental Satellite), with visible and thermal capabilities was launched (Lombardi and Hanson, 2005). After several years, multiple GOES sensors were set in orbit (assemblage) providing different heat budget products (e.g., ocean heat content, radiation components, SST) at high temporal (i.e., 15 minutes) but low spatial resolution (i.e., ~30 km).

The advanced very high resolution radiometer (AVHRR), the first polar-orbiting sensor able to measure SST, was launched on 1985 (Fusco et al., 1989). AVHRR has enough spectral bands for better estimating heat budget parameters such as solar radiation and cloud cover. Unlike GOES, AVHRR observations are daily and with a spatial resolution of 1.1 km. Also, the accuracy of AVHRR for measuring SST is higher (± 0.5 °C) compared with GOES-

8 (± 1℃). These uncertainties are of special interest for climate studies since they have a direct impact on heat budget error calculations in terms of Q_R.

The advanced along-tracking scanning radiometer (AATSR) is a sun-synchronous sensor that was designed to retrieve global SST with an accuracy of ± 0.3 ℃ (Corlett et al., 2006). In addition to more accurate SST estimates, AATSR has a higher spatial resolution (1 km) compared with GOES. Unlike GOES, AVHRR and AATSR, the spaceborne sensor TIROS operational vertical sounder (ATOVS) consists of a high-resolution radiation sounder (HIRS), the advanced microwave sounding unit-A (AMSU-A), and AMSU-B for estimating temperature and humidity in all weather conditions with a 60-km resolution (40 km nadir) by a microwave sounder. ATOVS is capable of measuring sea surface temperature, surface skin temperature, and outgoing longwave radiation. Despite the vertical profiling capabilities of ATOVS and the fact that the sensor measures the SST with ± 0.5 ℃ of accuracy, this sensor has a coarse spatial resolution (60 km) with respect to AVHRR (1.1 Km), GOES (30 Km), and AATSR (1 km). Despite of their widespread use, satellite-based IR remote sensing measurements may have a significant bias of ~50% due mainly to atmospheric effects such as aerosols, rain and fog that contribute in absorbing light within IR and SWIR wavelengths (Wang, 2010). Thus, *in situ* SST measurements are essential to validate and complement space-based retrievals.

4.3.2 SHIPBOARD AND MOORING MEASUREMENTS

Field measurements of heat budget variables are commonly applied for validating satellite measurements and filling data gaps originated from missing satellite pixels. Thermal data can be derived from buoys, underway continuous flow systems, CTD profiles, and onboard radiometers attached to the deck of oceanographic vessels (Kearns et al., 2000).

Unlike satellites, atmospheric effects do not influence ship-based radiometers, thus their estimates mainly depend on skin temperature variations. Notice that the skin temperature is the temperature of the microlayer (i.e., layer just underneath the water surface and encompassing a thickness of mm). This temperature is slightly ($\sim 0.01 - 0.1$ ℃) different with respect to the bulk temperature of the upper mixed layer (Minnett et al., 2001). Ship-based radiometers can autonomously measure SST with an accuracy of ± 0.16 ℃ (Jessup and Branch, 2008; Donlon et al., 2002; Branch et al., 2008).

The SST sensors attached to buoys are mainly used for monitoring regional climate. Buoys provide a higher temporal resolution for estimating Q_R and Q_H with respect to shipboard observations. However, their spatial resolution is coarser, as high as 600 Km, with respect to ship-derived measurements. To gain synoptic measurements, the data obtained by buoys are distributed through a data distribution system such as the Global Telecommunication System of the World Meteorological Organization. This coordination is essential to obtain global climatology with a temporal resolution of less than 3 h (Wallace, 2012).

4.4 THERMODYNAMIC MODELS COUPLED TO CIRCULATION

As solar energy enters the water column, most of the photons are absorbed by suspended and dissolved optical components and transformed into heat (Morel and Antoine, 1994). Likewise, on a clear day at mid latitudes, phytoplankton absorbs about half of the solar flux, particularly between 350 and 700 nm, where it can be used to drive photosynthesis, creation of organic matter, and/or inelastic dissipation as fluorescence (phytoplankton, CDOM, and Raman), and thermal effects (Lewis et al., 1983; Shell et al., 2003). One small fraction ($\sim 1\%$ depending on water turbidity) of the solar energy entering the aquatic medium is returned to

the atmosphere due to the molecular and particulate backscattering (Kirk, 1988). Likewise, depending on vapor pressure and aerosol composition, one portion of these upwelling photons are further absorbed and converted into heat by aerosols and water vapor (Holland et al., 2011). These heat pathways are simultaneous and cannot be studied based on direct methods. Thus, thermodynamic models coupled to hydrodynamics must be used (Djoumna et al., 2014; Jolliff and Smith, 2014). In physical oceanography, thermodynamic models have shown that horizontal advection may be responsible for 90% of heat flux variability in surface littoral waters. Likewise, it has been shown that biota weakly ($\sim 3\%$) participates in this process. Also, numerical experiments in oceanic waters suggest that vertical mixing is the primary mechanism (up to 80 %) of modulating air-water heat transfer (Oschlies, 2004).

Over relatively large areas (i.e., 600-1000 km) and periods of time (i.e., years to decades), heat budget can be simplified as advection effects are reduced (Gordon et al., 2000; Morel, 1988; Strutton and Chavez, 2004). In the Gulf of California, Castro et al. (1994) used a simple model to compute the net surface heat flux based on monthly heat content variation between 0 and 400 m depth by:

$$H(t) = \int_V \rho C_p T(x, t) dV \tag{10}$$

where $T(x, t)$ is the temperature profile [°C], C_p is calculated from Millero et al. (1973), and dV [m^3] are the volume elements centered at the standard depths calculated from the bathymetry. In order to remove high seasonal variability and derive inter-annual trends, they fit a seasonal signal by least squares:

$$H(t) \cong H_0 + H_1 \cos \omega t + H_2 \sin \omega t \tag{11}$$

where $\omega = 2\pi/365$ day^{-1}, t is the time in days from January 1st, and H is annual harmonic in the Fourier series. Finally, they measured net heat flux values computed from meteorological

data with theoretical estimates as derived from the following equation Lavin and Organista (1988):

$$Q(t) \cong Q_0 + Q_1 \cos \omega t + Q_2 \sin \omega t \qquad (12)$$

Jolliff et al. (2012) used a coupled numerical model for calculating the ocean biological feedback in Monterey Bay, California. More specifically, they combined a coupled ocean-atmosphere mesoscale prediction system (COAMPS) with a nested numerical modeling system developed at the Naval Research Laboratory (NRL). During this process, they assessed the thermal impact of phytoplankton blooms in the Monterey Bay through investigating the sensitivity of their modeling system to changes on oceanic optical shortwave attenuation. They found that light attenuation by phytoplankton blooms can increase the local air temperature (up to $\sim 2°C$) and produce air-sea fluxes on short time scales (i.e., a few hours). Also, they suggest that the influence of suspended and dissolved matter (e.g., CDOM) on heat budget variables (i.e., Q_H, Q_R) is comparable to phytoplankton at the air-sea interface.

A more complex parameterization of temperature changes due to variations on RHR and hydrodynamics is (Kako and Kubota, 2009; Qiu and Kelly, 1993):

$$h\frac{\partial T}{\partial t} + U.\nabla T = A_h h\nabla^2 T + \frac{1}{\rho c}(Q - q_{z=-h}) - \Delta T(W_e + A_h\nabla^2 h) \qquad (13)$$

$$\frac{1}{2}\alpha gh\Delta T W_e = m_0 u *^3 + \int_{-h}^{0} q(z)dz - \frac{\alpha gh}{2\rho c}(Q + q_{z=-h}) - m_c\frac{\alpha gh}{4\rho c}(|Q| - Q) \qquad (14)$$

where h is the mixed layer depth and U is the horizontal velocity in the uppermost layer of the mixed layer. Constants A_h, ρ, c, α, ΔT, and g are the horizontal viscosity (10^3 m²s⁻¹), seawater density (1028 kgm⁻³), specific heat of seawater (3930 Jkg⁻¹K⁻¹), thermal expansion coefficient of seawater (2.5×10^{-4} °C⁻¹), temperature difference between the mixed layer and water just below it (0.5 °C), and gravitational acceleration, respectively. The two adjustable

constants m_0 and m_c may be chosen 0.5 and 0.83, respectively (Qiu and Kelly, 1993). Likewise, Q denotes net heat flux through the sea surface that can be computed using the bulk formulas in Kondo (1975) with modeled SST, gridded wind speeds, and other atmospheric properties furnished by the national centers for environmental prediction (NCEP)- national centers for atmospheric research (NCAR) reanalysis products (Kalnay et al., 1996). Friction velocity (u_*) can be computed using wind speed, with air density of 1.2 kgm^{-3} and drag coefficient of 1.2×10^{-3}. Other notations are standards, unless otherwise is stated. In the left hand side of the equation, local and advective change of temperature are denoted, respectively. The terms on the right side show the diffusive effect of heat flux on temperature in the upper mixed layer. The environment velocity W_e at the bottom of the mixed layer is computed from Eq. (14). Heating by water constituents is incorporated into the downward radiative flux (Manizza et al., 2005):

$$q(z) = 0.58I_0 + I_{RED}e^{-k_r z} + I_{BLUE}e^{-k_b z} \tag{15}$$

where I_{RED} and I_{BLUE} are the irradiance in red and blue bands, respectively, and can be derived from the NCEP-NCAR re-analysis product. Attenuation coefficients of particulates for the visible wavelength bands with red/yellow (k_r) and blue/green (k_b) colors in Eq. (15) can be derived from the IOPs data obtained from in situ and previously-derived models (Isobe et al., 2014; Manizza et al., 2005; Morel, 1988). In summary, the computational procedure requires boundary conditions for ocean currents to solve Eq. (13) numerically, through solving entrainment velocity by Eq. (14) and downward radiative flux by Eq. (15).

4.5 IMPACT OF SPM AND CDOM ON SST AND RHR

Studies show the effect of suspended and dissolved particles on modulating RHR through light attenuation and diffusion in littoral waters (Nielsen et al., 2002; Savage et al., 2002). In

the Gulf of Maine, Ackleson et al. (1994) and Balch et al. (2002) found that waters dominated by coccolithophore blooms have 5-fold higher heating rates (0.32 ℃ day^{-1}) compared with those where phytoplankton blooms were absent (0.06 ℃ day^{-1}). Kahru et al. (1993) found that algal particulates in the southern Baltic Sea affect heat budget components by affecting Q_R due to changes on reflectance. In this investigation, they found that the phytoplankton increased upward Q_R through increasing the reflectance. They also found that water temperature was in average higher (up to 1.5 ℃) in waters characterized by phytoplankton blooms. In coastal waters of east and south China Sea Wang and Tang, (2010) showed that algal blooms may increase SST up to 1 and 5 ℃ in spring and autumn in the East China Sea, respectively. This effect was attributed to the increase of solar radiation due to phytoplankton pigments.

At mid and high latitudes, Shell et al. (2003) modeled SST changes due to phytoplankton by coupling an ocean general circulation and an atmospheric general circulation model forced by phytoplankton chlorophyll measurements derived from ocean color satellite sensors. They found that the variation of SST due to phytoplankton was 0.1 – 1.5 ℃ and 0.1 – 0.3 ℃ during spring/summer and during fall/winter, respectively. Jolliff et al. (2012) found that optical attenuation associated with phytoplankton blooms in the Monterey Bay substantially impacts the thermal exchange between ocean and atmosphere. This investigation showed that phytoplankton blooms may cause a local atmospheric warming of 2 ℃ day^{-1}. Jolliff and Smith (2014) found that thermal stratification due to phytoplankton has also a positive feedback on phytoplankton growth and further vertical gradients of temperature and mixing reduction of the water column. Off Japan coast, Isobe et al. (2014) developed a radiative-convective model and found that phytoplankton may be responsible of SST changes of up to 1℃, in the Chukchi Sea during summer. The information is summarized in **Table 1**.

Table 1. Summarized information on previous studied on the thermal effects of particulates in coastal and oceanic waters

Study	Temperature change (℃)	Region
Isobe et al. (2014)	1	Chukchi Sea
Joliff et al. (2012)	2	Monterey Bay
Wang and Tang (2010)	1-5	East China Sea
Shell et al. (2003)	0.1-1.5	Global scale
Balch et al (2002)	1	Gulf of Maine
Ackleson et al. (1994)	1	Gulf of Maine
Kahru et al. (1993)	1.5	Southern Baltic Sea

CDOM and SPM have a comparable contribution to light absorption and RHR (i.e., ~50%) (Hill 2008). In Central Arctic surface waters, Pegau, (2002) found that within 30 – 50 % of UV radiation absorption (λ = 200 – 380 nm) is due to CDOM, and light absorption by CDOM in the top 10 m of water column and within the visible spectral range (λ = 350 – 700 nm) may increase RHR in ~30%. Off the New Jersey coast and during June-August 2001, Chang and Dickey (2004) found that light absorption due to CDOM and non-algal particles (NAP) may have larger (two folds) effects on RHR compared with phytoplankton.

4.6 PARTICLE-MEDIATED HEAT VARIABILITY AND WEATHER PATTERNS

The spatial variation of heat fluxes driven by suspended particulates influences the variability of temperature in the upper mixed layer of ocean and the lower atmosphere. These thermodynamic perturbations can have different impacts on local weather variables as sea ice and cloudiness, which are the focus of the following section.

4.6.1 SEA ICE

Manizza et al. (2005) showed that water heating due to phytoplankton may cause a reduction of sea ice cover (up to 6%) in summer. This is a major change with respect to the warming attributed to water and air temperature (~2%). Also, changes of SST due to phytoplankton growth has a positive feedback on ice melting (Manizza et al., 2005). In Arctic and Subarctic regions, under-ice phytoplankton blooms may cause a local increase in surface temperature and a change of heat flux during early spring (Nelson and Smith, 1986). In coastal waters, the impact of CDOM and NAP on sea ice melting is more important with respect to phytoplankton (Chang and Dickey, 2004; Dickey and Falkowsky, 2002). Based on a global model, Loptien (2011) studied relationships between water turbidity and SST in the Baltic Sea. The main finding of this study was that turbidity-mediated changes on SST may affect timing of sea ice (e.g., early retreats in spring and late formation in autumn).

4.6.2 CLOUDINESS

In the previous section, the influence of SPM on SST and convective oscillations in the atmosphere was discussed. Indeed, the formation of marine low clouds has been found to be substantially correlated with Q_H and Q_E (Ghate et al., 2009). In general, variations on Q_H are responsible of modifying cloud types, by transforming marine stratiform clouds into trade wind cumuliform clouds (Rosenfeld et al., 2006). Furthermore, the increase of surface sensible heat flux and/or latent heat flux can trigger the formation of open cell clouds, and subsequent precipitation (Wang et al., 2010). The resulting heat fluxes make the boundary layer thicker due to the larger vertical air velocities that favor the formation of thicker clouds and the initiation of rain events (Mechem et al., 2012). Due to SST variability, the paths of weather fronts can be slightly shifted (Senatore et al., 2014). Thus, it is expected that SST gradients due to SPM changes may alter trajectory of fronts. These atmospheric modifications may cause precipitation near coastal areas having mountains due to the displacement of humid air toward higher elevations, where orographic effects enhance rainfall intensity (Langhans et al., 2013).

4.6.3 AEROSOLS

Aerosols play a key role in cloud formation and type in coastal and marine regions. Kazil et al. (2014) showed that carbon-rich aerosols are highly hygroscopic and may play a role in shifting a convective cloud from a closed cell (i.e., without precipitation) to an open cell cloud (i.e., with precipitation) due to the formation of convective currents. In Tasmania, Australia, McCoy et al. (2015) showed that more than half of variations in cloud particles are principally originated from marine biogenic matter. Likewise, Krüger and Graßl (2011)

showed that in Southern Ocean, within 45°S and 65°S and during austral summer, phytoplankton blooms significantly participate in precipitation regime of the region by providing a major fraction of cloud condensation nuclei (CCN). These particles play a key role in providing suitable conditions for nuclei production and cloud formation. Likewise, spatial variations of algal and non-algal particulates can affect convective currents and subsequent cloud cover conditions over the region. Indeed, studies in mid latitudes show that spatial alterations of SST are associated to cloud cover and type and forms phytoplankton blooms (Isobe et al., 2014; Morel, 1988). Also, rain-derived turbidity plumes increase light attenuation at the top level of water column and increase the SST variation over the turbid zone (Nakamoto et al., 2001; Shell et al., 2003). These processes may accelerate the upward motion of marine aerosols and signify their effect on cloud formation and type. Despite the important role of organic particles, numerical simulations suggest that aerosols have a secondary influence on triggering precipitation in clouds with respect to temperature and moisture perturbations at the boundary layer (Wang et al., 2010; Mechem et al., 2012).

The National Aeronautics and Space Administration (NASA) has established the phytoplankton, Aerosol, Clouds and ocean Ecosystem (PACE) mission, tentatively scheduled to launch in 2022 to understand how the living ocean improve forecasts of earth system variability. The objective of this mission is to understand global ocean ecology, biogeochemistry, and carbon cycle based on global ocean color measurements and find their interrelationship with the Earth's climate, clouds, and aerosols (www.nasa.gov). Similarly, the European space agency (ESA) initiated a program in 2009 in response to the need for climate-quality data. Their objective was to ameliorate the quality of obtained data by satellite network and achieve more accurate responses from global climate models. During their program, they have been monitoring ocean-atmosphere variables such as aerosol, cloud, SST, and ocean color, and find their connection in global climate. Finally, to be launched in 2018 as a collaborating mission, the Japan aerospace exploration agency (JAXA) and ESA have established an earth observation satellite, so called EarthCARE. Their objective is to

use four sensors such as cloud profiling radar, backscatter Lidar, multispectral imager, and broadband radiometer, to observe clouds and aerosols on a global scale. This information helps to understand the details of aerosols and clouds for reducing crucial differences in climate change predictions.

4.6.4 CLIMATE FEEDBACKS

Global climate patterns are responsible for changing the intensity, duration, and frequency of weather conditions, which in turn have an influence on spatial and temporal distribution of dissolved and suspended particulate matter. Here, four climate indices are discussed, starting with the mode having the largest spatial and temporal influence on the eastern Canada climate, the Atlantic multi-decadal oscillation (AMO). Some posteriori, climate modes characterized by shorter periodicities, such as the North Atlantic oscillation (NAO), the multivariate ENSO index (MEI), and the Arctic oscillation, are examined.

The AMO is a mode of natural variability occurring in the North Atlantic Ocean and has a major influence in SST. The AMO is responsible of SST changes over the North Atlantic with a periodicity of 60-80 years. Multi-decadal variations have been found in drought and precipitation records in many regions around the world. McCabe et al. (2008) showed that AMO is the most consistent indicator of decadal to multi-decadal drought variability in the US during the 20th century. Droughts, based on their frequency, intensity, and duration, can enhance the thermal effects associated to SPM in coastal waters due to their major role in coastal and inland erosion. As result of land erosion more terrigenous particulates are transported toward littoral waters. Thus, nearshore waters become more turbid due to the formation of turbidity plumes (Jacobi et al., 2015). McCabe and Wolock (2014) showed that there is a positive link between the positive phase of AMO and the increase of SST and

precipitation in North America, while the negative phase is associated with smaller fluctuations of SST and precipitation. In Quebec, Assani et al. (2010) showed that AMO had a minor influence on river discharge along the north shore of the Gulf of St. Lawrence.

The NAO is the leading pattern of atmospheric variability occurring at middle and high latitudes influencing the North Atlantic Ocean (Pegau et al. 1997). Indeed, the NAO perturbation is related to a redistribution of air mass between the Arctic and the Sub-Tropical Atlantic Oceans. NAO has a positive phase that reflects below-normal geopotential heights with pressure systems across high latitudes of the North Atlantic, and above-normal geopotential heights with pressure systems over the central North Atlantic, the eastern United States and Western Europe.

The negative phase of NAO reflects an opposite pattern of height and pressure anomalies over central North Atlantic, the eastern United States and Western Europe. The NAO's change of phase takes place within a biennial to a decadal time scale (Hurrell and Loon, 1997). This phase shift generates changes on wind speed and direction, heat and moisture transport, SST, and storm characteristics (Wettstein and Mearns, 2002). Likewise, the NAO phase alteration has been associated to variation of river discharge in the northern hemisphere (Cayan, 1992). Thus, during a NAO^+ (positive phase), increase in fresh water supply increases the magnitude of transported particulates (Dickson et al., 1996). During the NAO^- (negative phase), Hátún et al. (2009) found a decrease of strength of the subpolar gyre. This hydrographic alteration was related to a decrease of phytoplankton population, and thus, decreasing the population of grazers. In the St. Lawrence Estuary and during the NAO^+, Assani et al., (2011) found an increase of river flow along the north shore of the St. Lawrence River water shed.

The MEI is a monthly index based on six main variables measured over the tropical Pacific Ocean: sea level pressure, zonal and meridional components of the surface wind, sea surface temperature, surface air temperature, and cloudiness (Gouirand and Moron, 2003).

The El Nino Southern Oscillation (ENSO) is the most important coupled ocean-atmosphere phenomenon to cause global climate variability at time scales from two to seven years and is highly correlated to the MEI (Spencer and Braswell, 2013). Indeed, negative and positive values of the MEI are characterized by cold (La Nina) and warm (El Nino) ENSO phases and lower and higher than normal SST, respectively, over central and eastern equatorial pacific.

The warm phase of ENSO is associated with weaker low-level atmospheric winds along the equator, enhanced convection across the entire equatorial pacific, increase in global SST, and stronger jet stream activities over North America during the El Nino winters (Shabbar and Skinner, 2004). Thus, it is expected that SPM increases during a warm ENSO over eastern Canada. Spencer and Braswell, (2013) reported that surface temperature and cloudiness decrease during a negative phase of ENSO, due to decrease of solar radiation reaching the ocean surface. During El Nino, the southern and central areas of Quebec are commonly associated to a greater intensity and duration of rainfalls characterized by an anomalous warm winter. Thus, a greater transport of terrigenous particulates toward the Estuary and the Gulf of St. Lawrence during winter are expected during El Nino years (Assani et al., 2011). Although not measured, this phenomenon is expected to increase the SST during early spring and late fall due to larger proportion of solar radiation absorbed by land-derived particulate matter.

The Atlantic Oscillation, also referred as AO, is a climate index that can be related to particle transport by rivers and land runoffs through affecting atmospheric conditions. It describes the atmospheric circulation over the Arctic, also referred as the northern hemisphere annular mode. The AO positive phase is characterized by below average geopotential heights associated with more atmospheric instability and precipitation, stronger winds, and more reduced SST, while during an AO$^-$, the sign of geopotential heights is reversed. An AO negative phase is associated with weakening of the polar low-pressure system (the polar vortex) over the Arctic, and consequently, weakening of upper level winds

(i.e., westerlies at these latitudes), which results in cold Arctic air displacements farther south into the U.S. (Wettstein and Mearns, 2002). Handorf et al. (2015) found a weak correlation between the negative phase of AO and the arctic snow cover and sea ice. In Quebec, Assani et al. (2011) showed that higher stream discharges along the south shore of the St. Lawrence watershed occurred during the AO^-, while the AO^+ was associated with less river discharges. The AO and NAO phases are positively correlated in North America.

The production of in-land mineral and organic particulates due to seasonal variation of air temperature during spring and winter over the eastern Canada and North America can be corresponded to AO^+ and NAO^+. Wettstein and Mearns (2002) showed higher temperatures in the U.S. and lower temperatures in Quebec, Canada, when the AO – NAO indices increase. During the $AO^+ – NAO^+$, the occurrence of very low temperatures in Quebec may increase the forest dieback (Auclair et al., 1996). Moreover, a tree or shrub starts to die due to extreme cold conditions and generates leaf residuals that can be later transported to nearshore waters by the spring freshets (Brodie and Dunn, 2010; McCabe and Wolock, 2014; Jiang and Zhang, 2015). Therefore, the phase variation of AO and NAO can be related to the variation in heat flux and surface water temperature in coastal waters due to variation in water constituents.

Table S1. List of acronyms

Abbreviation	Definition	Unit
AATSR	Advanced Along Track Scanning Radiometer	
AMO	Atlantic multi-decadal oscillation	
AMSU-A	Advanced microwave sounding unit-A	
AMSU-B	Advanced microwave sounding unit-b	
AO	Atlantic oscillation	
AOGCM	Atmosphere-ocean general circulation model	
ATOVS	Advanced TIROS operational vertical sounder	
AVHRR	Advanced very high-resolution radiometers	
CCN	Cloud condensation nuclei	
CDOM	Chromophoric dissolved organic matter	
CDR	Climate Date Records	
COAMPS	Coupled ocean – atmosphere prediction system	
CTD	Conductivity, temperature, and depth	
DOM	Dissolved organic matter	
EUMETSAT	European organization for the exploitation of meteorological satellites	
GAC	global area coverage	

GBN	Global Buoy Network
GHRSST	Group for High Resolution Sea Surface Temperature
GOES	Geostationary operational environmental satellite
GTS	Global Telecommunication system
HIRS	High resolution radiation sounder
HyspIRI	Hyperspectral infrared imager
IASI	Infrared atmospheric sounding interferometer
ISAR	Infrared Sea surface temperature Autonomous Radiometer
LDV	Laser Doppler velocimetry
LIDAR	Light detection and ranging
M-AERI	Marine-Atmosphere Emitted Radiance Interferometer
MEI	Multivariate ENSO index
MHS	Microwave humidity sounder
MIRS	Microwave integrated retrieval system
NAO	North Atlantic oscillation
NAP	Non-algal particles
NCEP	National Center for Environmental Predictions
NESDIS	National environmental satellite, data, and information service

NIR	Near-infrared	
NOAA	National oceanic and atmospheric administration	
NRL	Naval research laboratory	
PACE	Pre-aerosol Clouds and ocean Ecosystem	
PIV	Particle image velocimetry	
PSU	Practical salinity units	
RHR	Radiant heat rate	
RMSE	Root mean square error	
SAR	Synthetic aperture radar	
SISTeR	Scanning Infrared Sea Surface Temperature Radiometer	
SSEC	Space science and engineering center	
SSM/I	Special sensor microwave imager	
TIR	Thermal infrared	
TIROS	Television Infrared Observation Satellite	
TOA	Top of the atmosphere	
UV	Ultra violet	
VOS	Voluntary observing ships	
WMO	World Meteorological Organization	
$\nabla^2 T$	Laplacian of temperature	$°C^2\ m^{-2}$

A_h	Horizontal viscosity	$m^2 s^{-1}$
$q_{z=-h}$	Heat flux at the depth h	W
W_e	Environment velocity	$m\ s^{-1}$
C_E	Coefficient of latent flux	$KJ\ kg^{-1}\ K^{-1}$
C_H	Coefficient of sensible flux	$KJ\ kg^{-1}\ K^{-1}$
$C_{p,a}$	Constant pressure specific heat of air	$KJ\ kg^{-1}\ K^{-1}$
$E_d(z.\lambda)$	Spectral downwelling at the depth z	$w\ m^{-2}\ nm^{-1}$
$E_n(z.\lambda)$	Net irradiance profiles at the depth z	$w\ m^{-2}\ nm^{-1}$
$E_u(z.\lambda)$	Upwelling irradiances at the depth z	$w\ m^{-2}\ nm^{-1}$
I_{BLUE}	Irradiance in blue band	$W\ m^{-2}$
I_{RED}	Irradiance in red band	$W\ m^{-2}$
L_V	Evaporative latent heat	W
Q_E	Latent heat flux	W
Q_H	Sensible heat flux	W
Q_R	Radiative heat flux	W
R_d	Complementary downwelling sky radiance	$Wsr^{-1}m^{-2}$
R_u	Upwelling sea radiance	$Wsr^{-1}m^{-2}$
$T_r(z)$	Solar transmission function	-
$a_{CDOM}(\lambda)$	CDOM absorption coefficient	m^{-1}

$a_{NAP}(\lambda)$	NAP absorption coefficient	m^{-1}
$a_{ph}(\lambda)$	Phytoplankton absorption coefficient	m^{-1}
$a_w(\lambda)$	Water absorption coefficient	m^{-1}
c_p	Specific heat of seawater	W s kg^{-1} °C^{-1}
k_b	Attenuation coefficients of particulates with blue/green colors	m^{-1}
k_r	Attenuation coefficients of particulates with red/yellow colors	m^{-1}
u_*	Friction velocity	m s^{-1}
$\alpha_a(\lambda)$	Sea-surface albedo	-
ρ_a	Air density	Kg m^{-3}
ΔT	Air-sea difference of temperature	°C
Δq	Specific humidity	-
∇T	Gradient of temperature	°C m^{-1}
e	Emissivity of the sea surface	-
h	Mixed-layer depth	m
Q	Net heat flux through the sea surface	W
RHR(z)	Radiant heat rate	°C s^{-1}
U	Wind speed above the air-sea interface	m s^{-1}

Z	Depth	m
α	thermal expansion coefficient of seawater	$°C^{-1}$
$a(\lambda)$	Total absorption coefficient	m^{-1}

CHAPTER 5

5. GENERAL CONCLUSION

5.1 CONCLUSIONS

The general objective of this thesis was to propose new remote sensing parameterizations for estimation the concentration of SPM in surface waters of the SLE (chapter 2). Also, the intention was to investigate to investigate the response of optically-derived C_{SPM} to different particle assemblages in terms of chemical composition and size distribution (chapter 3). A final motivation of this thesis was to review the role of SPM on heat budgets of littoral waters (chapter 4). In the introduction, fundamental concepts in marine optics are summarized. Also as part of this chapter, the study area, sampling protocols, and remote sensing models are described.

In the second chapter, a remote sensing model was originally proposed estimating the concentration of SPM in surface waters of the SLE and the Saguenay Fjord. Unlike previous algorithms, the parameterization evaluated here included optical information in the near-IR range to minimize the interference of strongly-light absorbing components in the blue spectral region. The MERIS-derived model for estimating C_{SPM} may be applied to other SLE-like environments having comparable optical properties and water turbidities. The suggested remote sensing approach will be also useful in future spaceborne missions such as Sentinel-3, a sensor having compatibility with MERIS spectral bands. An important result in chapter 2 was The sensitivity of MERIS bands 7 and 9 to changes on particle chemical composition

measurements. This effect was observed in situ and later confirmed based on synthetic remote sensing spectra obtained from radiative transfer model simulations.

In the third chapter, relationships between inherent optical properties of SPM and two particle second-order attributes (size distribution and chemical composition) showed the greater importance of particle dimensions for determining the variability of SPM scattering properties. Conversely, it was found that changes on refractive index of SPM, as inferred from the mineral content of particulates, was critical for explaining variations on particle absorption properties.

In the fourth chapter, the effects of suspended and dissolved particulates on the distribution of heat fluxes in turbid waters and the associated climate feedbacks were reviewed. Indeed, climate is expected to increase precipitation and turbidity plumes in the SLE, which will cause a redistribution of heat fluxes along the estuary since runoff will be mainly occurring in the lower estuary. Conversely, we could illustrate that how the immersion of particles in the variation of heat flux at the water surface can participate in altering weather conditions in a region. Besides particles, we discussed the comparable role of CDOM in light absorption within UV-blue wavelength compared to suspended particles, and the contribution of CDOM in radiant heat flux. In the SLE, CDOM is provided by several rivers and tributaries along the estuary, majorly the St. Lawrence River and the Saguenay Fjord.

5.2 PERSPECTIVES

An important research topic to address in the future is the influence of subpixel variability on satellite-derived C_{SPM} estimates. The SLE is a very dynamic environment that is characterized by a large spatial and temporal variability of SPM. Thus, a better sampling strategy should use continuous measurements of SPM-related variables (e.g., turbidity,

backscattering) over the satellite footprint. In order to minimize errors on satellite retrievals of C_{SPM}, an important effort should be focused in improving the mineral composition of SPM, a critical factor for obtaining accurate weight measurements. Lastly, this can be done by using multiple instruments such as Coulter Counter and LISST.

Accurate determinations of particle composition and size, and the associated inherent optical properties can help to understand how different suspended particles participate in the variation of radiant heat transfer through the absorbing of incident light. This information helps us to better understand relationships between different particle assemblages, heat fluxes and associated water temperature changes. These particle-mediated changes on water temperature can be assimilated into weather models for evaluating the impact of SPM on meteorological parameters such as atmospheric vertical motion, potential vorticity, and cloud condensation level.

BIBLIOGRAPHIC REFERENCES

Aas E., 1996, Refractive index of phytoplankton derived from its metabolite composition, Journal of Plankton Research, 18, 12, pp. 2223-2249.

Ackleson, S.G., Balch, W.M., Holligan, P.M., 1994. Response of water-leaving radiance to particulate calcite and chlorophyll *a* concentrations: A model for Gulf of Maine coccolithophore blooms. Journal of Geophysical Research. Oceans 99, 7483–7499. doi:10.1029/93JC02150

Adler, G., Koop, T., Haspel, C., Taraniuk, I., Moise, T., Koren, I., Heiblum, R.H., Rudich, Y., 2013. Formation of highly porous aerosol particles by atmospheric freeze-drying in ice clouds. Proc. Natl. Acad. Sci. 110, 20414–20419. doi:10.1073/pnas.1317209110

Agrawal, Y.C., I.N. McCave, and J.B. Riley, 1991. "Laser diffraction size analysis," in Principles, methods and applications of particle size analysis, J.P.M. Syvitski, editor, Cambridge University Press, pp. 119-128.

Ahn , Y. H. 1990. Optical properties of biogenous and numerical particles in the ocean; application: Inversion of reflectance. Ph.D. thesis, University of Pierre et Marie Curie. QC/425/YB/1990 [in French].

Allen, C.D., Breshears, D.D., 1998. Drought-induced shift of a forest–woodland ecotone: Rapid landscape response to climate variation. Proceedings of National Academy of Sciences. 95, 14839–14842.

Aminot, A., and Chaussepied, M. 1983. Manuel des analyses chimiques en milieu marin. Brest: CNEXO.

Arancibia-Bulnes, C.A., Estrada, C.A., and Ruiz-Suárez, J.C. 2000. Solar absorptance and thermal emittance of cermets with large particles. Journal of Physics D: Applied Physics, 33: 2489.

Assani, A.A., Landais, D., Mesfioui, M., Matteau, M., 2010. Relationship between the Atlantic Multidecadal Oscillation index and variability of mean annual flows for catchments in the St. Lawrence watershed (Quebec, Canada) during the past century. Hydrological Research. 41, 115. doi:10.2166/nh.2010.055

Auclair, A.N.D., Lill, J.T., Revenga, C., 1996. The role of climate variability and global warming in the dieback of Northern Hardwoods. Water, Air, Soil Pollution. 91, 163–186. doi:10.1007/BF00666255

Babin, M., and Stramski, D. 2004. Variations in the mass-specific absorption coefficient of mineral particles suspended in water. Limnology and Oceanography, 49, 756–767.

Babin, M., Stramski D., Ferrari G.M., Claustre H., Bricaud A., Obolensky G., Hoepffner N., 2003. Variations in the light absorption coefficients of phytoplankton, nonalgal particles, and dissolved organic matter in coastal waters around Europe. Journal of Geophysical Research 108. doi:10.1029/2001JC000882

Babin, S.M., Carton, J.A., Dickey, T.D., Wiggert, J.D., 2004. Satellite evidence of hurricane-induced phytoplankton blooms in an oceanic desert. Journal of Geophysical Researches. 109, C03043. doi:10.1029/2003JC001938

Balch, W.M., Vaughn, J.M., Novotny, J.F., Drapeau, D.T., Goes, J.I., Booth, E., Lapierre, J.M., Vining, C.L., Ashe, A., 2002. Fundamental changes in light scattering associated with infection of marine bacteria by bacteriophage. Limnology and Oceanography 47, 1554–1561.

Bernatchez, P., Dubois, J.-M.M., 2004. Bilan des connaissances de la dynamique de l'érosion des côtes du Québec maritime laurentien. Géographie physique et Quaternaire 58, 45. doi:10.7202/013110ar

Bhadha, J.H., Lang, T.A., and Daroub, S.H. 2017. Influence of suspended particulates on phosphorus loading exported from farm drainage during a storm event in the Everglades Agricultural Area. Journal of Soils and Sediments, 17: 240–252. doi:10.1007/s11368-016-1548-5.

Blanc, T.V., 1985. Variation of Bulk-Derived Surface Flux, Stability, and Roughness Results Due to the Use of Different Transfer Coefficient Schemes. Journal of Physical Oceanography 15, 650–669. doi:10.1175/1520-0485(1985)015<0650:VOBDSF>2.0.CO;2

Boss, E., Taylor, L., Gilbert, S., Gundersen, K., Hawley, N., Janzen, C., Johengen, T., Purcell, H., Robertson, C., Schar, D.W., 2009. Comparison of inherent optical properties as a surrogate for particulate matter concentration in coastal waters. Limnology and Oceanography. Methods 7, 803–810.

Bourgault, D., Kelley, D.E., and Galbraith, P.S. 2005. Interfacial solitary wave run-up in the St. Lawrence Estuary. Journal of Marine Research, 63: 1001–1015.

Bourgault, D., Morsilli, M., Richards, C., Neumeier, U., and Kelley, D.E. 2014. Sediment resuspension and nepheloid layers induced by long internal solitary waves shoaling orthogonally on uniform slopes. Continental Shelf Research, 72: 21–33. doi:10.1016/j.csr.2013.10.019.

Bourgault, D., Saucier, F.J., and Lin, C.A. 2001. Shear instability in the St. Lawrence Estuary, Canada: A comparison of fine-scale observations and estuarine circulation

model results. Journal of Geophysical Research: Oceans, 106: 9393–9409. doi:10.1029/2000JC900165.

Bowers, D.G. 2003. A simple turbulent energy-based model of fine suspended sediments in the Irish Sea. Continental Shelf Research, 23: 1495–1505. doi:10.1016/j.csr.2003.08.006.

Bowers, D.G., Binding, C.E., 2006. The optical properties of mineral suspended particles: A review and synthesis. Estuarine, Coastal and Shelf Science 67, 219–230. doi:10.1016/j.ecss.2005.11.010

Bowers, D.G., Braithwaite, K.M., Nimmo-Smith, W.A.M., Graham, G.W., 2009. Light scattering by particles suspended in the sea: The role of particle size and density. Continental Shelf Research 29, 1748–1755. doi:10.1016/j.csr.2009.06.004

Branch, R., Jessup, A.T., Minnett, P.J., Key, E.L., 2008. Comparisons of shipboard infrared sea surface skin temperature measurements from the CIRIMS and the M-AERI. Journal of Atmospheric and Oceanic Technology 25, 598–606. doi:10.1175/2007JTECHO480.1

Bricaud, A., Morel, A., and Prieur, L. 1981. Absorption by dissolved organic matter of the sea (yellow substance) in the UV and visible domains. Limnology and oceanography, 26: 43–53.

Bricaud, A., Morel, A., Babin, M., Allali, K., Claustre, H., 1998. Variations of light absorption by suspended particles with chlorophyll a concentration in oceanic (case 1) waters: Analysis and implications for bio-optical models. Journal of Geophysical Research. 103, 31033–31044. doi:10.1029/98JC02712

Brodie, I.M., Dunn, P.K., 2010. Commonality of rainfall variables influencing suspended solids concentrations in storm runoff from three different urban impervious surfaces. Journal of Hydrology. 387, 202–211. doi:10.1016/j.jhydrol.2010.04.008

Bukata, R.P., Jerome, J.H., Bruton, J.E., Jain, S.C., and Zwick, H.H. 1981. Optical water quality model of Lake Ontario. 1. Determination of the optical cross sections of organic and inorganic particulates in Lake Ontario. Applied Optics, 20, 1696–1703.

Carder, K.L., Chen, F.R., Cannizzaro, J.P., Campbell, J.W., Mitchell, B.G., 2004. Performance of the MODIS semi-analytical ocean color algorithm for chlorophyll-a. Advances in Space Research, 33, 1152–1159. doi:10.1016/S0273-1177(03)00365-X

Castro, R., Lavin, M.F., Ripa, P., 1994. Seasonal heat balance in the Gulf of California. Journal of Geophysical Research 99, 3249–3261.

Cayan, D.R., 1992. Latent and sensible heat flux anomalies over the northern oceans: Driving the sea surface temperature. American Meteorological Society 22, 859–881.

Cess, R.D., Potter, G.L., Blanchet, J.P., Boer, G.J., Ghan, S.J., Kiehl, J.T., Treut, H.L., Li, Z.-X., Liang, X.-Z., Mitchell, J.F.B., Morcrette, J.-J., Randall, D.A., Riches, M.R., Roeckner, E., Schlese, U., Slingo, A., Taylor, K.E., Washington, W.M., Wetherald, R.T., Yagai, I., 1989. Interpretation of Cloud-Climate Feedback as Produced by 14 Atmospheric General Circulation Models. Science 245, 513–516. doi:10.1126/science.245.4917.513

Chang, G.C., Dickey, T.D., 2004. Coastal ocean optical influences on solar transmission and radiant heating rate. Journal of Geophysical Research, Oceans 109, C01020. doi:10.1029/2003JC001821

Chanut, J.P., Poulet, S.A., 1979. Distribution des spectres de taille des particules en suspension dans le fjord du Saguenay. Canadian Journal of Earth Sciences 16, 240–249.

Çizmeli, S.A. 2002. Propriétés optiques intrinsèques et apparentes des eaux du golfe et de l'estuaire du Saint-Laurent: concordance optique, paramétrisation et variabilité spatio-temporelle, PhD. Thesis, Université de Sherbrooke, Sherbrooke, Canada, 156 pp, 2008.

Corlett, G.K., Barton, I.J., Donlon, C.J., Edwards, M.C., Good, S.A., Horrocks, L.A., Llewellyn-Jones, D.T., Merchant, C.J., Minnett, P.J., Nightingale, T.J., Noyes, E.J., O'Carroll, A.G., Remedios, J.J., Robinson, I.S., Saunders, R.W., Watts, J.G., 2006. The accuracy of SST retrievals from AATSR: An initial assessment through geophysical validation against in situ radiometers, buoys and other SST data sets. Journal of Advanced Space Research, Natural Hazards and Oceanographic Processes from Satellite Data 37, 764–769. doi:10.1016/j.asr.2005.09.037

Coulombier, T., Neumeier, U., and Bernatchez, P. 2012a. Sediment transport in a cold climate salt marsh (St. Lawrence Estuary, Canada), the importance of vegetation and waves. Estuarine, Coastal and Shelf Science, 101: 64–75. doi:10.1016/j.ecss.2012.02.014.

Coulombier, T., Neumeier, U., and Bernatchez, P. 2012b. Sediment transport in a cold climate salt marsh (St. Lawrence Estuary, Canada), the importance of vegetation and waves. Estuarine, Coastal and Shelf Science, 101: 64–75. doi:10.1016/j.ecss.2012.02.014.

d'Anglejan, B.F., Smith, E.C., 1973. Distribution, transport, and composition of suspended matter in the St. Lawrence estuary. Canadian Journal of Earth Sciences 10, 1380–1396.

Dickey, T.D., Falkowsky, P.G., 2002. Solar energy and its biological-physical interactions in the sea. Interscience Publications, New York.

Dickson, R., Lazier, J., Meincke, J., Rhines, P., Swift, J., 1996. Long-term coordinated changes in the convective activity of the North Atlantic. Progress in Oceanography 38, 241–295.

Djoumna, G., Lamb, K.G., Rao, Y.R., 2014. Sensitivity of the Parameterizations of Vertical Mixing and Radiative Heat Fluxes on the Seasonal Evolution of the Thermal Structure of Lake Erie. Atmosphere-Ocean 52, 294–313. doi:10.1080/07055900.2014.939824

Dong, Y., Rosenbaum, R.K., and Hauschild, M.Z. 2016. Assessment of Metal Toxicity in Marine Ecosystems: Comparative Toxicity Potentials for Nine Cationic Metals in Coastal Seawater. Environmental Science & Technology, 50, 269–278. doi:10.1021/acs.est.5b01625.

Dogliotti, A.I., Ruddick, K.G., Nechad, B., Doxaran, D., Knaeps, E., 2015. A single algorithm to retrieve turbidity from remotely-sensed data in all coastal and estuarine waters. Remote Sensing of Environment 156, 157–168. doi:10.1016/j.rse.2014.09.020

Donlon, C.J., Minnett, P.J., Gentemann, C., Nightingale, T.J., Barton, I.J., Ward, B., Murray, M.J., 2002. Toward Improved Validation of Satellite Sea Surface Skin Temperature Measurements for Climate Research. Journal of Climate 15, 353–369. doi:10.1175/1520-0442(2002)015<0353:TIVOSS>2.0.CO;2

Donohoe, A., Frierson, D.M.W., Battisti, D.S., 2013. The effect of ocean mixed layer depth on climate in slab ocean aquaplanet experiments. Climate Dynamics 43, 1041–1055. doi:1007/s00382-013-1843-4

Doxaran, D., Ehn, J., Belanger, S., Matsuoka, A., Hooker, S., and Babin, M. 2012. Optical characterization of suspended particles in the Mackenzie River Plume (Canadian Arctic Ocean) and implications for ocean colour remote sensing. Biogeosciences, 9. 3213-3229.

Doxaran, D., Froidefond, J., Castaing, P., 2002. A reflectance band ratio used to estimate suspended matter concentrations in sediment-dominated coastal waters. International Journal of Remote Sensing 23, 5079–5085.

Doxaran, D., Froidefond, J.-M., and Castaing, P. 2003. Remote-sensing reflectance of turbid sediment-dominated waters. Reduction of sediment type variations and changing illumination conditions effects by use of reflectance ratios. Applied Optics, 42: 2623–2634.

Doxaran, D., Froidefond, J.-M., Castaing, P., Babin, M., 2009. Dynamics of the turbidity maximum zone in a macrotidal estuary (the Gironde, France): Observations from field and MODIS satellite data. Estuarine, Coastal and Shelf Science 81, 321–332. doi:10.1016/j.ecss.2008.11.013

Doxaran, D., Froidefond, J.-M., Lavender, S., and Castaing, P. 2002. Spectral signature of highly turbid waters: Application with SPOT data to quantify suspended particulate matter concentrations. Remote Sensing Environment, 81, 149–161. doi:10.1016/S0034-4257(01)00341-8.

Dunton, K.H., Schonberg, S.V., and Cooper, L.W. 2012. Food Web Structure of the Alaskan Nearshore Shelf and Estuarine Lagoons of the Beaufort Sea. Estuaries and Coasts, 35, 416–435. doi:10.1007/s12237-012-9475-1.

D'Sa, E.J., Miller, R.L., and McKee, B.A. 2007. Suspended particulate matter dynamics in coastal waters from ocean color: Application to the northern Gulf of Mexico:

Suspended particulate matter dynamics. Geophysical Research Letters, 34, doi:10.1029/2007GL031192.

El-Sabh, M.I., and Silverberg, N. 1990. The St. Lawrence Estuary: Introduction. In Oceanography of a Large-Scale Estuarine System. Edited by M.I. El-Sabh and N. Silverberg. Springer-Verlag. pp. 1–9. doi:10.1002/9781118663783.ch1.

El-Sabh, M.I., and Silverberg, N. 1992. The St. Lawrence Estuary: Introduction. In Oceanography of a Large-Scale Estuarine System. Edited by M.I. El-Sabh and N. Silverberg. Springer-Verlag. pp. 1–9.

Estapa, M.L., Boss, E., Mayer, L.M., Roesler, C.S., 2012. Role of iron and organic carbon in mass-specific light absorption by particulate matter from Louisiana coastal waters. Limnology and Oceanography. 57, 97–112. doi:10.4319/lo.2012.57.1.0097

Fauchot, J., Saucier, F.J., Levasseur, M., Roy, S., Zakardjian, B., 2008. Wind-driven river plume dynamics and toxic Alexandrium tamarense blooms in the St. Lawrence estuary (Canada): A modeling study. Harmful Algae 7, 214–227. doi:10.1016/j.hal.2007.08.002

Feng, L., Li, J., 2006. A comparison of latent heat fluxes over global oceans for ERA and NCEP with GSSTF2. Geophysical Research Letters 33. doi:10.1029/2005GL024677

Fettweis, M., Monbaliu, J.; Baeye, M., Nechad, B., and Van den Eynde, D.2012. Weather and climate induced spatial variability of surface suspended particulate matter concentration in the North Sea and the English Channel. Methods in Oceanography, 3–4, 25–39

Fleming, S.W., Dahlke, H.E., 2014. Parabolic northern-hemisphere river flow teleconnections to El Niño-Southern Oscillation and the Arctic Oscillation. Environmental Research Letters. 9, 104007. doi:10.1088/1748-9326/9/10/104007

Forrester, W.D. 1970. Geostrophic approximation in the St. Lawrence estuary. Tellus, 22: 53–65. doi:10.1111/j.2153-3490.1970.tb01936.x.

Froidefond, J., Lahet, F., Hu, C., Doxaran, D., Guiral, D., Prost, M., and Ternon, J.-F. 2004. Mudflats and mud suspension observed from satellite data in French Guiana. Marine Geology, 208, 153–168.

Fusco, L., Muirhead, K., Tobiss, G., 1989. Earthnet's coordination scheme for AVHRR data. International Journal of Remote Sensing 10, 625–636. doi:10.1080/01431168908903903

Gagné, H., Lajeunesse, P., St-Onge, G., Bolduc, A., 2009. Recent transfer of coastal sediments to the Laurentian Channel, Lower St. Lawrence Estuary (Eastern Canada), through submarine canyon and fan systems. Geo-Marine Letters 29, 191–200. doi:10.1007/s00367-009-0138-6

Garcia, R.D., Reissig, M., Queimaliños, C.P., Garcia, P.E., and Dieguez, M.C. 2015. Climate-driven terrestrial inputs in ultraoligotrophic mountain streams of Andean Patagonia revealed through chromophoric and fluorescent dissolved organic matter. Science of The Total Environment, 521–522: 280–292. doi:10.1016/j.scitotenv.2015.03.102.

Gentemann, C.L., 2014. Three way validation of MODIS and AMSR-E sea surface temperatures. Journal of Geophysical Research, Oceans 119, 2583–2598. doi:10.1002/2013JC009716

Gernez, P., Barillé, L.; Lerouxel, A., Mazeran, C., Lucas, A., and Doxaran, D. 2014. Remote sensing of suspended particulate matter in turbid oyster-farming ecosystems. Journal of Geophysical Research, 119, 7277-7294.

Ghate, V.P., Albrecht, B.A., Fairall, C.W., Weller, R.A., 2009. Climatology of Surface Meteorology, Surface Fluxes, Cloud Fraction, and Radiative Forcing over the Southeast Pacific from Buoy Observations. Journal of Climate 22, 5527–5540. doi:10.1175/2009JCLI2961.1

Gildor, H., 2003. A role for ocean biota in tropical intraseasonal atmospheric variability. Geophysical Research Letters 30. doi:10.1029/2002GL016759

Gilerson, A. a., Gitelson, A.A., Zhou, J., Gurlin, D., Moses, W.J., Ioannou, I., and Ahmed, S.A. 2010. Algorithms for remote estimation of chlorophyll-a in coastal and inland waters using red and near infrared bands. Papers in Natural Resources,. doi:10.1029/2005GL022917.

Gitelson, A.A., Dall'Olmo, G., Moses, W., Rundquist, D.C., Barrow, T., Fisher, T.R., Gurlin, D., Holz, J., 2008. A simple semi-analytical model for remote estimation of chlorophyll-a in turbid waters: Validation. Remote Sensing of Environment 112, 3582–3593. doi:10.1016/j.rse.2008.04.015

Gobeil, C., Sundby, B., and Silverberg, N. 1981. Factors influencing particulate matter geochemistry in the St. Lawrence estuary turbidity maximum. Marine Chemistry, 10: 123–140.

Gordon, C., Cooper, C., Senior, C.A., Banks, H., Gregory, J.M., Johns, T.C., Mitchell, J.F.B., Wood, R.A., 2000. The simulation of SST, sea ice extents and ocean heat transports in a version of the Hadley Centre coupled model without flux adjustments. Climate Dynamics. 16, 147–168. doi:10.1007/s003820050010

Gordon, H.R. 1997. Atmospheric correction of ocean color imagery in the Earth Observing System era. Journal of Geophysical Research: Atmospheres, 102: 17081–17106. doi:10.1029/96JD02443.

Gordon, H.R., and Castaño, D.J. 1987. Coastal Zone Color Scanner atmospheric correction algorithm: multiple scattering effects. Applied optics, 26: 2111–2122.

Gouirand, I., Moron, V., 2003. Variability of the impact of El Niño–southern oscillation on sea-level pressure anomalies over the North Atlantic in January to March (1874–1996). International Journal of Climatology. 23, 1549–1566. doi:10.1002/joc.963

Guézennec, L., Lafite, R., Dupont, J.-P., Meyer, R., Boust, D., 1999. Hydrodynamics of suspended particulate matter in the tidal freshwater zone of a macrotidal estuary (the Seine Estuary, France). Estuaries 22, 717–727. doi:10.2307/1353058

Handorf, D., Jaiser, R., Dethloff, K., Rinke, A., Cohen, J., 2015. Impacts of Arctic sea ice and continental snow cover changes on atmospheric winter teleconnections. Geophysical Research Letters. 42, 2015GL063203. doi:10.1002/2015GL063203

Hardman-Mountford, N.J., Polimene, L., Hirata, T., Brewin, R.J.W., Aiken, J., 2013. Impacts of light shading and nutrient enrichment geo-engineering approaches on the productivity of a stratified, oligotrophic ocean ecosystem. Journal of Royal Society. Interface 10, 20130701. doi:10.1098/rsif.2013.0701

Hátún, H., Payne, M.R., Beaugrand, G., Reid, P.C., Sandø, A.B., Drange, H., Hansen, B., Jacobsen, J.A., Bloch, D., 2009. Large bio-geographical shifts in the north-eastern Atlantic Ocean: From the subpolar gyre, via plankton, to blue whiting and pilot whales. Progress in Oceanography. 80, 149–162. doi:10.1016/j.pocean.2009.03.001

Helbling, E.W., Gao, K.S., Goncalves, R.J., Wu, H.Y., Villafane, V.E., 2003. Utilization of solar UV radiation by coastal phytoplankton assemblages off SE China when exposed

to fast mixing. Marine Ecology Progress Series. 259, 59–66. doi:10.3354/meps259059

Hessen, D.O., Carroll, J., Kjeldstad, B., Korosov, A.A., Pettersson, L.H., Pozdnyakov, D., Sørensen, K., 2010. Input of organic carbon as determinant of nutrient fluxes, light climate and productivity in the Ob and Yenisey estuaries. Estuarine, Coastal and Shelf Science. 88, 53–62. doi:10.1016/j.ecss.2010.03.006

Hill, V.J., 2008. Impacts of chromophoric dissolved organic material on surface ocean heating in the Chukchi Sea. Journal of Geophysical Research. 113. doi:10.1029/2007JC004119

Holland, M.M., Bailey, D.A., Briegleb, B.P., Light, B., Hunke, E., 2011. Improved Sea Ice Shortwave Radiation Physics in CCSM4: The Impact of Melt Ponds and Aerosols on Arctic Sea Ice Journal of Climate. 25, 1413–1430. doi:10.1175/JCLI-D-11-00078.1

Huang, C.-C., Li, Y.-M., Wang, Q., Sun, D.-Y., Le, C.-F., and Shi, K. 2012. Scattering spectrum properties and their relationship to biogeochemical parameters: a case study in Taihu Lake. Limnology, 13: 1–11. doi:10.1007/s10201-011-0346-4.

Hurrell, J.W., Loon, H.V., 1997. Decadal variationsin climate associated with the North Atlantic Oscillation. Climate Change 36, 301–326. doi:10.1023/A:1005314315270

Hwang, S.-W., Seo, D.-I., Yoon, J.-D., Kim, J.-H., Park, S.-H., Jang, M.-H., and Chang, K.-H. 2017. Changes in particulate organic matters and plankton populations in nature-like fishways: role of nature-like fish ways in water treatment. Knowledge & Management of Aquatic Ecosystems,: 2. doi:10.1051/kmae/2016034.

Isobe, A., Kako, S., and Iwasaki, S. 2014. Synoptic-Scale Atmospheric Motions Modulated by Spring Phytoplankton Bloom in the Sea of Japan. Journal of Climate, 27: 7587–7602. doi:10.1175/JCLI-D-14-00277.1.

Jacobi, J., Schneider, M., Bottazzi, P., Pillco, M., Calizaya, P., Rist, S., 2015. Agroecosystem resilience and farmers' perceptions of climate change impacts on cocoa farms in Alto Beni, Bolivia. Renewable Agriculture and Food Systems. 30, 170–183. doi:10.1017/S174217051300029X

Jessup, A.T., Branch, R., 2008. Integrated Ocean Skin and Bulk Temperature Measurements Using the Calibrated Infrared In Situ Measurement System (CIRIMS) and Through-Hull Ports. Journal of Atmospheric and Oceanic Technology. 25, 579–597. doi:10.1175/2007JTECH0479.1

Jiang, C., Zhang, L., 2015. Climate Change and Its Impact on the Eco-Environment of the Three-Rivers Headwater Region on the Tibetan Plateau, China. International Journal of Environmental Research. Public. Health 12, 12057–12081. doi:10.3390/ijerph121012057

Jolliff, J.K., Smith, T.A., 2014. Biological modulation of upper ocean physics: Simulating the biothermal feedback effect in Monterey Bay, California: Biothermal Feedback. Journal of Geophysical Research. Biogeosciences 119, 703–721. doi:10.1002/2013JG002522

Jolliff, J.K., Smith, T.A., Barron, C.N., deRada, S., Anderson, S.C., Gould, R.W., Arnone, R.A., 2012. The impact of coastal phytoplankton blooms on ocean-atmosphere thermal energy exchange: Evidence from a two-way coupled numerical modeling system. Geophysical Research Letters. 39, L24607. doi:10.1029/2012GL053634.

Junge, C. E., 1963, Air Chemistry and Radioactivity, Academic, New York.

Kaefer, B.A., Anderson, D.M., 1993. Use of remotely-sensed surface temperatures in studies of Alexandrium Tamarense bloom dynamics. Elsevier. V, 763–768.

Kahru, 1993. Cyanobacterial Blooms Cause Heating of the Sea-Surface. Marine Ecology Progress Series. 101, 1–7. doi:10.3354/meps101001

Kako A. and Kubota M., 2009. Numerical studies on the variability of mixed layer temperature in the North Pacific, Journal of Physical Oceanography, 39, DOI: 10.1175/2008JPO3979.1

Kalnay, E., and Coauthors, 1996. The NCEP/NCAR 40-Year Reanalysis Project. Bulletin of American Meteorological Society, 77, 437–471, doi:10.1175/1520-0477(1996)077,0437:TNYRP.2.0.CO;2.

Kazil, J., Feingold, G., Wang, H., Yamaguchi, T., 2014. On the interaction between marine boundary layer cellular cloudiness and surface heat fluxes. Atmospheric Chemistry and Physics. 14, 61–79. doi:10.5194/acp-14-61-2014

Kearns, E.J., Hanafin, J.A., Evans, R.H., Minnett, P.J., Brown, O.B., 2000. An Independent Assessment of Pathfinder AVHRR Sea Surface Temperature Accuracy Using the Marine Atmosphere Emitted Radiance Interferometer (MAERI). Bulletin of American Meteorological Society. 81, 1525–1536. doi:10.1175/1520-0477(2000)081<1525:AIAOPA>2.3.CO;2

Kirk, J.T.O., 1988. Solar heating of water bodies as influenced by their inherent optical properties. Journal of Geophysical Research. Atmospheres 93, 10897–10908. doi:10.1029/JD093iD09p10897

Kirk, J.T.O., 1994. Light and photosynthesis in aquatic ecosystems. 2nd ed. 3rd, 80-85, Cambridge University Press.

Komori, S., Kurose, R., Takagaki, N., Ohtsubo, S., Iwano, K., Handa, K., Shimada, S., 2011. Sensible and latent heat transfer across the air-water interface in wind-driven turbulence. Kyoto University Press, Gas Transfers at Water Surfaces 2010, 78–89.

Komori, S., Nagaosa, R., Murakami, Y., 1993. Turbulence Structure and Heat and Mass Transfer Mechanism at a Gas-Liquid Interface in a Wind-Wave Tunnel, in: Nieuwstadt, F.T.M. (Ed.), Advances in Turbulence IV, Fluid Mechanics and Its Applications. Springer Netherlands, pp. 423–427.

Kondo, J., 1975. Air–sea bulk transfer coefficients in diabatic conditions. Boundary-Layer Meteorology, 9, 91–112, doi:10.1007/BF00232256

Kostadinov, T.S., Siegel, D.A., and Maritorena, S. 2009. Retrieval of the particle size distribution from satellite ocean color observations. Journal of Geophysical Research, 114. doi:10.1029/2009JC005303.

Koutitonsky, V.G., and Bugden, G.L. 1989, March 14. The Physical oceanography of the Gulf of st. Lawrence: A Review with Emphasis on the Synoptic Variability of the Motion. Proceeding, Maurice Lamintagne Institute, Mont-Joli, Quebec.

Krüger, O., Graßl, H., 2011. Southern Ocean phytoplankton increases cloud albedo and reduces precipitation. Geophysical Research Letters. 38, L08809. doi:10.1029/2011GL047116

Kubota, M., Kano, A., Muramatsu, H., Tomita, H., 2003. Intercomparison of Various Surface Latent Heat Flux Fields. Journal of Climate. 16, 670–678. doi:10.1175/1520-0442(2003)016<0670:IOVSLH>2.0.CO;2

Langhans, W., Schmidli, J., Fuhrer, O., Bieri, S., Schar, C., 2013. Long-Term Simulations of Thermally Driven Flows and Orographic Convection at Convection-Parameterizing and Cloud-Resolving Resolutions. Journal of Applied Meteorology and Climatology. 52, 1490–1510. doi:10.1175/JAMC-D-12-0167.1

Lapierre, J., Frenette, J., 2008. Advection of freshwater phytoplankton in the St. Lawrence River estuarine turbidity maximum as revealed by sulfur-stable isotopes. Marine Ecology Progress Series. 372, 19–29. doi:10.3354/meps07685

Larouche, P., Boyer-Villemaire, U., 2010. Suspended particulate matter in the St. Lawrence estuary and Gulf surface layer and development of a remote sensing algorithm. Estuarine, Coastal and Shelf Science 90, 241–249. doi:10.1016/j.ecss.2010.09.005

Lavin, M.F., Organista, S., 1988. Surface heat flux in the northern Gulf of California. Journal of Geophysical Research. Oceans 93, 14033–14038. doi:10.1029/JC093iC11p14033

Lawrence, D.M., Slater, A.G., 2005. A projection of severe near-surface permafrost degradation during the 21st century. Geophysical Research Letters, 32, L24401. doi:10.1029/2005GL025080

Lee, Z. P., Lubac, B., Werdell, J., and Arnone, R. 2009. An update of the quasi-analytical algorithm (QAA_v5). IOCCG software report, 2009.

Levasseur, M., Therriault, J.-C., Legendre, L., 1984, Hierarchical control of phytoplankton succession by physical factors, Marine Ecology Progress Series, 19, 211-222

Levenberg, K. 1944. A method for the solution of certain problems in least squares, Quarterly Journal of Applied Mathematics, 1944, 2, pp. 164–168.

Lewis, M.R., Cullen, J.J., Platt, T., 1983. Phytoplankton and thermal structure in the upper ocean: Consequences of nonuniformity in chlorophyll profile. Journal of Geophysical Research. 88, 2565. doi:10.1029/JC088iC04p02565

Loisel, H., Nicolas, J.-M., Sciandra, A., Stramski, D., Poteau, A., 2006. Spectral dependency of optical backscattering by marine particles from satellite remote sensing of the

global ocean. Journal of Geophysical Researches. 111, C09024. doi:10.1029/2005JC003367

Loisel H., Duforet L., Dessailly D., Chami M., Dubuisson P., 2008, Investigation of the variations in the water leaving polarized reflectance from the POLDER satellite data over two biogeochemical contrasted oceanic areas, Optics Express, 16, 17, 12905-12915.

Lombardi, M.A., Hanson, W., 2005. The GOES time code service, 1974-2004: a retrospective. Journal of National Institute of Standards and Technology. 110, 79.

Löptien, U., Meier, H.E.M., 2011. The influence of increasing water turbidity on the sea surface temperature in the Baltic Sea: A model sensitivity study. Journal of Marine Systems 88, 323–331. doi:10.1016/j.jmarsys.2011.06.001

Lucotte, M., and d' Anglejan, B. 1986. Seasonal control of the Saint-Lawrence maximum turbidity zone by tidal-flat sedimentation. Estuaries, 9, 84–94.

Ludwig, P., Pinto, J.G., Reyers, M., Gray, S.L., 2014. The role of anomalous SST and surface fluxes over the southeastern North Atlantic in the explosive development of windstorm Xynthia. Q. Journal of Royal Meteorological Society. 140, 1729–1741. doi:10.1002/qj.2253

Lyapustin, A.I., and Kaufman, Y.J. 2001. Role of adjacency effect in the remote sensing of aerosol. Journal of Geophysical Research: Atmospheres, 106: 11909–11916. doi:10.1029/2000JD900647.

Ma, L., Wang, F., Wang, C., Wang, C., and Tan, J. 2015. Monte Carlo simulation of spectral reflectance and BRDF of the bubble layer in the upper ocean. Optics Express, 23: 24274. doi:10.1364/OE.23.024274.

Manizza, M., Le Quéré, C., Watson, A.J., Buitenhuis, E.T., 2005. Bio-optical feedbacks among phytoplankton, upper ocean physics and sea-ice in a global model. Geophysical Research Letters. 32, L05603. doi:10.1029/2004GL020778

Martinez-Vicente, V., Dall'Olmo, G., Tarran, G., Boss, E., and Sathyendranath, S. 2013. Optical backscattering is correlated with phytoplankton carbon across the Atlantic Ocean. Geophysical Research Letters, 40: 1154–1158. doi:10.1002/grl.50252.

McCabe, G.J., Betancourt, J.L., Gray, S.T., Palecki, M.A., Hidalgo, H.G., 2008. Associations of multi-decadal sea-surface temperature variability with US drought. Quaternary international, The 22nd Pacific Climate Workshop 188, 31–40. doi:10.1016/j.quaint.2007.07.001

McCabe, G.J., Palecki, M.A., 2006. Multidecadal climate variability of global lands and oceans. International Journal of Climatology. 26, 849–865. doi:10.1002/joc.1289

McCabe, G.J., Wolock, D.M., 2014. Variability Common to Global Sea Surface Temperatures and Runoff in the Conterminous United States. Journal of Hydrometeorology. 15, 714–725. doi:10.1175/JHM-D-13-097.1

McCarthy, J.F., and Zachara, J.M. 1989. Subsurface transport of contaminants. Environmental science & technology, 23: 496–502.

McCoy, D.T., Burrows, S.M., Wood, R., Grosvenor, D.P., Elliott, S.M., Ma, P.-L., Rasch, P.J., Hartmann, D.L., 2015. Natural aerosols explain seasonal and spatial patterns of Southern Ocean cloud albedo. Science Advances. 1, e1500157. doi:10.1126/sciadv.1500157

Mechem, D.B., Yuter, S.E., de Szoeke, S.P., 2012. Thermodynamic and Aerosol Controls in Southeast Pacific Stratocumulus. Journal of Atmospheric Sciences. 69, 1250–1266. doi:10.1175/JAS-D-11-0165.1

Mei, Z.-P., Saucier, F.J., Le Fouest, V., Zakardjian, B., Sennville, S., Xie, H., Starr, M., 2010. Modeling the timing of spring phytoplankton bloom and biological production of the Gulf of St. Lawrence (Canada): Effects of colored dissolved organic matter and temperature. Continental Shelf Research. 30, 2027–2042. doi:10.1016/j.csr.2010.10.003

Meybeck, M., Laroche, L., Dürr, H.., and Syvitski, J.P.. 2003. Global variability of daily total suspended solids and their fluxes in rivers. Global and Planetary Change, 39: 65–93. doi:10.1016/S0921-8181(03)00018-3.

Miller, P.I., Shutler, J.D., Moore, G.F., and Groom, S.B. 2006. SeaWiFS discrimination of harmful algal bloom evolution. International Journal Remote Sensing, 27, 2287-2301.

Miller, R.L., McKee, B.A., 2004. Using MODIS Terra 250 m imagery to map concentrations of total suspended matter in coastal waters. Remote Sensing of Environment 93, 259–266. doi:10.1016/j.rse.2004.07.012

Millero, F.J., Perron, G., Desnoyers, J.E., 1973. Heat capacity of seawater solutions from 5° to 35°C and 0.5 to 22‰ chlorinity. Journal of Geophysical Research. 78, 4499–4507. doi:10.1029/JC078i021p04499

Minnett, P.J., Knuteson, R.O., Best, F.A., Osborne, B.J., Hanafin, J.A., Brown, O.B., 2001. The marine-atmospheric emitted radiance interferometer: A high-accuracy, seagoing infrared spectroradiometer. Journal of Atmospheric and Oceanic Technology. 18, 994–1013.

Mobley, C.D. 1994. Light and Water: Radiative Transfer in Natural Waters. Academic Press.

Modest, M.F. 2003. Chapter 22 - Inverse radiative heat transfer. In Radiative Heat Transfer (Second Edition). Academic Press, Burlington. pp. 729–742.

Mohammadpour, G., Montes-Hugo, M.A., Stavn, R., Gagné, J.-P., Larouche, P., 2015. Particle Composition Effects on MERIS-Derived SPM: A Case Study in the Saint Lawrence Estuary. Canadian Journal of Remote Sensing 41, 515–524. doi:10.1080/07038992.2015.1110012

Montes-Hugo, M., Roy, S., Gagné, J.P., Demers, S., Cizmeli, S., and Mas, S. 2012. Ocean colour and distribution of suspended particulates in the St. Lawrence estuary. EARSeL eProceedings, 11: 1.

Montes-Hugo, M.; and Mohammadpour, G. 2012. Biogeo-optical modeling of SPM in the St. Lawrence Estuary. Canadian Journal of Remote Sensing, 38, 197-209.

Montes-Hugo, M.A., Vernet, M., Martinson, D., Smith, R., Iannuzzi, R., 2008. Variability on phytoplankton size structure in the western Antarctic Peninsula (1997–2006). Deep Sea Research Part II: Topical Studies in Oceanography 55, 2106–2117. doi:10.1016/j.dsr2.2008.04.036

Morel, A. 1974. Optical properties of pure water and pure sea water, in Optical aspects of oceanography, edited by N.G. Jerlov, and Nielsen, E.S., pp. 1-24, Academic, New York, 1974.

Morel, A. 1988. Optical modeling of the upper ocean in relation to its biogenous matter content (case I waters). Journal of Geophysical Research: Oceans, 93: 10749–10768. doi:10.1029/JC093iC09p10749.

Morel, A., Antoine, D., 1994. Heating Rate within the Upper Ocean in Relation to its Bio–optical State. Journal of Physical Oceanography. 24, 1652–1665. doi:10.1175/1520-0485(1994)024<1652:HRWTUO>2.0.CO;2

Morel, A., Gentili, B., 1996. Diffuse reflectance of oceanic waters. III. Implication of bidirectionality for the remote-sensing problem. Applied Optics. 35, 4850–4862. doi:10.1364/AO.35.004850

Morel, A., Prieur, L., 1977. Analysis of variations in ocean color. Limnology and Oceanography 22, 709–722. doi:10.4319/lo.1977.22.4.0709

Mueller, J.L., Fargion, G.S., McClain, C.R., Brown, S.W., Clark, D.K., Johnson, B.C., Yoon, H., Lykke, K.R., and Flora, S.J., 2003. Ocean Optics Protocols For Satellite Ocean Color Sensor Validation, Revision 5, Volume VI: Special Topics in Ocean Optics Protocols, Part 2. NASA Tech Memo 211621.

Müller HW, Horn K., 1990. Some Technical Aspects of a High Quality UV/Vis Spectrometer for Routine Analysis, Applied UV Spectroscopy 19D, Bodenseewerk Perkin-Elmer GmbH, Überlingen,

Nakamoto, S., Kumar, S.P., Oberhuber, J.M., Ishizaka, J., Muneyama, K., Frouin, R., 2001. Response of the equatorial Pacific to chlorophyll pigment in a mixed layer isopycnal ocean general circulation model. Geophysical Research Letters. 28, 2021–2024. doi:10.1029/2000GL012494

Nechad, B., De Cauwer, V., Park, Y., and Ruddick, K.G. 2003. Suspended Particulate Matter (SPM) mapping from MERIS imagery. Calibration of a regional algorithm for the Belgian coastal waters. lQr, 1: 52–0.

Nechad, B., Ruddick K.G. and Park Y. 2009. Calibration and validation of a generic multisensor algorithm for mapping of total suspended matter in turbid waters. Remote Sensing of Environment, 114, 854-866.

Nelson, D.M., Smith Jr., W.O., 1986. Phytoplankton bloom dynamics of the western Ross Sea ice edge—II. Mesoscale cycling of nitrogen and silicon. Deep Sea Research. Part Oceanography. Res. Pap. 33, 1389–1412. doi:10.1016/0198-0149(86)90042-7

Neukermans, G., Loisel, H., Mériaux, X., Astoreca, R., McKee, D., 2012. In situ variability of mass-specific beam attenuation and backscattering of marine particles with respect to particle size, density, and composition. Limnology and oceanography 57.

Neukermans, G., Reynolds, R. A. Stramski, D., 2016. Optical classification and characterization of marine particle assemblages within the western Arctic Ocean. Limnology and Oceanography., 61: 1472–1494. doi:10.1002/lno.10316

Nieke, B., Reuter, R., Heuermann, R., Wang, H., Babin, M., Therriault, J.C. 1997. Light absorption and fluorescence properties of chromophoric dissolved organic matter (CDOM), in the St. Lawrence Estuary (Case 2 waters). Continental Shelf Research, 17: 235–252.

Nielsen, S.L., Sand-Jensen, K., Borum, J., Geertz-Hansen, O., 2002. Phytoplankton, nutrients, and transparency in Danish coastal waters. Estuaries 25, 930–937. doi:10.1007/BF02691341

O'Carroll, A.G., August, T., Le Borgne, P., Marsouin, A., 2012. The accuracy of SST retrievals from Metop-A IASI and AVHRR using the EUMETSAT OSI-SAF matchup dataset. Remote Sensing of Environment. 126, 184–194. doi:10.1016/j.rse.2012.08.006

Ohlmann, J.C., Siegel, D.A., Mobley, C.D., 2000a. Ocean Radiant Heating. Part I: Optical Influences. Journal of Physical Oceanography. 30, 1833–1848. doi:10.1175/1520-0485(2000)030<1833:ORHPIO>2.0.CO;2

Ohlmann, J.C., Siegel, D.A., 2000b. Ocean Radiant Heating. Part II: Parameterizing Solar Radiation Transmission through the Upper Ocean. Journal of Physical Oceanography. 30, 1849–1865. doi:10.1175/1520-0485(2000)030<1849:ORHPIP>2.0.CO;2

Ohlmann, J.C., Siegel, D.A., Washburn, L., 1998. Radiant heating of the western equatorial Pacific during TOGA-COARE. Journal of Geophysical Research. Oceans 103, 5379–5395. doi:10.1029/97JC03422

Organelli, E., Bricaud, A., Gentili, B., Antoine, D., and Vellucci, V. 2016. Retrieval of Colored Detrital Matter (CDM) light absorption coefficients in the Mediterranean Sea using field and satellite ocean color radiometry: Evaluation of bio-optical inversion models. Remote Sensing of Environment, 186: 297–310. doi:10.1016/j.rse.2016.08.028.

Oschlies, A., 2004. Feedbacks of biotically induced radiative heating on upper-ocean heat budget, circulation, and biological production in a coupled ecosystem-circulation model. Journal of Geophysical Research. Oceans 109, C12031. doi:10.1029/2004JC002430

Otterman, J., 1976. Climatic change by cloudiness linked to the spatial variability of sea surface temperatures. Journal of Franklin Institute. 302, 259–282. doi:10.1016/0016-0032(79)90128-5

Pan, X., Mannino, A., Russ, M.E., Hooker, S.B., Harding, L.W., 2010. Remote sensing of phytoplankton pigment distribution in the United States northeast coast. Remote Sensing of Environment. 114, 2403–2416. doi:10.1016/j.rse.2010.05.015

Pearson, R.K. 2005. Mining imperfect data. Dealing with contamination and incomplete records. Society for Industrial and Applied Mathematics, 305 p. doi.org/10.1137/1.9780898717884.

Pegau, W.S., 2002. Inherent optical properties of the central Arctic surface waters. Journal of Geophysical Research. Oceans 107, 8035. doi:10.1029/2000JC000382

Pegau, W.S., Gray, D., Zaneveld, J.R.V., 1997. Absorption and attenuation of visible and near-infrared light in water: dependence on temperature and salinity. Applied Optics. 36, 6035–6046. doi:10.1364/AO.36.006035

Peng, F., Effler, S.W., 2012. Mass-specific scattering coefficient for natural minerogenic particle populations: particle size distribution effect and closure analyses. Applied Optics 51, 2236. doi:10.1364/AO.51.002236

Pope, R.M., Fry, E.S., 1997. Absorption spectrum (380–700 nm) of pure water. II. Integrating cavity measurements. Applied optics 36, 8710–8723.

Poulet, S., Cossa, D., Marty, J.C., 1986. Combined analysis of the size spectra and biochemical composition of particles in the St. Lawrence Estuary. Marine Ecology Progress. Ser 30, 205–214.

Qiu, B., and Kelly, K.A. 1993. Upper-Ocean Heat Balance in the Kuroshio Extension Region. Journal of Physical Oceanography, 23: 2027–2041. doi:10.1175/1520-0485(1993)023<2027:UOHBIT>2.0.CO;2.

Reynolds, R. A., Stramski, D. and Neukermans, G., 2016, Optical backscattering by particles in Arctic seawater and relationships to particle mass concentration, size distribution, and bulk composition. Limnology and Oceanography 61: 1869–1890. doi:10.1002/lno.10341

Reynolds, R.A., Stramski, D., Wright, V.M., and Wozniak, S.B. 2010. Measurements and characterization of particle size distributions in coastal waters. Journal of Geophysical Research, 115, C08024, doi:10.1029/2009JC005930.

Reynolds, R.W., Rayner, N.A., Smith, T.M., Stokes, D.C., Wang, W., 2002. An improved in situ and satellite SST analysis for climate. Journal of Climate. 15, 1609–1625.

Rosenfeld, D., Kaufman, Y.J., Koren, I., 2006. Switching cloud cover and dynamical regimes from open to closed Benard cells in response to the suppression of precipitation by aerosols. Atmospheric Chemistry and Physics 6, 2503–2511. doi:10.5194/acp-6-2503-2006

Röttgers, R., Dupouy, C., Taylor, B.B., Bracher, A., Woźniak, S.B., 2014. Mass-specific light absorption coefficients of natural aquatic particles in the near-infrared spectral region. Limnology and Oceanography 59, 1449–1460. doi:10.4319/lo.2014.59.5.1449

Röttgers, R., McKee, D., and Woźniak, S.B. 2013. Evaluation of scatter corrections for ac-9 absorption measurements in coastal waters. Methods in Oceanography, 7: 21–39. doi:10.1016/j.mio.2013.11.001.

Ruddick, K., Nechad, B., Neukermans, G., Park, Y., Doxaran, D., Sirjacobs, D., and Beckers, J.-M. 2008. Remote sensing of suspended particulate matter in turbid waters: state of the art and future perspectives. In Proceedings of the Ocean Optics XIX conference, Barga. pp. 6–10.

Ruiz, A., Franco, J., Orive, E., 1994. Suspended particulate matter dynamics in the shallow mesotidal urdaibai estuary (Bay of Biscay, Spain). Netherland Journal of Aquatic Ecology. 28, 309–316. doi:10.1007/BF02334199

Sakai, H., Nozaki, Y., 1995. Biogeochemical Processes and Ocean Flux in the Western Pacific, First. ed. Terra Scientific Publishing Company, Tokyo, Japan.

Saucier, F.J., and Chassé, J. 2000. Tidal circulation and buoyancy effects in the St. Lawrence Estuary. Atmosphere-Ocean, 38: 505–556. doi:10.1080/07055900.2000.9649658.

Sauter, J. 1928. Die Grössenbestimmung der in Gemischnebeln von Verbrennungskraftmaschinen vorhandenen Brennstoffteilchen" VDI-Forschungsheft Nr. 279, 1926 und Nr. 312, 1928 (in german).

Savage, C., Elmgren, R., Larsson, U., 2002. Effects of sewage-derived nutrients on an estuarine macrobenthic community. Marine Ecology Progress Series. Ser. 243, 67–82.

Schaepman-Strub, G., Schaepman, M.E., Painter, T.H., Dangel, S., and Martonchik, J.V. 2006. Reflectance quantities in optical remote sensing—definitions and case studies. Remote Sensing of Environment, 103: 27–42. doi:10.1016/j.rse.2006.03.002.

Senatore, A., Mendicino, G., Knoche, H.R., Kunstmann, H., 2014. Sensitivity of Modeled Precipitation to Sea Surface Temperature in Regions with Complex Topography and Coastlines: A Case Study for the Mediterranean. J. Hydrometeorology. 15, 2370–2396. doi:10.1175/JHM-D-13-089.1

Shabbar, A., Skinner, W., 2004. Summer Drought Patterns in Canada and the Relationship toGlobal Sea Surface Temperatures. Journal of Climate. 17, 2866–2880. doi:10.1175/1520-0442(2004)017<2866:SDPICA>2.0.CO;2

Shell, K.M., Frouin, R., Nakamoto, S., Somerville, R.C.J., 2003. Atmospheric response to solar radiation absorbed by phytoplankton. Journal of Geophysical Research. Atmospheres 108, 4445. doi:10.1029/2003JD003440

Shi, J.Z., Gu, W.-J., Wang, D.-Z., 2008. Wind wave-forced fine sediment erosion during the slack water periods in Hangzhou Bay, China. Environmental Geology. 55, 629–638. doi:10.1007/s00254-007-1013-2

Siegel, D.A., Ohlmann, J.C., Washburn, L., Bidigare, R.R., Nosse, C.T., Fields, E., Zhou, Y., 1995. Solar radiation, phytoplankton pigments and the radiant heating of the equatorial Pacific warm pool. Journal of Geophysical Research. Oceans 100, 4885–4891. doi:10.1029/94JC03128

Siegel, D.A., Westberry, T.K., Ohlmann, J.C., 1999. Cloud color and ocean radiant heating. Journal of Climate. 12, 1101–1116.

Smith, R.C., Baker, K.S., 1981. Optical properties of the clearest natural waters (200-800 nm). Applied Optics. 20, 177–184.

Snyder, W.A., Arnone, R.A., Davis, C.O., Goode, W., Gould, R.W., Ladner, S., Lamela, G., Rhea, W.J., Stavn, R., Sydor, M., Weidemann, A., 2008. Optical scattering and backscattering by organic and inorganic particulates in US coastal waters. Applied Optics 47, 666. doi:10.1364/AO.47.000666

Sokal, R., Rohlf, J., 1995. Biometry, in: Biometry. W.H. Freeman, New York, NY, p. 887.

Spearman, C., 1904. The Proof and Measurement of Association between Two Things. The American Journal of Psychology 15, 72. doi:10.2307/1412159

Spencer, R.W., Braswell, W.D., 2013. The role of ENSO in global ocean temperature changes during 1955–2011 simulated with a 1D climate model. Asia-Pac. Journal of Atmospheric Sciences. 50, 229–237. doi:10.1007/s13143-014-0011-z

Stavn, R.H., Richter, S.J., 2008. Biogeo-optics: particle optical properties and the partitioning of the spectral scattering coefficient of ocean waters. Applied optics 47, 2660–2679.

Stokes, G.M., Schwartz, S.E., 1994. The Atmospheric Radiation Measurement (ARM) Program: Programmatic Background and Design of the Cloud and Radiation Test

Bed. Bulletin of American Meteorological Society. 75, 1201–1221. doi:10.1175/1520-0477(1994)075<1201:TARMPP>2.0.CO;2

Stramski, D., Reynolds, R.A., Babin, M., Kaczmarek, S., Lewis, M.R., Röttgers, R., Sciandra, A., Stramska, M., Twardowski, M.S., Franz, B.A., and Claustre, H. 2008. Relationships between the surface concentration of particulate organic carbon and optical properties in the eastern South Pacific and eastern Atlantic Oceans. Biogeosciences, 5: 171–201. doi:10.5194/bg-5-171-2008.

Strutton, P.G., Chavez, F.P., 2004. Biological Heating in the Equatorial Pacific: Observed Variability and Potential for Real-Time Calculation. Journal of Climate. 17, 1097–1109. doi:10.1175/1520-0442(2004)017<1097:BHITEP>2.0.CO;2

Sundby, B. 1974. Distribution and transport of suspended particulate matter in the Gulf of St. Lawrence. Canadian Journal of Earth Sciences, 11, 1517- 1533.

Tang, Q., Leng, G., 2013. Changes in Cloud Cover, Precipitation, and Summer Temperature in North America from 1982 to 2009. Journal of Climate. 26, 1733–1744. doi:10.1175/JCLI-D-12-00225.1

Therriault, J.-C., and Levasseur, M. 1985. Control of phytoplankton production in the Lower St. Lawrence Estuary: light and freshwater runoff. Naturaliste Canadien, 112: 77–96.

Thorndike, E.M., 1969. Optical Oceanography. N. G. Jerlov. Elsevier, New York, 1968. xvi + 194 pp., illus. $13.50. Elsevier Oceanography Series. Science 163, 64–64. doi:10.1126/science.163.3862.64

Tremblay, L., Kohl, S. D., Rice, J. A., and Gagné, J. P., 2005. Effects of temperature, salinity, and dissolved humic substances on the sorption of polycyclic aromatic hydrocarbons to estuarine particles. Marine Chemistry, 96(1), 21-34.

Tremblay, L., and Gagné, J. P. 2007. Distribution and biogeochemistry of sedimentary humic substances in the St. Lawrence Estuary and the Saguenay Fjord, Québec. Organic Geochemistry, 38: 682–699. doi:10.1016/j.orggeochem.2006.11.003.

Tremblay, L., and Gagné, J. P. 2009. Organic matter distribution and reactivity in the waters of a large estuarine system. Marine Chemistry, 116: 1–12. doi:10.1016/j.marchem.2009.09.006.

Troude, J.-P., and Sérodes, J.-B. 1990. Caractéristiques hydrodynamiques d'un estran à forte sédimentation. Canadian Journal of Civil Engineering, 17: 148–155. doi:10.1139/l90-019.

Turpie, K.R. 2013. Explaining the Spectral Red-Edge Features of Inundated Marsh Vegetation. Journal of Coastal Research, 290: 1111–1117. doi:10.2112/JCOASTRES-D-12-00209.1.

Vermote, E., Tanré, D., Deuzé, J.L., Herman, M., Morcrette, J.J., and Kotchenova, S.Y. 2006. Second simulation of a satellite signal in the solar spectrum-vector (6SV). 6S User Guide Version, 3, 2006.

Verspecht, F., Pattiaratchi, C., 2010. On the significance of wind event frequency for particulate resuspension and light attenuation in coastal waters. Continental Shelf Research. 30, 1971–1982. doi:10.1016/j.csr.2010.09.008

Wallace, A., 2012. DBCP Implementation Strategy. World Meteorological Organization (WMO), Fermantle, Australia.

Wang, H., Feingold, G., Wood, R., Kazil, J., 2010. Modelling microphysical and meteorological controls on precipitation and cloud cellular structures in Southeast Pacific stratocumulus. Atmospheric Chemistry and Physics 10, 6347–6362. doi:10.5194/acp-10-6347-2010

Wang, M., 2010. Atmospheric correction for remotely-sensed ocean-colour products. Reports and Monographs of the International. Ocean-Colour Coordinating Group IOCCG.

Wang, S., Tang, D., 2010. Remote sensing of day/night sea surface temperature difference related to phytoplankton blooms. International Journal of Remote Sensing. 31, 4569–4578. doi:10.1080/01431161.2010.485143

Wei, H., Sun, J., Moll, A., and Zhao, L. 2004. Phytoplankton dynamics in the Bohai Sea observations and modelling. Journal of Marine Systems, 44: 233–251. doi:10.1016/j.jmarsys.2003.09.012.

Wettstein, J.J., Mearns, L.O., 2002. The influence of the North Atlantic-Arctic Oscillation on mean, variance, and extremes of temperature in the northeastern United States and Canada. Journal of Climate. 15, 3586–3600.

Wozniak, B. and Dera, J., 2007. Light absorption in sea water (Vol. 33). New York: Springer.

Woźniak, S.B. 2014. Simple statistical formulas for estimating biogeochemical properties of suspended particulate matter in the southern Baltic Sea potentially useful for optical remote sensing applications*. Oceanologia, 56: 7–39. doi:10.5697/oc.56-1.007.

Woźniak, S.B., Darecki, M., Zabłocka, M., Burska, D., and Dera, J. 2016. New simple statistical formulas for estimating surface concentrations of suspended particulate matter (SPM) and particulate organic carbon (POC) from remote-sensing reflectance in the southern Baltic Sea. Oceanologia, 58: 161–175. doi:10.1016/j.oceano.2016.03.002.

Woźniak, S.B., Stramski, D., Stramska, M., Reynolds, R.A., Wright, V.M., Miksic, E.Y., Cichocka, M., Cieplak, A.M., 2010. Optical variability of seawater in relation to particle concentration, composition, and size distribution in the nearshore marine

environment at Imperial Beach, California. Journal of Geophysical Research 115. doi:10.1029/2009JC005554

Xi, H., Larouche, P., Tang, S., Michel, C., 2013. Seasonal variability of light absorption properties and water optical constituents in Hudson Bay, Canada: Absorption in Hudson Bay. Journal of Geophysical Research: Oceans 118, 3087–3102. doi:10.1002/jgrc.20237

Xiao, Y.-H., Räike, A., Hartikainen, H., and Vähätalo, A.V. 2015. Iron as a source of color in river waters. Science of The Total Environment, 536, 914–923. doi:10.1016/j.scitotenv.2015.06.092.

Xiao, Y.-H., Sara-Aho, T., Hartikainen, H., and Vähätalo, A.V. 2013. Contribution of ferric iron to light absorption by chromophoric dissolved organic matter. Limnology and Oceanography, 58, 653–662. doi:10.4319/lo.2013.58.2.0653

Xie, H., Aubry, C, Belanger, S., and Song. G. 2012. The dynamics of absorption coefficients of CDOM and particles in the St.-Lawrence estuarine system: Biogeochemical and physical implications. Marine Chemistry, 128–129, 44–56.

Yang, X., Sokoletsky, L., Wei, X., and Shen, F. 2017. Suspended sediment concentration mapping based on the MODIS satellite imagery in the East China inland, estuarine, and coastal waters. Chinese Journal of Oceanology and Limnology, 35, 39–60. doi:10.1007/s00343-016-5060-y.

Yeats, P.A. 1988. Distribution and transport of suspended particulate matter. In: Strain, P.M. (Ed.), Chemical Oceanography in the Gulf of St. Lawrence. Department of Fisheries and Oceans, chapter 2, pp. 15-28.

Yeats, P.A., and Bewers, J.M. 1976. Trace metals in the waters of the Saguenay fjord. Canadian Journal of Earth Sciences, 13, 1319–1327.

Yu, J.C.S., Chou, T.-Y., Yu, H.-C., Chen, P., Vanhellemont, Q., and Fettweis, M. 2016. Surface suspended particulate matter concentration in the Taiwan Strait during summer and winter monsoons. Ocean Dynamics, 66: 1517–1527. doi:10.1007/s10236-016-0992-5.

Yu, L., Zhang, Z., Zhong, S., Zhou, M., Gao, Z., Wu, H., Sun, B., 2011. An inter-comparison of six latent and sensible heat flux products over the Southern Ocean. Polar Research. 30. doi:10.3402/polar.v30i0.10167

Zaneveld, J.R.V., Twardowski, M.J., Barnard, A., and Lewis, M.R. 2005. Introduction to Radiative Transfer. In Remote Sensing of Coastal Aquatic Environments. Edited by R.L. Miller, C.E.D. Castillo, and B.A. Mckee. Springer Netherlands. pp. 1–20. Available from http://link.springer.com/chapter/10.1007/978-1-4020-3100-7_1

Zarco-Tejada, P.J., Miller, J.R., Mohammed, G.H., Noland, T.L., and Sampson, P.H. 2000. Chlorophyll fluorescence effects on vegetation apparent reflectance: II. Laboratory and airborne canopy-level measurements with hyperspectral data. Remote Sensing of Environment, 74: 596–608.

Zhai, L., Tang, C., Platt, T., Sathyendranath, S., 2011. Ocean response to attenuation of visible light by phytoplankton in the Gulf of St. Lawrence. J. Maritime Systems. 88, 285–297. doi:10.1016/j.jmarsys.2011.05.005

Zhang, C., Hu, C., Shang, S., Müller-Karger, F.E., Li, Y., Dai, M., Huang, B., Ning, X., and Hong, H. 2006. Bridging between SeaWiFS and MODIS for continuity of chlorophyll-a concentration assessments off Southeastern China. Remote Sensing of Environment, 102: 250–263. doi:10.1016/j.rse.2006.02.015.

Zhang, M., Tang, J., Dong, Q., Song, Q., Ding, J., 2010. Retrieval of total suspended matter concentration in the Yellow and East China Seas from MODIS imagery. Remote Sensing of Environment. 114, 392–403. doi:10.1016/j.rse.2009.09.016

Zhang, R.-H., 2014. Effects of tropical instability wave (TIW)-induced surface wind feedback in the tropical Pacific Ocean. Climate Dynamics 42, 467–485. doi:10.1007/s00382-013-1878-6

Zhang, X., Hu, L., He, M.-X., 2009. Scattering by pure seawater: Effect of salinity. Optics Express 17, 5698. doi:10.1364/OE.17.005698

Zhang, X., Huot, Y., Gray, D.J., Weidemann, A., and Rhea, W.J. 2013. Biogeochemical origins of particles obtained from the inversion of the volume scattering function and spectral absorption in coastal waters. Biogeosciences, 10: 6029–6043. doi:10.5194/bg-10-6029-2013.

Zhang, X., Stavn, R.H., Falster, A.U., Gray, D., Gould, R.W., 2014. New insight into particulate mineral and organic matter in coastal ocean waters through optical inversion. Estuarine, Coastal and Shelf Science 149, 1–12. doi:10.1016/j.ecss.2014.06.003